Title
State Structure and Operator Dynamics in Quantum Many-Body Systems: from s-Sourcery to Strong Zero Modes

Author
Olund, Christopher Thomas

Publication Date
2022

Peer reviewed|Thesis/dissertation

State Structure and Operator Dynamics in Quantum Many-Body Systems: from s-Sourcery to Strong Zero Modes

by

Christopher Thomas Olund

A dissertation submitted in partial satisfaction of the

requirements for the degree of

Doctor of Philosophy

in

Physics

in the

Graduate Division

of the

University of California, Berkeley

Committee in charge:

Professor Norman Yao, Chair
Professor K. Birgitta Whaley
Professor Joel Moore

Spring 2022

State Structure and Operator Dynamics in Quantum Many-Body Systems: from s-Sourcery to Strong Zero Modes

Abstract

State Structure and Operator Dynamics in Quantum Many-Body Systems: from s-Sourcery to Strong Zero Modes

by

Christopher Thomas Olund

Doctor of Philosophy in Physics

University of California, Berkeley

Professor Norman Yao, Chair

In this disseration we explore the structure and construction of certain quantum many-body states, as well as operator dynamics in quantum many-body systems. First, we detail the implementation of a new tensor network ansatz for many-body ground states based on adiabatically evolving a state to repeatedly double in size. Next, we extend the notion of 'strong zero modes, ' edge-localized operators stable at infinite temperature, to operators localized to boundaries between systems. We then discuss efforts to numerically characterize scrambling, a strong form of thermalization, in the Sachdev–Ye–Kitaev model. Finally, we show that a states with large momentum splittings can be created via symmetric Bloch oscillations in two optical lattices being accelerated in opposite directions.

To my family

Contents

List of Figures

Acknowledgments

I have to start by thanking my advisor, Norman Yao, for guiding me through my PhD, teaching me a ton of physics, and pushing me when he knew I could be doing more. I'd also like to thank the other professors whose groups I rotated through before ending up in Norm's: Ashvin Vishwanath, Jeff Neaton, and Joel Moore. I also thank Joel and Birgitta Whaley for serving on my committee.

I've been privileged to work with many great collaborators as well. Snir Gazit and Jack Kemp entrusted me with the central projects of my disseration, and mentored me throughout their completion. Max Block joined a very complicated numerical project halfway through as a new grad student and was crucial in pushing it to the finish line. Bryce Kobrin and Greg Kahanamoku-Meyer picked up where I left off on my scrambling project, greatly expanding the ambition of the numerics. Zack Pagel gave me the opportunity to work with him on the theory for what would have already been an impressive experimental paper without my help. I'd also like to thank all of my other coauthors, whether I worked with them directly or not, as well as everyone I worked with on projects abandoned due to either hitting a brick wall or a global pandemic.

I was also fortunate to be able to learn from many other members of the Yao group, whether theorists or experimentalists. I would especially like to thank my officemates Tommy Schuster and Kam Akkaravarawong, as well as Francisco Machado, for always being willing to listen to me talk through what I was trying to do and providing valuable insight. I'd also like to thank Thomas Mittiga, Bingtian Ye, Chong Zu, Satcher Hsieh, Pra Bhattacharyya, Rahul Sahay, Soonwon Choi, and everyone else in the group past or present.

I couldn't have gotten through years at Berkeley without my friends, particularly in my incoming class. I'd especially like to thank Steve Drapcho, Neil Goeckner-Wald, and Erik Urban, who were fantastic roommates through our first year of graduate school, and Steve and Neil for the next five years as well. I'd also like to thank Sam Kohn and Charlie Hill, as well as Mike Fang, Will Livingston, Ning Bao, and everybody else I roped into doing various puzzle hunts over the years. And of course, all of the other friends I made here.

Finally, my biggest thanks of all go to my dad and mom, Thomas and Barbara, as well as to my brother Anthony, for all of their love and encouragment. My almost daily calls with my dad in particular were a pillar of support that I couldn't have gone without.

Chapter 1

Introduction

In recent years there has been a surge of interest in quantum information science and quantum computing. These topics sit at a convergence between many areas of physics, from condensed matter and atomic physics to even gravitational physics, not to mention other fields altogether such as computer science. The results described in this thesis similarly form a constellation of topics related to the structure and dynamics of information in quantum many-body systems.

In particular, the results herein are related to the following questions. First, how does one describe a many-body state of interest succinctly, i.e. using a number of parameters that scales manageably with system size? Relatedly, how might one physically construct states of interest with high fidelity? Next, how does information spread throughout a system? In particular, how does one tell when that information has, in a sense to be defined later, *maximally* spread, and how could one characterize the speed at which this process occurs? Finally, can we identify robust degrees of freedom in which to store information? Before going into more detail about these and outlining the thesis, I will first recount my history throughout my PhD.

1.1 My Time in Grad School

I started graduate school at Berkeley in the fall of 2013, having received an undergraduate degree in physics and math from the University of Virginia (UVA) the previous spring. During undergrad I had done theoretical research on Bose–Einstein condensates (BECs) and topological insulators (TIs), and planned to continue studying the latter during grad school. At the time, of course, I didn't have much perspective on the breadth of research being done in condensed matter or AMO physics, let alone physics in general, and that initial plan wouldn't last long.

I had something of a circuitous journey leading up to finding a research group. The spring of my first year I asked Professor Ashvin Vishwanath if he would give me a project on TIs. It turned out that most of the basic TI theory had been more or less worked out

by that time, so I was given a project that involved finding the edge modes in a 2D Floquet system, i.e. a system with a drive periodic in time. Such systems no longer have states with well-defined energies, but there still exists the concept of an eigenstate's *quasi*energy which is defined modulo $2\pi/T$ where T is the period of the drive. Unfortunately, this project ended up being scooped a month or two after I started it.

At the end of the summer I parted ways with Ashvin; while I enjoyed the research itself, his advising style was more hands-off than was ideal for me as a young grad student. I next approached Joel Moore who was, at the time, stretched a bit thin; he suggested that I might be able to be coadvised by him and another professor. With that plan in mind, I rotated with Jeff Neaton's group the following spring, learning the basics of density functional theory (DFT), a powerful numerical technique for finding approximate ground states in actual materials. Over the course of the semester, it became apparent that DFT was not for me; my enjoyment of physics was primarily derived from my love of math, and the heavy numerics involved here were too far removed from that for my taste.

Hearing this, Joel graciously offered to give me a project himself. His first idea was a project involving thermal transport in the Lieb–Liniger model, a 1D gas of bosons with a delta function contact interaction. After a few weeks of learning about the notion of quantum integrability (a concept that would arise again in several of my later projects) and the Bethe ansatz, Joel proposed another idea that he thought might make for a better first project. A paper[1] had just come out that proposed a universal speed limit on the rate at which a system can "scramble" information. The notion of scrambling is one in which initially local information strongly delocalizes throughout the system. Black holes saturated this bound, as did a system of fermions with random all-to-all four body interactions known as the Sachdev–Ye–Kitaev (SYK) model. Because the theory was based on systems in the thermodynamic limit, previous numerical studies had trouble actually extracting the rate at which systems scrambled in finite sized systems. The project was to carefully extract this scrambling rate in the finite size SYK model, extrapolate to the thermodynamic limit, and use knowledge of the analytic results to ensure that our methodology was actually working. Ideally, we wanted to find a method that would be applicable to other systems where we didn't already know the answer.

That September my current advisor Norman Yao, then a postdoc, was brought on to the project. My initial SYK numerics were hacked together in Mathematica and limited to quite small systems due to need to average over many realizations of the model with different random couplings. Under Norm's tutelage over the next year or so I recoded everything in Python, improved the efficiency of the implementation, and learned how to utilize supercomputer clusters to parallelize the calculations. Around the end of 2016 Norm had become a professor and Joel was about to be the interim department chair, so we all decided that it made sense for me to officially switch to Norm's group.

Around this time I picked up a few more projects. First, I began working with another of Norm's grad students, Francisco Machado, on trying to improve existing Lieb–Robinson bounds in systems with long-range interactions. After a few months we ran into a wall with it; the approach we were trying at the time improved the bound only by constant

factors. The other project, started in early 2017, would end up becoming one of the core topics of this thesis. It was proposed to me by Snir Gazit, then a postdoc in the group, and was based on a theoretical protocol for many-body state construction called "s-source" (or more lightheartedly "s-sourcery")[2]. The idea was to take the ground state of a system with a small number of degrees of freedom and use it to build the ground state of the corresponding system of twice the size by interleaving ancillary degrees of freedom between those of the original system and then acting on the combined system with adiabatic time evolution between the two systems' Hamiltonians. Snir's pitch was that we would actually implement this protocol numerically.

Meanwhile, a few more students, Bryce Kobrin and Greg Kahanamoku-Meyer, were brought onto the SYK project to try and push to larger system sizes; there was a qualitative change in the temperature dependence of the model's scrambling rate around 20 Majorana fermions, and with exact diagonalization I could only go up to 24 or 26. Going further would involve more advanced numerical techniques. Over time the scope of the project grew and I became less involved as I focused on other projects, with Bryce eventually leading the publication of the project's results a couple years later.

During the s-source project we collaborated with John McGreevy, one of the authors of the original s-source paper. Another grad student, Max Block, joined the project about halfway through and helped to push the project to its conclusion. We finally wrapped up and submitted the paper in February 2020, mercifully shortly before the COVID pandemic really took off in the US.

Back during the fall of 2017 Norm taught a very comprehensive graduate atomic physics course which I, along with the rest of the group, took. Applying what I learned in that course, I did theory work for several experiments in parallel to the s-source project. Two of those collaborations, one involving engineering interactions in a cavity system with Dan Stamper-Kurn's group and the other involving Floquet states in a kicked 2D harmonic oscillator with Holger Mueller's group eventually stalled, and, with the pandemic, were never picked back up. A third, however, did result in a paper. Here I worked with Zack Pagel, also in Holger's group, to help explain the theory underlying an experiment of theirs that formed states with very large momentum splittings in an optical lattice using symmetric Bloch oscillations.

I started my final project shortly after the COVID lockdowns began in 2020. The project involved operators known as "strong zero modes" (SZMs). SZMs are localized to the edges of many-body systems and correspond to degrees of freedom which are stable even at infinite temperature. The goal was to see if this notion generalized to operators localized to the boundary between two systems in different phases (say an Ising paramagnet and an Ising ferromagnet). While the answer ended up being yes, we also ended up discovering a lot of subtle physics, as well as fundamental differences between the boundary SZMs in spin systems and the corresponding systems of Majorana fermions (which described exactly the same physics for the old "edge" SZMs). In this thesis, I will detail the subset of projects that I worked on that ultimately led to publications.

1.2 Outline

The number of parameters required to fully specify an arbitrary state in a quantum many-body system scales exponentially with the physical size of the system. Because we often care about behavior of such systems in the thermodynamic limit such a scaling has a potential to be devastating to our efforts to conduct numerical studies into systems of interest, particularly if finite size effects don't rapidly fade. Thankfully, nature is sometimes merciful; it turns out that many states of interest can be described to an excellent approximation using relatively few parameters if one assumes an appropriate structure of the wavefunction (i.e. an ansatz). Many such ansatzes fall under the title of tensor networks, as the states are described as some set of tensors that can be contracted to calculate quantities of interest. The most famous tensor network ansatz is the matrix product (MPS) [3–6] which efficiently describes 1D states with low entanglement entropy; happily, this includes the ground states of many local Hamiltonians. Another of relevance to us the multiscale entanglement renormalization ansatz (MERA) [7–11]. In a MERA one starts with a large state and repeatedly forms a smaller state through three steps: first, forming blocks of neighboring states, next applying unitary transformations called disentanglers to, well, disentangle neighboring blocks, and finally applying a second set of transformations called isometries to coarse-grain blocks into single degrees of freedom.

In Chapter 2, I will discuss a numerical implementation of the "s-source" state preparation protocol proposed in Ref. [2]. If one considers a family of Hamiltonians $\{H_N\}$ of N-body systems, the s-source procedure constructs the ground state of H_{2N} by first taking the ground state of H_N, interleaving another N ancillary degrees of freedom, and then applying a unitary transformation. The unitary transformation in this case is simply the one obtained through adiabatic evolution between H_N (of the "original" degrees of freedom) and H_{2N}. For families of Hamiltonians belonging to what is known to an "$s = 1$ fixed point" we expect that the adiabatic unitary exists and is quasilocal, allowing it to be approximated by a finite depth quantum circuit. Our implementation assumes the existence of such a circuit, and then actually finds it by minimizing the energy of a corresponding tensor network ansatz. The procedure can be iterated to find approximate ground states of H_{4N}, H_{8N}, and so on. Note that this tensor network is itself a variant of MERA, though we're thinking about it upside down and are starting from an exact state at some small N. Notably, there exist states that cannot be constructed by applying a quantum circuit of sub-extensive depth to a product state than can be so constructed by the s-source protocol, assuming the small initial state can be constructed by some other means.

Next, in chapter 3, I show evidence strongly suggesting that objects known as strong zero modes (SZMs) exist on the boundary between a transverse field Ising model in the ferromagnetic phase and another in the paramagnetic phase (or, it turns out, in another ferromagnetic phase with a different coupling, or even one at the critical point). Previously shown to exist at the edges of certain models [12–20], strong zero modes are quasilocal operators that commute with the system's Hamiltonian up to a term exponentially small in the system's size, anticommute with a symmetry of the system, and square to the identity.

They correspond to a degree of freedom that is stable up to times exponentially large in the system size even at infinite temperature. We might hope to use such objects to construct qubits that are similarly robust. Extending the notion to phase boundaries invites the possibility of further control and manipulation of the SZMs; for example, we might be able to transport them by moving the phase boundary[21].

For the normal 'edge' SZMs one could equivalently describe a spin system in terms of an equivalent system of Majorana fermions by way of a Jordan–Wigner (JW) transformation. The SZMs of the two systems are then also exactly the same, related by the same transformations. We point out that this is *not* true for the boundary problem; the SZM at the boundary of two Ising models is in fact different, and much more complicated, than the one that exists at the boundary of two equivalent Kitaev models due to the fact that the JW transformation is nonlocal. While the Kitaev boundary SZM is trivial, it is not obvious that the purported SZM for the Ising boundary is exact; in fact, for some parameter choices it ceases to exist. Nevertheless, we argue that the operator's series expansion has some finite radius of convergence for which it is an exact SZM. We show this both with numerical evidence as well as analytic arguments. In particular, we prove that a simpler model with a finite left chain has an exact SZM despite displaying many of the same features that would make us fear that the original model might not have an SZM, and we provide a counting argument to show that the number of terms at each order in perturbation theory grows slowly enough that convergence is plausible.

In Chapter 4, I will discuss efforts to numerically extract the Lyapunov exponent λ in Sachdev–Ye–Kitaev model at finite size. λ characterizes the rate at which a system scrambles; that is, how long it takes for local operators to evolve into complicated operators involving terms with support on roughly all sites in the system. This corresponds to information being maximally delocalized throughout the system, and it was shown by Maldecena et al. in Ref. [1] that under reasonable assumptions the Lyapunov exponent of a system with inverse temperature β can be bounded by

$$\lambda \leq 2\pi/\beta. \tag{1.1}$$

Scrambling in a system can be diagnosed by objects known as out-of-time-order correlators (OTOCs), defined for local operators V and W as $\langle W(t)V(0)W(t)V(0)\rangle$. All OTOCs decay from their initial values at $t = 0$ to 0 at late times in a system that scrambles with characteristic rate λ. The SYK model is known to saturate the Maldacena bound at low temperatures, but the assumptions of the proof break down for small systems; in fact, for systems of fewer than about 20 Majorana fermions the SYK model sees λ *decreasing* with temperature. Here we make efforts to carefully characterize $\lambda(N, \beta)$; I focus mainly on progress made during the first year and a half of the project when I was leading it.

In chapter 5, I discuss the theory underlying the creation of symmetric states with large momentum splittings by accelerating two optical lattices in opposite directions (the paper this chapter is based on also details the successful experimental implementation of this protocol, but as that predated my involvement with the project, I omit that section from

this thesis). The resulting Bloch oscillations adiabatically transfer an initial state $|0\rangle$ through a series of states $(|n\hbar k\rangle + |-n\hbar k\rangle)/\sqrt{2}$ for $n = 1, 2, \ldots$. We explain that the decoupling of symmetric and antisymmetric momentum states allows us to transform the problem into one quite similar to a single accelerated lattice under a rotating wave approximation (RWA), and avoid issues previously assumed to prevent efficient adiabatic transfer near velocity degeneracy. Furthermore, we explicitly derive a condition on the lattices' ramp rate such that the RWA is valid.

1.3 Previously published work

Chapter 2 of this thesis was previously published as Ref. [22], and appears here with minor edits for formatting and clarity (e.g. replacing instances of "this paper" with "this chapter").

Chapter 3 is based on work I did with Jack Kemp and Norman Yao, and will be submitted for publication in the near future [23].

The project described in Chapter 4 has been published in Ref. [24], but that paper is not reproduced here (with the exception of one figure containing the ultimate results of the paper). Instead the chapter is primarily based on my early contributions to the project.

Chapter 5 was previously published as Ref. [25]. In addition to minor formatting edits I have also removed details of the paper's experimental results, as I was only involved with the theoretical side of the project.

Chapter 2

Adiabatic state preparation

2.1 Introduction

2.1.1 Motivations

In this chapter, I detail the implementation of a new tensor network ansatz for ground states of many-body Hamiltonians called 's-source' [2]. In addition to the straightforward motivation to find representations that either can more accurately capture the target state or that are easier to optimize, this particular tensor network has an associated physical interpretation that could be naturally adapted (at least in principle) to make an experimental state prepation protocol. The basic idea behind the ansatz, which will be expanded upon in subsequent sections, is that one starts with the exact ground state of a few-body system and then creates ground states of larger systems via adiabatic evolution between Hamiltonians at different system sizes. In particular, we imagine repeatedly doubling the size of the system through this evolution, interleaving new degrees of freedom at each step to be incorported into the larger system.

Numerically, if we allow ourselves to start from a small enough system we know we can find the ground state through exact diagonalization. The hope is that we can leverage our knowledge of this small-system state and allow the adiabatic theorem to guide our way through the increasingly high-dimensional Hilbert spaces of the larger systems. In this chapter, the adiabatic approach both informs the structure of the tensor network and helps to justify a greedy approach to optimization which cuts down on computational costs. While our algorithm to find the s-source representation of a state is variational, one could also in principle utilize the adiabatic theorem directly to construct a tensor network. Because the s-source circuit is actually a variant of another well-studied tensor network, the multiscale entanglement renormalization ansatz (MERA) [7–11], these ideas could be explored in more traditional MERAs as well.

Adiabatic state preparation is also of general interest to experimentalists as an alternative to preparing states via cooling in situations where that may be difficult to achieve [26], or even to create excited states inaccessible to cooling (see Chapter 5 of this dissertation for

one such example). This allows one to to choose some other initial Hamiltonian for which the ground state is easier to prepare, and then change the Hamiltonian slowly into that of the target system. This is particularly relevant to cold atom experiments in which one has a large amount of control over the system's Hamiiltonian [27–29], as well as in quantum computation [30, 31]. The s-source tensor network presents an additional complication due to the need to introduce new degrees of freedom at each length scale; one might imagine being able to accomplish this using optical tweezers [32–34]. Any practical matters aside, the s-source construction provides a different perspective on how to think about the structure of many body states.

2.1.2 Tensor networks

A deep lesson of late-20$^{\text{th}}$-century physics is the renormalization group (RG) philosophy: many body physics is organized scale-by-scale. The fruits of this lesson have been assimilated well into our understanding of classical statistical physics and of perturbative quantum field theory [35, 36]. In strongly-correlated quantum systems, however, we still have a great deal to learn, in particular about eigenstates and even groundstates of local model Hamiltonians.

Most of many-body Hilbert space is fictional, at least in the sense that it cannot be reached from a product state by time evolution with local Hamiltonians in a time polynomial in system size [37]. Ground states of local Hamiltonians are even more special: generically (with few exceptions arising from an overabundance of gapless excitations) the entanglement entropy of large-enough subregions satisfies an area law [38]. This statement is supported by a great deal of evidence, and has been rigorously proved for gapped systems in 1D [39].

Importantly, much of the area-law corner of Hilbert space can be efficiently parameterized using tensor networks. This has been done with several different tensor network geometries, such as matrix product states (MPS) [3–6] in 1D, and projected entangled pair states (PEPS) [40–43] and isometric tensor networks [44, 45] in 2D. These parameterizations have proven to be very effective variational ansatzes in a wide range of circumstances [46, 47] [1]. In particular, the density matrix renormalization group (DMRG) algorithm can be understood as a variational optimization on the MPS manifold [52, 53].

Despite their successes, variational algorithms based on area-law tensor network ansatzes face some limitations. Specifically, in gapless phases, or at critical points, entanglement entropy can diverge with subsystem size making these area-law tensor networks sub-optimal variational manifolds. It is also known that there exist even area law states that do not have an efficient MPS representation [54]. Finally, many tensor networks are difficult to efficiently optimize in $D > 1$ [47, 55].

Developing numerical methods for gapless phases and critical points requires understanding a richer entanglement structure than area-law states exhibit – we must account for the amount of entanglement at each length scale. The process of organizing our understanding

[1] We note that there are also *non-variational* algorithms for finding ground states that make use of tensor networks, some of which are provably efficient in some circumstances [48–51]

of the entanglement in a quantum state scale-by-scale is sometimes called *entanglement renormalization* [56, 57]. So far, the best-developed implementation of this idea is the multiscale entanglement renormalization ansatz (MERA), which is a state-of-the-art variational ansatz for the study of 1D quantum critical points [7–11]. MERA has also inspired several variants such as deep MERA (DMERA) [58] and an analytic construction continuous MERA (cMERA) [59, 60].

Despite the successes of MERA, developing a deeper understanding of entanglement renormalization remains a key challenge in condensed matter physics. More generally, existing tensor network methods leave room for improvement in several ways. First, the numerical values of the optimal tensors found in this way are difficult to interpret or directly relate to analytic results; the procedure is essentially a black box (though we note that in certain situations analytical constructions of MERA have been found using wavelets [61, 62]). Second, and more practically, the variational minimization of the expectation value of the Hamiltonian requires sweeping across the lattice many times, an often-costly procedure which has many opportunities to get stuck in locally-optimal configurations.

In this chapter, we introduce and benchmark a numerical algorithm for entanglement renormalization that takes small steps towards alleviating some of these issues. In particular, we provide a numerical implementation of the so-called s-source framework, originally introduced in Ref. [2]. We note that the purpose of this work is to implement s-source and characterize its accuracy; we leave a rigorous resource analysis to future studies.

2.1.3 s-source formalism

We now briefly describe the s-source formalism; a more thorough explanation is provided in Ref. [2]. Let H_L be a hamiltonian defined on a d-dimensional lattice of size L^d and $|\psi^L\rangle$ be the associated ground state. The Hamiltonian family $\{H_L\}$ belongs to an s-source fixed point if $|\psi^{2L}\rangle$ can be constructed by applying a quasi-local unitary U to s copies of $|\psi^L\rangle$ and some unentangled ancilla degrees of freedom. In many cases, we expect the adiabatic theorem to provide a construction of such a quasi-local unitary: if there is a gapped path from H_L to H_{2L} then adiabatic evolution along this path will suffice. There is evidence that many known states are s-source fixed points, including trivial insulators ($s = 0$), chiral insulators ($s = 1$) and various field theories [2]. Examples with $s > 1$ are known as well, including fracton models [63–65]. Belonging to an s-source fixed point constrains the growth of entanglement with system size, and in particular when $s < 2^{d-1}$ implies an area law for the entanglement entropy of subregions [2]. While the construction in Ref. [2] is more general, we will specialize our numerical exploration to one dimensional spin chains.

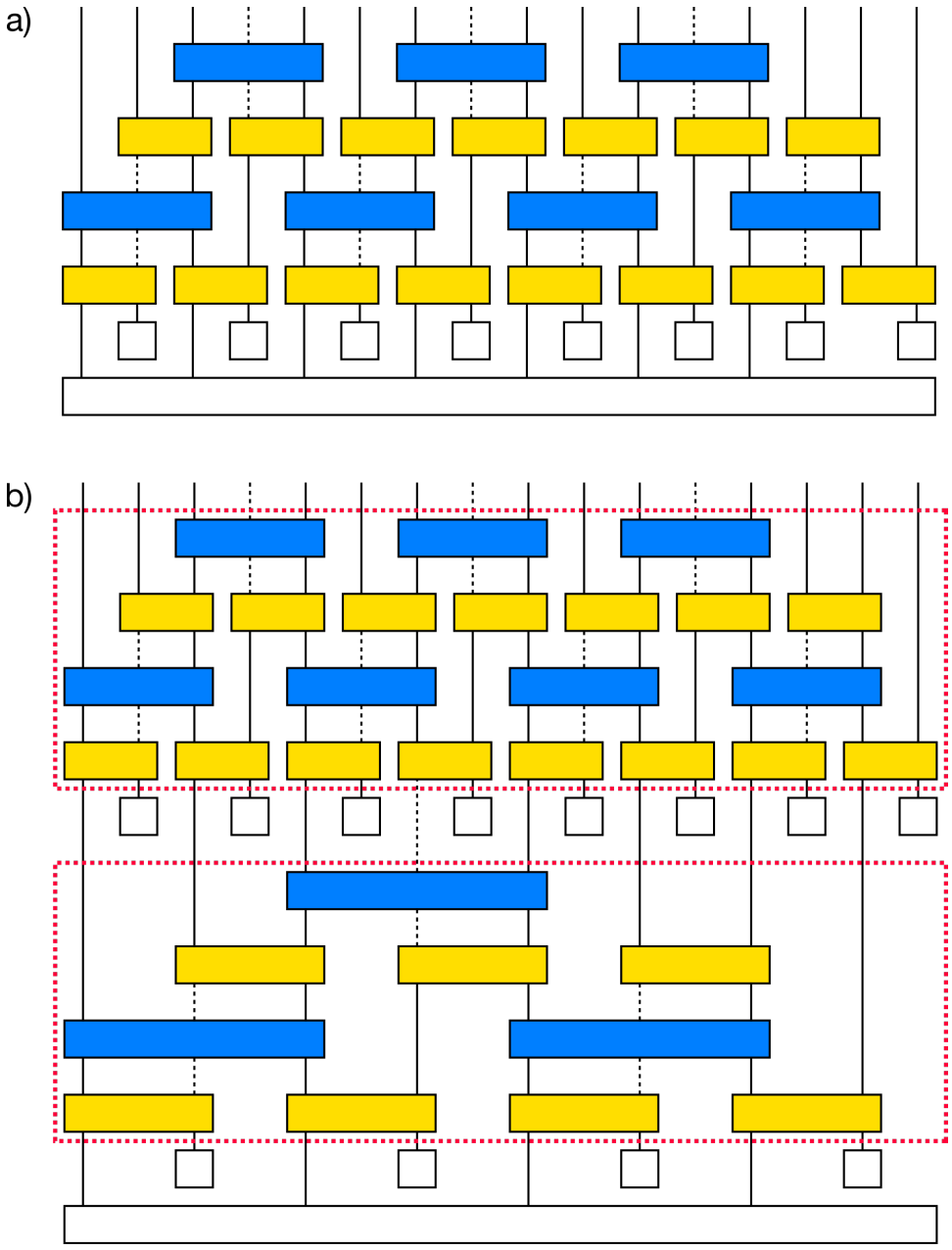

Figure 2.1: Circuit diagrams for the s-source renormalization procedure. a) A single layer of the circuit which takes an eight spin ground state (the large black box) and eight ancillae (small black boxes) and after applying the turn "on" (yellow) and turn "off" (blue) unitaries produces an approximation to the sixteen spin ground state. b) A two superlayer circuit which starts from the four spin ground state and produces an approximation to the sixteen spin ground state; each block outlined by a red dashed line represents a superlayer made up of two on and two off layers.

The key advantage of s-source is its ability to generate long-range entangled states using a constant depth circuit for $s \geq 1$. We illustrate this by comparing it to some more intuitive state preparation schemes. It is well known that building highly entangled states from a product state with local gates requires extensively deep quantum circuits [66]. Even with $|\psi^L\rangle$ as a resource, not all renormalization schemes generate long-range entanglement. In 1D, for example, one might consider concatenating two copies of a ground state end-to-end, and then acting with a local unitary to "glue" the states together. Unfortunately, constructing a long-range entangled state in this manner is not possible since the local unitary cannot strongly entangle distant spins in the two halves. In the s-source framework in 1D, we circumvent this issue by intercalating L ancilla spins between the spins that make up $|\psi^L\rangle$, thus expanding the underlying lattice. Crucially, this implies that a quasilocal unitary only needs to *locally* redistribute the rescaled entanglement structure. We will refer to the state formed by interleaving ancillae and $|\psi^L\rangle$ as the "$s = 1$ input state", or just the "s-source input state" where $s = 1$ is to be understood. In contrast, we would call a product state of $2L$ spins an "$s = 0$ input state."

To adapt the s-source construction to a numerical setting, one must decide how to implement the quasi-local unitary. One possibility would be to perform quasi-adiabatic evolution via an algorithm like time evolving block decimation (TEBD) [67, 68]. In this work, we take an alternative route and fix a tensor network structure informed by the analytic Trotterization of the adiabatic evolution, which we refer to as the s-source tensor network. The tensor network we obtain closely resembles a single layer of the MERA tensor network, and repeated application indeed results in a flavor of MERA. In principle, the Trotterized adiabatic unitary provides an exact expression for the s-source tensor network, but explicitly calculating it is generically computationally intractable. Instead, we seek to *find* the corresponding tensor network through other means. One approach, which is possible in certain limiting cases, is to make use of the Trotterized structure to determine analytic expressions for the constituent tensors. More generally, we can determine the s-source network variationally by minimizing the expectation value of H_{2L} with $|\psi^L\rangle$ as input (Fig. 2.1a). At its core, since we are still using a *variational* approach to identify the s-source tensor network, our prior concerns of becoming stuck in a locally-optimal configuration still apply.

Although we still resort to variational optimization, the existence of the analytic expression defining s-source allows us to physically interpret the resulting network and encourages us to optimize it in novel ways. For example, when considering multilayer s-source (red boxes in Fig. 2.1b), we think of each layer as an independent adiabatic expansion and optimize it *separately* by minimizing the energy of the appropriate Hamiltonian at that scale, given the input generated by the preceding layers. We emphasize that this is slightly different from the usual optimization of MERA, where one sweeps over the entire network multiple times. In general, our numerical procedure incurs larger errors than optimizing across all layers, and hence is sub-optimal when compared to standard global optimization approaches. Even so, it is less computationally expensive and, as we will explore below, can still perform well in certain cases of interest. In addition, by utilizing a greedy numerical algorithm, our implementation allows us to numerically test the validity of the adiabatic construction at

the heart of the s-source approach.

2.1.4 Performance of the s-source construction

We will benchmark our implementation's performance on the standard transverse field Ising model (TFIM)

$$H_{\text{TFIM}} = -J \sum_{\langle ij \rangle} \sigma_i^z \sigma_j^z - h \sum_i \sigma_i^x \tag{2.1}$$

as well as the TFIM with integrability-breaking perturbations [69, 70]. The TFIM has several limits that provide intuition about how s-source should behave in general. The first limit of interest is deep in the ferromagnetic phase ($h < J$), where the ground state at finite size is approximately a symmetric Greenberger–Horne–Zeilinger (GHZ) state, i.e. $(|\uparrow \ldots \uparrow\rangle + |\downarrow \ldots \downarrow\rangle)/\sqrt{2}$ (as opposed to the symmetry broken state such as $|\uparrow \ldots \uparrow\rangle$ that one would typically consider in the thermodynamic limit). Building a GHZ state from a product state with local gates requires a circuit of extensive depth, but with a size L GHZ input the size $2L$ GHZ state can be prepared using a single layer of nearest-neighbor controlled-not gates. Similarly, the exact finite-size ferromagnetic ground state at finite magnetic field is another simple example of a state with long-range entanglement that cannot be built from a product state with a finite depth circuit. One would expect the same to be true of a gapped ground state with nontrivial topological order: while we would have no hope of building such a state with a low depth circuit from a product input, an s-source input could allow one to construct a good approximation.

In contrast, the paramagnetic phase ($h > J$) is easier to approximate with a product state input. Deep in the phase the ground state is almost a product state, and the correlations that do exist are short-range. Using an s-source input naturally doubles the length scale of those correlations, and thus, to build the ground state one has to first *remove* those unwanted correlations before building the desired ones back in; for a product state input, we would only have to do the latter. Even if the s-source constructed state has low error, our effort is wasted; we could have done even better with less work by starting with a product state.

The most interesting case is at the critical point. Here, we generically observe a local minimum in the error as a function of the transverse field strength (Fig. 2.2). In some ways this is quite surprising; the existence of the analytic s-source construction relies on the adiabatic theorem, which in turn requires a gap. Of course, there will always be a gap due to finite system size; however, one naively expects that such a small finite-size gap would force one to use a longer adiabatic evolution time, thus incurring larger Trotter errors when approximating the adiabatic unitary with a local circuit. However, the scale invariance of the TFIM critical point makes it particularly amenable to approximation by s-source. At the critical point, the correlation length of the ground state scales with system size, so when we insert ancillae and hence trivially double the length scale of correlations, we actually achieve the proper long-range entanglement structure. We then correct the short range details with the local circuit. We note that the location of the error minimum remains at the critical

point even when one adds generic pertubations to the TFIM, consistent with the expectation that this behavior should generalize to other continuous phase transitions.

2.1.5 Organization

The remainder of the chapter is organized as follows. In Sec. 2.2, we give a precise description of both the s-source algorithm and our numerical implementation. In Sec. 2.3, we benchmark our numerical implementation by applying it to several standard 1D spin chain models: first, the (integrable) transverse field Ising chain (TFIM), next, the TFIM with a longitudinal field which is non-integrable and has no symmetries, and finally the TFIM with a symmetry-preserving but integrability-breaking term. In Sec. 2.4, we develop some analytic understanding of the circuit in the large-gap limit. In Sec. 2.5, we summarize our results and discuss potential future directions of study. Further technical details on numerical implementation and optimization are given in Sec. 2.6.1, while a derivation of the analytic unitaries given in Sec. 2.4 is provided in Sec. 2.6.2. These last two sections were appendices in the paper upon which this chapter is based and accordingly are supplemental to the rest.

2.2 s-source Algorithm and Numerical Implementation

In the s-source framework, we regard the entanglement present in the ground state at linear system size L as a resource for constructing the ground state at system size $2L$. Rather than attempting to directly prepare the macroscopic ground state of a model Hamiltonian, we suppose we are given s copies of the ground state at system size L, and design a circuit which doubles the system size. That is, we seek a unitary map which produces the ground state at size $2L$ from s copies of the ground state at size L times a collection of factorized ancillary qubits. Iterating this doubling procedure yields a circuit which produces the ground state in the thermodynamic limit from s copies of the (easily-determined) ground state of a small cluster of sites. We note, as previously discussed, that such a size-doubling map can exist even when the state represents a nontrivial phase and cannot be constructed from a product state via a low-depth local unitary circuit.

Our numerical implementation will focus on s-source with $s = 1$. When the Hamiltonian is gapped, one can immediately write down an expression for the s-source unitary using the adiabatic theorem. Let $\tilde{H}_L$ be the operator that acts as H_L on the odd lattice sites only. Now, consider a time-dependent Hamiltonian $H(t)$ which interpolates between

$$H(0) = \tilde{H}_L - \sum_{i \text{ even}} X_i \tag{2.2}$$

and

$$H(T) = H_{2L}. \tag{2.3}$$

Here, X_i are operators which put the ancillary qubits into a product ground state. The unitary operator which generates this time evolution is then:

$$U = \mathcal{T} e^{-i \int_0^T H(t) dt}. \tag{2.4}$$

Of course, if we could generally compute the full adiabatic unitary explicitly we could also solve the *easier* problem of just finding the exact ground state at system size $2L$! We can, however, imagine Trotterizing this unitary to get an approximation built out of *local* unitaries that is tractable enough to make further progress. When the gap is large we can find these component local unitaries analytically, as we explore in Sec. 2.4.1.

For the moment, however, we observe that even without actually doing the time-ordered integral, one can see upon which spins the local unitaries act; the terms in the leading order of the Trotter expansion will act on the same spins as do terms in either H_L or H_{2L}. Since we will work with nearest-neighbor Hamiltonians, one can think of the terms coming from H_{2L} as turning on interactions between the spins of our original L site system and the ancillae (which are now nearest neighbors after the interleaving step), and we can interpret the terms coming from H_L as turning off interactions between the original spins (which are no longer nearest neighbors). Keeping these leading order terms, we get an approximate tensor network for U as shown schematically in Fig. 2.1a.

Although we justify the circuit structure perturbatively, we will see from our numerics that it is still capable of generating approximate ground states even when a perturbative expansion would not converge. The order of the layers is in principle arbitrary, although some choices are more computationally efficient than others. We also note that one could choose to Trotterize into larger blocks and that doing so would improve the approximation in exchange for increased circuit optimization becoming much more computationally expensive. Later, in Sec. 2.4.2, we will see exactly how introducing longer range blocks reduces errors deep in either phase of the transverse field Ising model.

In our numerical implementation, we treat the tensor network as a variational ansatz built out of arbitrary local unitaries. We minimize $\langle H_{2L} \rangle$ over those component unitaries to get an approximation for $|\psi^{2L}\rangle$. As the reader may have noted, the circuit that we end up obtaining is, in fact, a MERA, albeit one with a particular circuit structure and where we have cut off some number of layers at the smallest scale. However, we are thinking of this MERA as being "upside down"; rather than starting with a large state and repeatedly coarse graining, we start with a small state and scale up.

Note that there is a fundamental tension between making the adiabatic evolution time T larger to reduce adiabaticity errors and making T smaller to reduce Trotterization errors for a fixed depth circuit. This tension disappears in the extreme limit of a large gap wherein we can determine U analytically, as we will describe in Sec. 2.4.1.

We now describe the actual circuit ansatz used, and explain how we numerically optimize it to find an approximate ground state. Suppose we have a solution for the ground state of H for an L spin system $|\psi^L\rangle$ in matrix product state (MPS) form. We construct the $2L$ spin input state $|\phi^{2L}\rangle$ by identifying spin i ($1 \leq i \leq L$) of the L particle system with spin

$2i-1$ of the $2L$ spin system, and then placing ancillary spins on the remaining sites. We note that the orientation of these ancillae does not matter as any single spin rotation can be absorbed into the circuit. Next, we construct a quantum circuit described by a total unitary U_T. We build this circuit in four layers: (i) applying two spin unitaries U_A^i to each pair of spins $(2i-1, 2i)$ for $1 \leq i \leq L$, (ii) applying unitaries U_B^i to pairs of spins $(4i-3, 4i-1)$ for $1 \leq i \leq L/2$, (iii) applying unitaries U_C^i to pairs $(2i+1, 2i)$ for $1 \leq i \leq L-1$, and finally (iv) applying U_D^i to pairs $(4i+1, 4i-1)$ for $1 \leq i \leq L/2-1$. The unitaries U_A^i and U_C^i correspond to turning on the new couplings between the original L spins and the ancillae, and the unitaries U_B^i and U_D^i and correspond to turning off the couplings between the original spins. A schematic of this setup for $L = 8$ can be seen in Fig. 2.1a. We can also repeat this procedure multiple times, successively inserting ancillae and then applying four layers of the circuit (which we will henceforth call a "superlayer") to repeatedly double the size of the input state. As an example, a two-superlayer circuit is illustrated in Fig. 2.1b.

In order to numerically optimize the circuit, we minimize the energy $E = \langle\widetilde{\psi}^{2L}|H_{2L}|\widetilde{\psi}^{2L}\rangle$ where $|\widetilde{\psi}^{2L}\rangle = U_T|\phi^{2L}\rangle$. In particular, we begin with an initial circuit (which could either be a random circuit or an educated guess) and then consider E to be a function of each of the individual local unitaries comprising U_T. We then sweep over all of these component unitaries multiple times using the conventional MERA update procedure described in [9]. For the interested reader, we provide some additional details about the numerical optimization in Sec. 2.6.1.

As mentioned above, this optimization procedure generally only finds a local minimum of the energy; if one wants to reliably find the global minimum, it is necessary to do this variational search many times with different initial conditions. To optimize a multilayer circuit, we pursue a greedy algorithm: for each superlayer, we minimize the expectation value of H_{2L} over the unitaries in the L to $2L$ layer with all preceding layers held fixed. The intuition behind this approach is that the adiabatic construction should in principle guarantee the existence of a multilayer circuit such that its first k superlayers generate the ground state at size $2^k L$. To be more precise, if we consider the analytic construction where we have the exact quasilocal adiabatic unitaries at our disposal, we know that one can construct the state $|\psi^{4L}\rangle$ from $|\psi^{L}\rangle$ by applying the adiabatic unitary $U^{L\to 2L}$ to get $|\psi^{2L}\rangle$ and then $U^{2L\to 4L}$ to get $|\psi^{4L}\rangle$. This suggests that a greedy approximation of each layer could in principle be effective.

Of course, re-optimizing all superlayers at each scale is at least as accurate and in some cases may yield much lower errors. However, full circuit optimization comes at a significant computational cost and we find that the greedy approach performs surprisingly well. Before presenting our numerical benchmarking results, we wish to emphasize that our approach, following the s-source philosophy, attempts only to find an optimal *adiabatic* trajectory, namely one which utilizes information from previous layers. In particular, we do *not* attempt a global energy minimization, as with standard MERA optimization schemes.

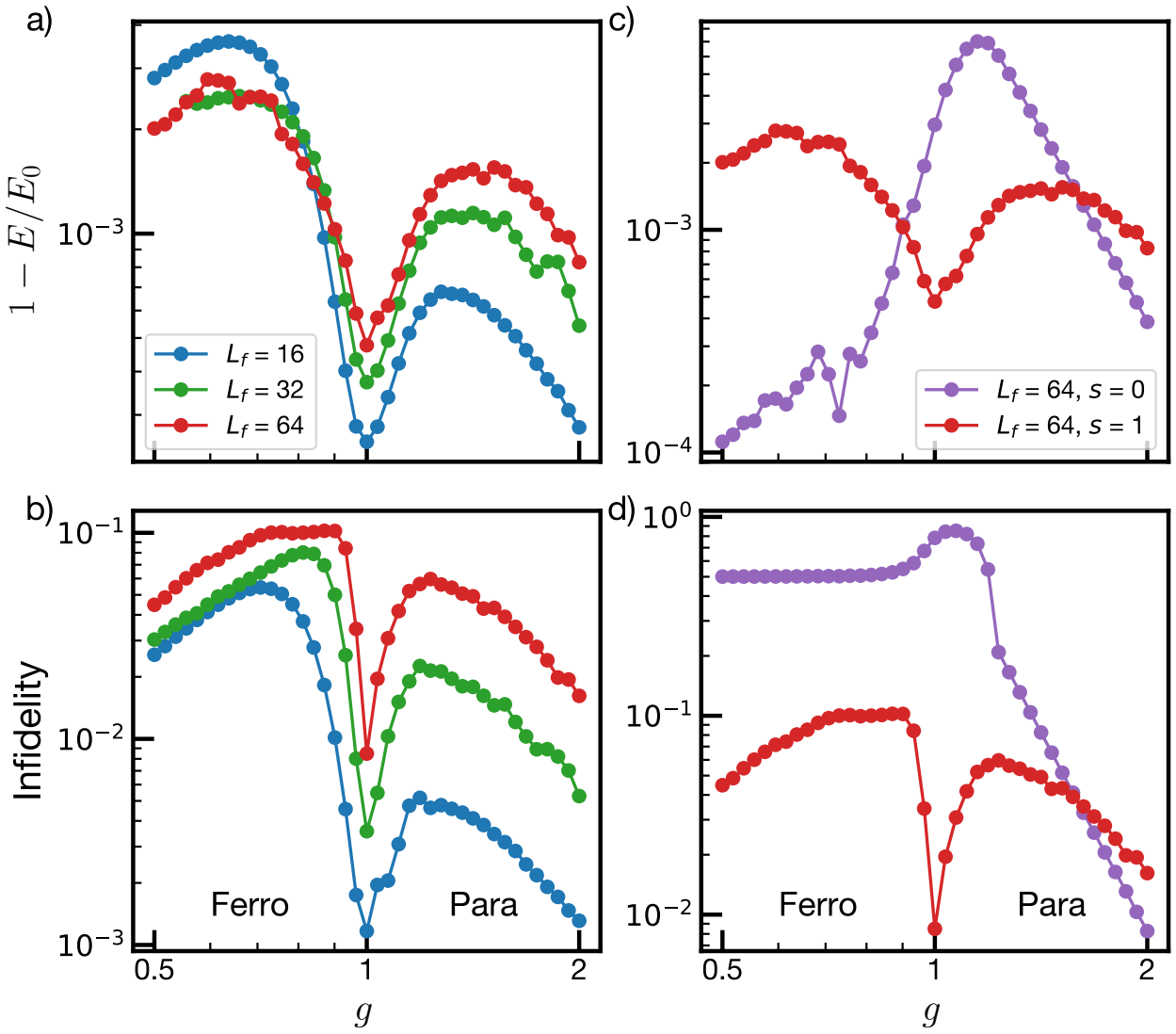

Figure 2.2: a) Relative energy error and b) infidelity of the TFIM s-source ground state as a function of g for several system sizes. Both go to 0 deep in either phase as one would expect, but there is also a local minimum at the critical point due to the scale invariance of the system. c) Relative energy error and d) infidelity for $L_\mathrm{f} = 64$ with with either the normal s-source input (s = 1) or product state input (s = 0). Using a product input state gives better energies deep in both phases, but has an infidelity over 0.5 in the ferromagnetic phase as long range entanglement cannot be generated. By either metric, s = 1 input gives substantially smaller errors near the critical point.

2.3 Numerical Benchmarking Results

To benchmark our numerical implementation we consider three 1D models: the transverse field Ising model (TFIM), a mixed-coupling Ising model (MCIM), and a mixed-field Ising model (MFIM), with Hamiltonians:

$$\begin{aligned} H_{TFIM} &= -J \sum_{\langle ij \rangle} \sigma_i^z \sigma_j^z - h \sum_i \sigma_i^x \\ H_{MCIM} &= -\sum_{\langle ij \rangle} \left(J_x \sigma_i^x \sigma_j^x + J_z \sigma_i^z \sigma_j^z \right) - h \sum_i \sigma_i^x \\ H_{MFIM} &= -J \sum_{\langle ij \rangle} \sigma_i^z \sigma_j^z - \sum_i \left(h_x \sigma_i^x + h_z \sigma_i^z \right). \end{aligned} \tag{2.5}$$

The TFIM sets our baseline understanding for how $s = 1$ s-source performs in three limits: a short range correlated unique ground state (the paramagnetic phase), an almost-degenerate long range correlated ground state (the ferromagnetic phase), and at a critical point.

We quantify our implementation's performance using both the relative error in energy (which we minimize) and the many-body infidelity, i.e. the overlap mismatch between the s-source state obtained at size $2L$ and the "exact" DMRG wavefunction at the same size, $1 - |\langle \widetilde{\psi}^{2L} | \psi^{2L} \rangle|^2$. As a point of reference, we compare this performance to that of $s = 0$ s-source, optimizing the same circuit structure with a product state input. We also study the consequences of truncating our approximation of the quasi-local unitary to include only nearest-neighbor gates. Finally, in order to understand the propagation of errors in our numerical s-source algorithm, we analyze the performance of multilayer circuits.

2.3.1 Benchmarking via the TFIM model

Since the TFIM is integrable, in this case, we calculate energy errors relative to the exact values. For the MCIM and MFIM models, we benchmark against energies obtained via DMRG. In addition, we use DMRG to generate our initial input MPS states for s-source for all three models (restricting to a specific $\mathbb{Z}_2$ parity sector when appropriate). In Fig. 2.2a, we plot the relative error in energy for a single layer of s-source for the TFIM as a function of $g = h/J$ for several values of the input system size L_0. To be specific, this means that we start with the ground state at L_0 and perform a single layer of our s-source algorithm to obtain an approximate ground state at $L_\mathrm{f} = 2L_0$, whose energy we then compare with the exact value. Similarly, Fig. 2.2b depicts the many-body infidelity, which exhibits the same qualitative behavior. In all of our numerics, we ensure that the input state in the ferromagnetic ($g < 1$) phase is the non-symmetry broken ground state.

As one expects, the error decreases deep in either the ferromagnetic or paramagnetic phase. Indeed, because the gap is large in these regions, there must exist a suitable s-source adiabatic unitary that minimizes both non-adiabatic and Trotter errors. Less expected, from this adiabatic perspective, is the existence of a local minimum in the error at the TFIM's

critical point, $g = 1$, despite the fact that the gap vanishes at this point. Naively, one might have expected that this would lead to an error maximum instead. In fact, this is exactly what does happen if we start with a product state input ($s = 0$) instead of the $s = 1$ s-source input state, as can be seen in Fig. 2.2c.

To understand this $s = 1$ local minimum, we note that the correlation length diverges at the critical point and that it is impossible to capture these correlations starting from a product state and using a low-depth local quantum circuit. However, if we start with the size L ground state (as we do in $s = 1$ s-source), then correlations of length L become correlations of length $2L$ upon ancillae insertion. In principle, at the critical point, this is exactly what we desire from the size $2L$ ground state; we emphasize once again that this is precisely the same intuition which underlies MERA and that our circuit is in fact a type of MERA with a "cut-off" at small scales.

To further check this intuition, we can define a single site energy error for the TFIM as

$$\epsilon(i) = -\frac{J}{2}\left(\sigma^z_{i-1}\sigma^z_i + \sigma^z_i\sigma^z_{i+1}\right) - h\sigma^x_i, \tag{2.6}$$

and then take a Fourier transform to define a momentum-resolved energy error $\epsilon(k)$. Doing this, we found that the momentum resolved error was only significant for momenta of $k = 0$, $k = \pi/4$, and $k = \pi/2$ (k in units of inverse lattice spacing). The $k = 0$ component is just the total energy error, whereas the $k = \pi/4$ and $k = \pi/2$ components correspond to errors of characteristic length scale 2 and 1 lattice spacings, respectively. These are, of course, exactly the length scales at which the nearest-neighbor and next-nearest-neighbor gates comprising our circuit act. There is no corresponding dip in $\epsilon(k = \pi/4)$ or $\epsilon(k = \pi/2)$ at the critical point, consistent with our understanding that the dip in the overall energy error really is due to ancilla insertion and not the local action of the circuit.

While this built in doubling of input correlations is beneficial at criticality, it can be detrimental in other regimes. This can be seen by comparing the performance of $s = 1$ s-source with $s = 0$ s-source deep in the paramagnetic phase ($g > 1$ in both Fig. 2.2c,d). While both errors are scaling toward zero as g increases, the scaling is worse for the $s = 1$ input. Here, the true ground state is short-range correlated, approaching a product state for large g. Thus, constructing the size $2L$ ground state with an $s = 1$ input actually involves first getting *rid* of all the doubled correlations.

Looking only at energy errors (Fig. 2.2c), the above statement would also appear to apply deep in the ferromagnetic phase ($g < 1$). However, the many-body infidelity tells a different story. In particular, although the energy errors for $s = 0$ s-source scale better than $s = 1$ s-source, the fidelity does not (Fig. 2.2d). To understand this behavior, we note that at $g = 0$, the ground state manifold of the TFIM is two-fold degenerate, consisting of the symmetric and anti-symmetric cat states. For finite but small g, these states will be split in energy by an exponentially small gap $\sim Jg^L$. Until g is nearly one, any linear combination of these two states will have approximately the same energy, and an "all up" like combination can be constructed from a product state input to give a low energy error. However, it is impossible to construct a cat state from a product state using a circuit with sub-extensive depth.

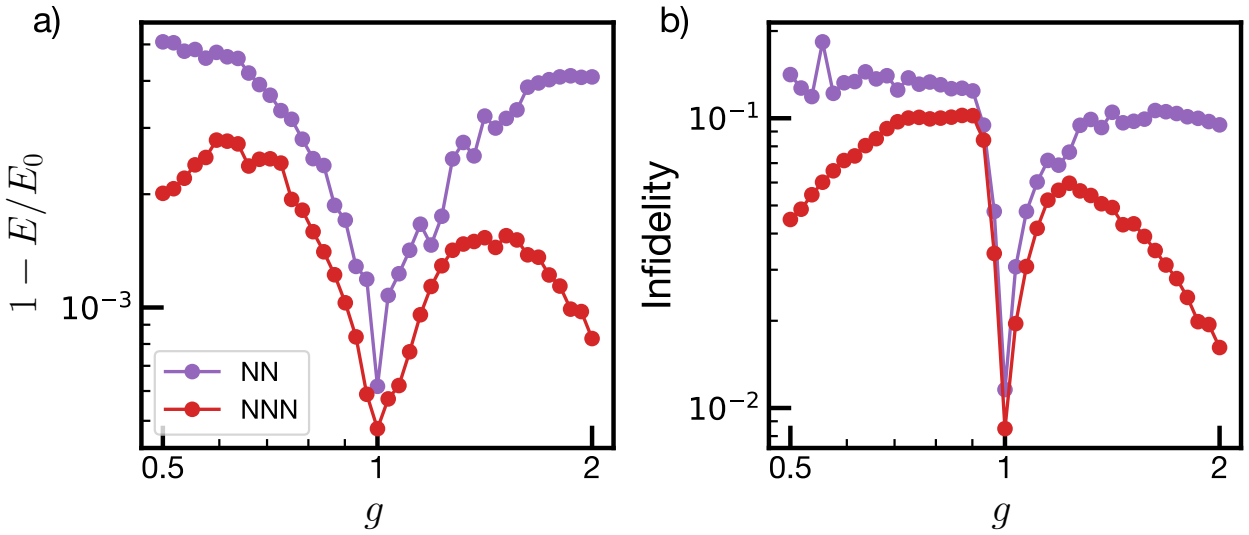

Figure 2.3: a) Relative energy error and b) infidelity of the TFIM for both the "standard" s-source circuit with both nearest-neighbor (NN) and next-nearest-neighbor (NNN) unitaries and a simplified circuit with only NN unitaries, both for $L_f = 64$. The general shape of the error curves, notably including the local minimum at the critical point, are similar for both circuits. The NN circuit does almost as well as the NNN circuit at the critical point, but the errors fall off more slowly than for the NNN circuit deep in either phase.

As a result, the infidelity of the $s = 0$ state is always greater than 0.5 throughout the entire ferromagnetic phase, as the zeroth order piece of the true ground state cannot be constructed. In contrast, with an $s = 1$ input state, a size L cat state can be used to create a size $2L$ cat state by using controlled NOT gates between each pair of original and ancilla spins. We expect that this behavior should generalize to certain classes of topological states. In particular, because one cannot change a topological invariant by acting with local unitaries, it is impossible to build such states from a product state input. On the other hand, using an $s = 1$ input preserves the topological character of the state.

2.3.2 Simplified circuit

Next, we turn to studying the effect of changing the range of the quasi-local unitary approximation by restricting our circuit to include *only* nearest-neighbor gates. A comparison of the resultant energy errors and infidelities are shown in Fig. 2.3. The nearest-neighbor circuit still exhibits a local error minimum at the critical point, and in fact nearly achieves the accuracy of the longer ranged s-source circuit there. This implies that the long-range correlations built in via ancillae insertion and the ability to perform nearest-neighbor corrective gates are the most important features for accurately constructing a state at the critical point.

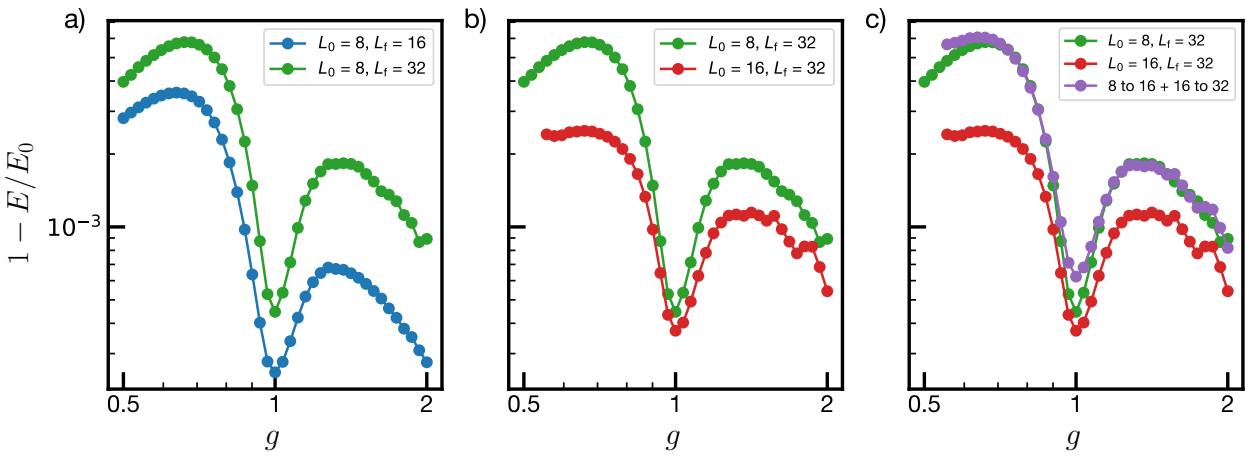

Figure 2.4: Relative energy error in the TFIM for multilayer circuits. a) Error comparison starting with $L_0 = 8$ for 1 and 2 layer circuits. b) Error comparison ending with $L_f = 32$ for 1 and 2 layer circuits. Error compounds reasonably with successive layers, and in particular is not much worse than single layer optimization at the critical point. c) We hypothesize that the multilayer error is subadditive, as illustrated here. Except where we have failed to find the global minimum, the $L_0 = 8$ to $L_f = 32$ error is bounded by the $L_0 = 8$ to $L_f = 16$ error plus the $L_0 = 16$ to $L_f = 32$ error, with the multilayer circuit substantially outperforming this bound at the critical point.

Moving away from the critical point, one sees the advantage of the next-nearest-neighbor circuit geometry; we will show in Sec. 2.4 that the range of individual gates in the circuit determines the scaling of the error with g deep in either phase.

2.3.3 Multilayer s-source

Our preceding discussion focuses on single-layer s-source, where one starts with a size L_0 input state and ends with a size $L_f = 2L_0$ final state. In multilayer s-source, we start from a size L_0 state and perform the s-source construction n times to get an approximate size $L_f = 2^n L_0$ state; we use the approximate state from one superlayer as the input state for the next. As aforementioned, in our numerics, we take a "greedy" approach where we optimize each superlayer in isolation rather than sweeping back and forth. In principle simultaneously optimizing superlayers should improve accuracy, but it would come at a substantial computational cost.

Fig. 2.4 depicts the energy errors for multilayer s-source for the TFIM as a function of both L_0 and L_f. Although it is difficult to make sharp statements, it appears that errors are not accumulating, per layer, super-linearly. We hypothesize that the multilayer error obeys

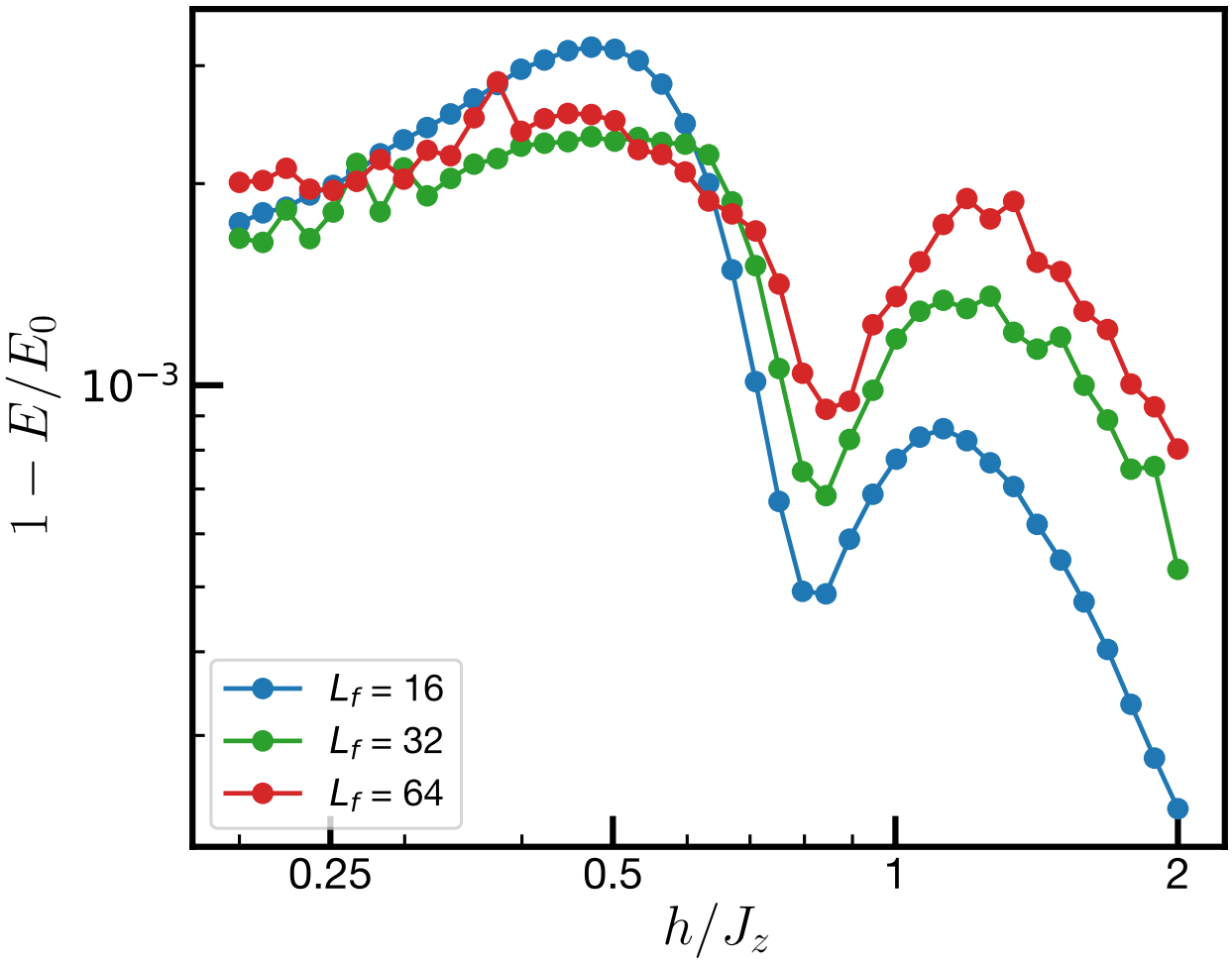

Figure 2.5: Relative energy error for the mixed coupling Ising model with $J_x = 0.1J_z$. The features of the error curve are qualitatively similar to the transverse field case, and the local minimum remains at the model's critical point.

the following bound:

$$\mathcal{E}_{L\to 4L} \leq \mathcal{E}_{L\to 2L} + \mathcal{E}_{2L\to 4L}, \tag{2.7}$$

where $\mathcal{E}_{L_0\to L_f}$ is the relative energy error for the optimal L_0 to L_f s-source state. The analogous statement for accumulated infidelities holds trivially (if one were to optimize the s-source circuit by minimizing infidelity instead of energy). In Fig. 2.4c, one can see that this proposed bound appears to hold for a two superlayer circuit.

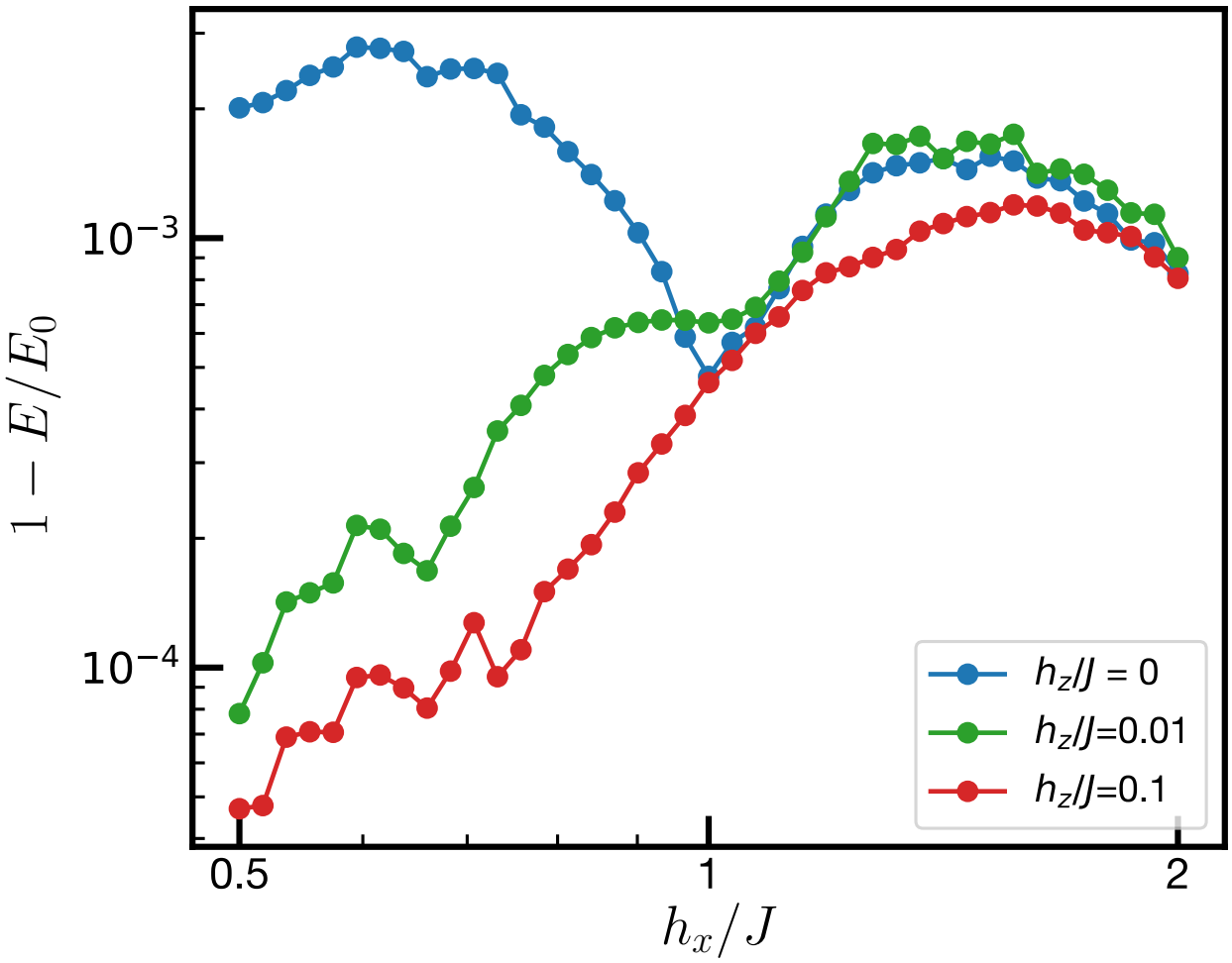

Figure 2.6: Relative energy error for the mixed field Ising model for $L_f = 64$. For sufficiently large h_z, there is no longer a local minimum in the error as there is no scale invariant point.

2.3.4 Non-integrable models

Finally, we now turn to applying the single-layer s-source algorithm to the non-integrable MCIM and MFIM models. In Fig. 2.5, we begin by showing the energy errors as a function of input size for the MCIM model. The qualitative features of the error curve are analogous to what we have already discussed in the TFIM case; the error decreases deep in either phase, and there is still a local minimum in the error at the phase transition. This minimum is consistent with our prior expectations since the critical point of the MCIM is still described by a conformal field theory. In Fig. 2.6, we plot the energy errors for a number of different longitudinal field strengths for the MFIM model. As h_z is increased, the local minimum flattens out and then vanishes, consistent with the lack of a scale invariant point.

2.4 Analytic analysis of errors

2.4.1 Analytic tensors in the large field limit

Our effort to express the adiabatic s-source unitary as a local, low-depth circuit faces two competing constraints. In order to have a good approximation, we need to be able to use both the adiabatic theorem (which requires that T^{-1} be small compared to the gap) and the Trotter decomposition (which requires that T^{-2} be large compared to commutators between different blocks of the Hamiltonian). In particular, in the large h/J limit of the TFIM, one can satisfy both of the above constraints. By moving into the interaction picture and expanding the time ordered exponential to leading order, we find (see Sec. 2.6.2 for details) that the nearest-neighbor ("on") unitaries are (Fig. 1), to leading order in h/J, given by $U = e^{-iH_{\text{eff}}}$, where

$$H_{\text{eff}} = -\frac{J}{8h}(\sigma_z^1\sigma_y^2 + \sigma_y^1\sigma_z^2). \tag{2.8}$$

Similarly, the next-nearest-neighbor ("off") unitaries (Fig. 1) are given by $U = e^{iH_{\text{eff}}}$ with the same H_{eff}.

One can perform the same calculation in the mixed field/coupling models. Defining $h = \sqrt{h_x^2 + h_z^2}$ and $\tan\eta = h_z/h_x$, we obtain an effective Hamiltonian

$$H_{\text{eff}} = \alpha(\sigma_x^1\sigma_y^2 + \sigma_y^1\sigma_x^2) + \beta(\sigma_y^1\sigma_z^2 + \sigma_z^1\sigma_y^2). \tag{2.9}$$

where

$$\begin{aligned}\alpha =& \frac{J_x}{32h}\left(7\sin\eta + 3\sin 3\eta\right) - \frac{3J_z}{8h}\cos^2\eta\,\sin\eta \\ \beta =& \frac{3J_x}{8h}\cos\eta\,\sin^2\eta - \frac{J_z}{32h}\left(7\cos\eta - 3\cos 3\eta\right)\end{aligned} \tag{2.10}$$

and again the "on" and "off" unitaries are given by $U = e^{-iH_{\text{eff}}}$ and $U = e^{iH_{\text{eff}}}$, respectively.

2.4.2 Perturbative analysis

In this subsection, we will use a perturbative analysis to explore how the error of the optimal s-source circuit varies with our system parameters. In our numerics, we are ultimately using a variational (in energy) method to solve for the circuit; thus, one cannot analytically calculate the error directly, but in a perturbative regime, we can compute how the leading order correction to the s-source wavefunction scales. As a bonus, this procedure naturally suggests additional tensors one could include in the circuit to further suppress errors. Though including such tensors would come with a computational cost for our numerical implementation, it is possible that they could be more natural for certain experimental geometries where long-range interactions are present [32, 33, 71–73].

Here we present the results of this analysis for the TFIM. Our basic strategy is to first figure out the exact s-source circuit at a fixed point (i.e. either $h/J = 0$ or $J/h = 0$), and

then to perturb around this fixed point. In other words, once we factor out the fixed point portion, we will parameterize each unitary in the circuit as $\exp(-iH) = \mathbb{I} - iH + \ldots$ with $\|H\| = \mathcal{O}(h/J)$ or $\mathcal{O}(J/h)$. We then consider whether there exists such a circuit that will take our initial state to the target state correctly to a given order in perturbation theory.

For the $J/h = 0$ fixed point (with ancillae inserted in the direction of the field), the s-source circuit is simply the identity and reproduces the size $2L$ ground state perfectly since both $|\psi^L\rangle$ and $|\psi^{2L}\rangle$ are product states. Deep in the paramagnetic phase, we can construct the correct size $2L$ ground state to linear order in J/h, and in fact, the circuit we use to do so is precisely based on the analytic unitaries found in the previous subsection. The leading order errors that remain are pairs of spin flips at sites $4i$ and $4i+4$ with coefficients of order $(J/h)^2$.

If we modify our circuit to contain two spin unitaries acting on pairs of spins located four sites away, we can construct the state *correctly* to order $(J/h)^2$. More generally, if one continues to add unitaries up to distance $2n$, one can faithfully construct the state to order $(J/h)^n$. The strategy is to first remove unwanted terms to bring the state back to the $J/h = 0$ state and then to build in the needed terms. Both distance n and $2n$ gates are required, the former to create the needed n^{th} order terms, and the latter to remove unwanted n^{th} order terms introduced when we add the ancillae. Furthermore, the effective Hamiltonians that parameterize these unitaries will be exponentially weak in distance, so the overall unitary will indeed be quasilocal as expected. Consistent with our numerical results, starting with a product state rather than the size L ground state allows us to do better; in particular, we will only need distance n gates in order to be correct to order $(J/h)^n$ since there are no unwanted terms to remove. We emphasize that this intuition is only true for sufficiently small J/h.

In the ferromagnetic phase things are a bit more subtle. We will denote the ground state which is "connected" to the symmetric cat state at $h = 0$ as $|\psi_0^L\rangle$ (even parity) and the analogous state which is connected to the anti-symmetric cat state as $|\psi_1^L\rangle$ (odd parity). The energy splitting between these states will scale like $(h/J)^L$. Were we to only care about energy errors, we might reasonably consider any linear combination of $|\psi_0^{2L}\rangle$ and $|\psi_1^{2L}\rangle$ to be our target state. However, we know that one cannot turn a product state into a cat state or vice versa with a circuit of sub-extensive depth. As previously discussed, at $h/J = 0$ one can go from a cat state input to a cat state output by inserting the ancillae in the $|\uparrow\rangle$ state and using CNOT gates for the bottom layer of the circuit. Thus, if our starting state is $|\psi_0^L\rangle$, then our target state will be $|\psi_0^{2L}\rangle$. We could also consider starting with either a product state or the symmetry breaking linear combination $(|\psi_0^L\rangle + |\psi_1^L\rangle)/\sqrt{2}$ and building towards $(|\psi_0^{2L}\rangle + |\psi_1^{2L}\rangle)/\sqrt{2}$; in this case the circuit at $h/J = 0$ is the identity. If we insist that the target is $|\psi_0^{2L}\rangle$ and begin with a product state input it is impossible to be correct to even 0^{th} order.

To this end, with the standard circuit (Fig. 2.1a), one can prepare $|\psi_0^{2L}\rangle$ correctly only to $\mathcal{O}(1)$, whereas for the symmetry broken or product inputs we can prepare $(|\psi_0^{2L}\rangle + |\psi_1^{2L}\rangle)/\sqrt{2}$ correctly to order h/J. The leading order error in the former case comes in the form of double spin flips on each of the two product states that make up the cat state. Using a three site

unitary with the third spin acting as a control would let us correct this error and prepare the true ground state correctly to order h/J. Similarly, blocks of $2n+1$ sites will allow us to correctly prepare the state to order $(h/J)^n$ by eliminating correlated $2n$ spin-flip errors. In contrast with the paramagnetic phase, where the long distance unitaries only needed to act on two sites, here the gates need to act on all of the sites within a block.

When targeting the symmetry broken state, the standard circuit will give us the correct answer to order h/J for both the product state and symmetry broken inputs. However, to correct higher order errors using $(|\psi_0^L\rangle + |\psi_1^L\rangle)/\sqrt{2}$ as an input requires $2n+1$-site unitaries to obtain the correct result at order $(h/J)^{n+1}$; the analogous situation with a product state input requires n site unitaries to be correct to order $(h/J)^n$. In all cases, the strengths of the required unitaries fall off exponentially with the diameter of the block, and the overall circuit is once again quasi-local.

2.5 Discussion and Conclusion

In this chapter, we have developed a numerical implementation of the s-source algorithm for finding approximate ground states of local Hamiltonians [2]. We approximate the lattice-doubling unitary of the s-source algorithm as an efficiently contractable tensor network, which we in turn variationally optimize to minimize the energy of the doubled-lattice ground state. To ensure our tensor network is efficiently contractable, we construct it from local rather than quasi-local components, although this decreases the accuracy of the approximation. We benchmark the resulting numerical algorithm on several 1D spin chain models, and find that the s-source construction works particularly well at scale-invariant critical points. We ascribe this to the fact that ancillae insertion doubles the length scale of all correlations in the input state, much in the same spirit as MERA. In addition, to gain some analytic intuition, we computed the scaling of the wavefunction errors deep in each phase of the TFIM, and determined how the s-source circuit could be modified to correct these errors. These corrections are consistent with the expectation that performing s-source with a quasi-local unitary should permit the exact construction of the doubled-lattice ground state.

Our work suggests several interesting directions for future study. First, one could use multi-layer s-source as a numerical method to extract information about renormalization group flow. When creating a multilayer s-source circuit, one obtains a sequence of unitaries U_1, U_2, ..., U_n that each double the size of the system. By parameterizing how this sequence of unitaries changes, it should be possible to follow the renormalization group flow and to extract quantities such as the operator dimension. In a similar vein, since the Hamiltonian parameters also flow, one might expect that the ideal input state to build $|\psi^{2L}(g)\rangle$ would not be $|\psi^L(g)\rangle$ but rather $|\psi^L(g')\rangle$, where the Hamiltonian parameter g' at length L flows to g at length $2L$. Allowing for this may significantly improve the performance of s-source away form criticality.

While we do not foresee s-source outperforming established methods like DMRG in determining 1D ground states, it may be useful for constructing ground states in 2D where existing

methods leave more room for improvement. Furthermore, the algorithm could be naturally adapted as an experimental method for preparing ground states. In fact, the ability to interleave ancillae has recently become possible in Rydberg optical tweezer arrays [32–34]. An experimental implementation of s-source would be particularly useful for generating states with long correlation lengths. Indeed, as we have previously discussed, strongly-correlated many-body states often require deep quantum circuits in order to be built from product states. Absent error correction, deep circuits result in low fidelities due to compounding gate errors. Thus, the ability of s-source to create certain classes of strongly-correlated states with low-depth circuits could provide a significant advantage in the NISQ era [74]. Finally, although the numerical implementation we explore here is variational, the s-source formalism provides a compelling connection to a non-variational ground-state construction which merits future exploration.

2.6 Supplemental information

2.6.1 Circuit optimization

Finding a quantum circuit that prepares a minimum energy eigenstate is a challenging problem [75, 76]. In the generic case, we cannot deterministically find the optimal circuit or even verify that a given circuit does minimize the energy. We can, however, perform a variational search by starting with some circuit and then iteratively updating component tensors in order to continually lower the energy, as is common practice for MERA.

Within a superlayer of the s-source circuit, we optimize each local unitary u while holding all others fixed. We then iterate this procedure for all u in the superlayer until the energy has converged. To update a single unitary, we utilize the optimization strategy outlined in [9]. To summarize, we pretend that the function we are trying to maximize, $f(u) = -\langle H \rangle$, is a linear function of u. Of course it is actually quadratic, as $u^\dagger$ is present in the dual circuit. If we treat $u^\dagger$ as constant, however, we can write $f(u) = \mathrm{tr}\big(W^\dagger u\big)$, where the environment $W^\dagger$ of u is found by contracting the tensor network formed by removing u from $-\langle H \rangle$'s tensor network. If W has singular value decomposition $W = XYZ^\dagger$, it follows that a linear function $f(u)$ achieves its maximum at $u = XZ^\dagger$.

For a nonlinear function of u, one should in principle update u multiple times until the energy converges. In practice, we only update each tensor u once during a full sweep of the superlayer; we have empirically found that this leads to a lower energy for a fixed total number of updates. We also tested an alternative optimization strategy referred to as "Linearization II" in [77], but this required using 10 updates per unitary per superlayer sweep for numerical stability, as well as tuning additional hyperparameters. We did not see any benefit of this approach for fixed computational cost.

As one might expect, this update procedure generally only finds a local energy minimum, not a global one. In order to get the global minimum we perform this optimization many times over circuits initialized with Haar-random unitaries. The cost of simulation is linear

in the number of samples, which can be large, so we note a few tricks that will improve either the speed or performance of optimization (although sampling over initializations is embarrassingly parallel).

First, we note that only a subset of the terms in the Hamiltonian will be within the light cone of a given u, so we only need to minimize the partial energy containing those terms when we update u. Crucially, the number of terms that contribute is *constant* as a function of system size, whereas the number of terms in the full Hamiltonian scales as L. We also note that each optimization step does not, generally, decrease the energy. For a quadratic function of a given u this procedure will actually maximize the absolute value of the function. In order to avoid this complication, we alter the spectrum of the (partial) energy we are minimizing to be negative-definite by shifting the partial hamiltonian by an appropriate multiple of the identity [8]: $\hat{h} \to \hat{h} - \alpha I$, where α is the maximum eigenvalue of the partial hamiltonian $\hat{h}$. In practice we find that we only need to do this for a few sweeps before all partial energies are negative, at which point we turn the shift off as it seems to slow down convergence (this suggests the possibility that shifting the spectrum *up* could speed up convergence as long as we are careful to keep things negative-definite).

We now describe some heuristics for efficient contraction of the next-nearest-neighbor $s = 1$ s-source circuit. Suppose we want to evaluate the expectation value of a term in the hamiltonian:

$$\langle \hat{O} \rangle = \langle \psi^L | U_1^\dagger \dots U_n^\dagger \hat{O} U_n \dots U_1 | \psi^L \rangle \tag{2.11}$$

where U_i is the ith superlayer of a multilayer s-source circuit. We start with the operator $\hat{O}$ (which is defined on the $2^n L$ site lattice) and then, in the language of MERA, act upon it with the ascending superoperator [9] (in other words, we conjugate by the innermost superlayer of the circuit). If $\hat{O}$ was supported on at most 6 adjacent sites, the ascended version of O will be supported on either 4 or 6 adjacent sites on the $2^{n-1}L$ spin lattice. This is because the causal cone extends by at most 6 sites, and contracting with the ancillae halves the support of the operator at the end.

We emphasize that we can ignore contraction with any gate in U_n outside of $\hat{O}$'s causal cone, since it will contract with its inverse in $U_n^\dagger$ to form an identity [9]. Therefore, there is no computational advantage to starting with a block of fewer than 4 sites (or 6 sites if the block would be ascended to a 6 site block), so if we want to evaluate the sum of expectation values of many operators, we should group them into blocks of operators living on either 4 or 6 adjacent sites. Doing so allows us to do a single contraction to find the sum of the expectation values of several adjacent local observables instead of multiple contractions to find the expectation value of each term separately. This reduces the time it takes to evaluate the expectation value of the hamiltonian considerably. Repeatedly applying ascending superoperators, we eventually obtain an operator defined on the L site lattice, which when contracted with the MPS and its dual will give the desired expectation value.

It is advantageous to cache various partial contractions of the MPS portion of the tensor network (i.e. $\langle \psi^L |$ and $| \psi^L \rangle$). In particular, at the final step of evaluating an expectation value, we will contract the ascended $\hat{O}$ with 4 or 6 pairs of adjacent physical indices of

the MPSs, with all other MPS indices already contracted. By storing all contractions of the MPSs with 4 or 6 pairs of adjacent dangling bonds, we can avoid repeating this costly computation. The evaluation of the $W^\dagger$s needed to optimize the circuit is done in much the same way, simply omitting the contraction with the specific u that is to be updated.

Energy minimization appears to take on the order of 1000 sweeps for the models we tested, with that number growing slightly with system size. This also varies from run to run; sometimes it might take 1000 sweeps, and sometimes it may take 10000. For most of the figures in this paper starting with an initial state of 32 spins and creating an s-source state of 64 spins we ran ~ 1000 initializations with 1000 sweeps each and took the best energy among them. For smaller systems, e.g. 8 to 16, we performed < 100 initializations.

We note that for this work we were particularly interested in characterizing the error of the s-source algorithm, and as such we needed to find the global minimum as reliably as possible. For some other applications, one may be perfectly content to have, say, twice the minimum error, in which case it is not as necessary to run so many randomly initialized optimizations. In this case one can often do pretty well by starting with a good guess for the initial circuit, adding some noise, and optimizing just a few initial states. For the TFIM, a good guess may be the leading order analytic solution that we discuss in Sec. 2.4.1, where noise is added by multiplying each unitary by another random unitary close to the identity. Here, we make two notes. First, with fewer parallel optimizations it is more important to do more sweeps for each one (several thousand rather than one thousand, say). Secondly, it is important to make sure that the initial condition of the circuit is not entirely real, as updating a real valued circuit will keep the circuit in the real manifold.

We note that further improvements are likely possible. It seems, for example, that it should be possible to reduce the average number of required sweeps by monitoring for convergence. However, checking for convergence can be quite deceptive here; one typically sees plateaus where the energy appears to converge, and then sudden jumps down to new local minima. A more careful analysis may reveal an effective way to anticipate whether or not further sweeps will result in an improved energy. In our experience, the energy would sometimes continue to improve beyond 1000 sweeps, but it was more efficient to sample more initial conditions than execute more sweeps per sample.

Finally, the cost of contraction scales roughly exponentially in the width of the circuit's causal cone. In practice, this might motivate the use of the simplified s-source circuit comprised of only the nearest-neighbor gates. We analyzed this circuit in Sec. 2.3 and found that the energy error was qualitatively similar to that of the circuit containing both nearest-neighbor and next-nearest-neighbor gates, and was quantitatively not much worse at the critical point.

2.6.2 Derivation of analytic unitaries for large magnetic fields

Here we derive the analytic expressions for the s-source unitaries of the TFIM in the limit $h \gg J$, previously described in Sec. 2.4.1. In this regime, we can simultaneously make the adiabatic evolution time T long enough to be adiabatic, but short enough that we can do a

Trotter expansion. The former condition requires, for $h \gg J$, $hT \gg 1$. In the interaction picture that we will consider shortly, the Trotter expansion requires $JT \ll 1$. We consider a single term in the Trotter expansion of Eq. 2.4 and thus reduce the problem to considering two spins that are initially in a field of strength h in the x direction and then turning on an interaction of strength J in the z direction. If we slowly turn on the interaction over a time T, then we have

$$H(t) = H_0 + \frac{t}{T} H_1 \tag{2.12}$$

with

$$H_0 = -h(\sigma_x^1 + \sigma_x^2) \tag{2.13}$$

$$H_1 = -J\sigma_z^1\sigma_z^2. \tag{2.14}$$

Then the adiabatic unitary associated with moving from H_0 to $H_0 + H_1$ is

$$U = \mathcal{T} \exp\left\{-i \int_0^T H(t)dt\right\}. \tag{2.15}$$

It is helpful for us to move to the interaction picture before proceeding. Doing so gives us the interaction picture unitary

$$U_I = \mathcal{T} \exp\left\{-i \int_0^T \frac{t}{T} e^{iH_0 t} H_1 e^{-iH_0 t} dt\right\} \approx 1 - i \int_0^T \frac{t}{T} e^{iH_0 t} H_1 e^{-iH_0 t} dt. \tag{2.16}$$

Upon integrating and discarding higher order terms, we get

$$U_I = 1 + i\left(\frac{JT}{4}(\sigma_z^1\sigma_z^2 + \sigma_y^1\sigma_y^2) + \frac{J}{8h} e^{-ih(\sigma_x^1+\sigma_x^2)T}(\sigma_z^1\sigma_y^2 + \sigma_y^1\sigma_z^2) e^{ih(\sigma_x^1+\sigma_x^2)T}\right). \tag{2.17}$$

Moving back to the Schrodinger picture and continuing to work to leading order,

$$\begin{aligned} U &= e^{-iH_0T} U_I = \left(e^{-iH_0T} U_I e^{iH_0T}\right) e^{-iH_0T} \\ &= 1 + i\left(hT(\sigma_x^1 + \sigma_x^2) + \frac{JT}{4}(\sigma_z^1\sigma_z^2 + \sigma_y^1\sigma_y^2) + \frac{J}{8h}(\sigma_z^1\sigma_y^2 + \sigma_y^1\sigma_z^2)\right) \\ &= \exp i\left(hT(\sigma_x^1 + \sigma_x^2) + \frac{JT}{4}(\sigma_z^1\sigma_z^2 + \sigma_y^1\sigma_y^2) + \frac{J}{8h}(\sigma_z^1\sigma_y^2 + \sigma_y^1\sigma_z^2)\right) \\ &= \exp(-iH_{\text{eff}}) \end{aligned} \tag{2.18}$$

which corresponds to an effective Hamiltonian

$$H_{\text{eff}} = -hT(\sigma_x^1 + \sigma_x^2) - \frac{JT}{4}(\sigma_z^1\sigma_z^2 + \sigma_y^1\sigma_y^2) - \frac{J}{8h}(\sigma_z^1\sigma_y^2 + \sigma_y^1\sigma_z^2). \tag{2.19}$$

We have not as of yet specified a value for T, so its presence in our effective Hamiltonian may appear, at first glance, to be troubling. However, we expect from the adiabatic theorem that, as long as the assumptions are met, there should be no strong T dependence. Indeed, one can explicitly verify that in the limit $T \gg J/h^2$ the effect of the T dependant terms is a phase shift. Dropping them, we end up with a particularly simple form for H_{eff}:

$$H_{\text{eff}} = -\frac{J}{8h}(\sigma_z^1\sigma_y^2 + \sigma_y^1\sigma_z^2). \tag{2.20}$$

The "off" unitaries, on the other hand, are given by $\exp\{(iH_{\text{eff}})\}$. We can see this by considering running the process backwards in time. This is, of course, just the "turn on" problem we just solved. There is one additional complication: these unitaries are acting not on the ground state, but on the first layer of the circuit. However, corrections due to the non-commutation of the the layers will come in at a higher order, and since we are only working to first order anyway we can simply ignore them.

We can repeat this analysis for a mixed coupling and field Ising model. Here we have hamiltonians

$$H_0 = -h_x(\sigma_x^1 + \sigma_x^2) - h_z(\sigma_z^1 + \sigma_z^2) \tag{2.21}$$

and

$$H_1 = -J_x\sigma_x^1\sigma_x^2 - J_z\sigma_z^1\sigma_z^2. \tag{2.22}$$

If we define $h = \sqrt{h_x^2 + h_z^2}$, $\tan\eta = h_z/h_x$, and go through the same steps, we find that to order J/h

$$\begin{aligned} H_{\text{eff,XX}} = &-\frac{J_xT}{32}\left(9 + 4\cos 2\eta + 3\cos 4\eta\right)\sigma_x^1\sigma_x^2 - \frac{J_xT}{4}\sin^2\eta\,\sigma_y^1\sigma_y^2 - \frac{3J_xT}{16}\sin^2 2\eta\,\sigma_z^1\sigma_z^2 \\ &-\frac{J_xT}{32}\left(2\sin 2\eta + 3\sin 4\eta\right)(\sigma_x^1\sigma_z^2 + \sigma_z^1\sigma_x^2) + \frac{J_x}{32h}\left(7\sin\eta + 3\sin 3\eta\right)(\sigma_x^1\sigma_y^2 + \sigma_y^1\sigma_x^2) \\ &+\frac{3J_x}{8h}\cos\eta\,\sin^2\eta\,(\sigma_y^1\sigma_z^2 + \sigma_z^1\sigma_y^2) \end{aligned} \tag{2.23}$$

$$\begin{aligned} H_{\text{eff,ZZ}} = &-\frac{3J_zT}{16}\sin^2 2\eta\,\sigma_x^1\sigma_x^2 - \frac{J_zT}{4}\cos^2\eta\,\sigma_y^1\sigma_y^2 - \frac{J_zT}{32}\left(9 - 4\cos 2\eta + 3\cos 4\eta\right)\sigma_z^1\sigma_z^2 \\ &-\frac{J_zT}{32}\left(2\sin 2\eta - 3\sin 4\eta\right)(\sigma_x^1\sigma_z^2 + \sigma_z^1\sigma_x^2) - \frac{3J_z}{8h}\cos^2\eta\,\sin\eta\,(\sigma_x^1\sigma_y^2 + \sigma_y^1\sigma_x^2) \\ &-\frac{J_z}{32h}\left(7\cos\eta - 3\cos 3\eta\right)(\sigma_y^1\sigma_z^2 + \sigma_z^1\sigma_y^2), \end{aligned} \tag{2.24}$$

with an overall effective hamiltonian $H_{\text{eff}} = H_0T + H_{\text{eff,XX}} + H_{\text{eff,ZZ}}$. If we again drop the T dependent terms, we get

$$\begin{aligned} H_{\text{eff}} = &\left(\frac{J_x}{32h}\left(7\sin\eta + 3\sin 3\eta\right) - \frac{3J_z}{8h}\cos^2\eta\,\sin\eta\right)(\sigma_x^1\sigma_y^2 + \sigma_y^1\sigma_x^2) \\ &+\left(\frac{3J_x}{8h}\cos\eta\,\sin^2\eta - \frac{J_z}{32h}\left(7\cos\eta - 3\cos 3\eta\right)\right)(\sigma_y^1\sigma_z^2 + \sigma_z^1\sigma_y^2). \end{aligned} \tag{2.25}$$

Chapter 3

Boundary Strong Zero Modes

3.1 Introduction

Fundamental to emerging quantum technologies is the capability to store and manipulate information in qubits in such a way that minimizes loss to the environment. In topological quantum computing, this is achieved by building qubits out of non-Abelian anyons, which are protected from local perturbations. However, at temperatures above the topological gap, interaction with thermally-excited quasi-particles can cause rapid decoherence [78–80]. In one dimension, it has been proposed that topological boundary modes can be decoupled from bulk thermal excitations by using strong quenched disorder to drive the system into a many-body localized phase [21, 81–83].

In fact, there exist translationally-invariant systems which host stable boundary degrees of freedom, even at infinite temperature. In such systems, the edge is unable to resonantly absorb or emit bulk excitations. Such long-lived edge modes across the entire spectrum are known as 'strong edge zero modes' (SZMs) [84, 85]. The terminology is in reference to the well-known topological Majorana zero modes in the Kitaev chain [86], but we stress that many examples, such as the transverse-field Ising model (TFIM), do *not* have corresponding topological edge modes in the ground state.

SZMs have been found in a diverse range of systems, not limited to one-dimensional or even time-independent Hamiltonions [12–20]. They are separated into 'exact' SZMs, which decouple the boundary completely from the bulk in the thermodynamic limit, and 'almost' SZMs, where the system eventually does thermalize, but parametrically slowly [87–89]. Recently, there has been a proposal to stabilize a qubit on a single edge of chain at infinite temperature with symmetry protected topological order using almost SZMs [90].

However, in topological computing, it is common for boundary modes to be constructed not on the edge of the system, but on the boundary between topological and trivial phases. Protocols can then be devised to easily manipulate qubits via controlling the location of the phase boundaries [91]. At finite temperature, such transport protocols could remain coherent by taking advantage of MBL [21], but, as in the static case, one might imagine SZMs render

disorder unnecessary. Indeed, in this paper we find that SZMs do exist on the boundary between phases and can provide dynamical protection to boundary degrees of freedom.

By definition, topological edge modes ought to be stable at both system boundaries and phase boundaries. However, we cannot rely on topological arguments at arbitrary temperatures, so the equivalent claim for SZMs is not at all manifest. The situation is even less clear for SZMs in systems without underlying topological edge modes. Though SZMs can survive in both cases, we shall describe how their nature is fundamentally different.

In particular, we focus on the one-dimensional transverse-field Ising model, and the same model after a Jordan–Wigner unitary transformation into a model of free Majorana fermions, the Kitaev chain. Under this transformation, the SZMs at the edge of these systems are the same. We show that for the Majorana fermions the SZM remains effectively unchanged at the boundary between a trivial and topological phase compared to the edge. In contrast, for certain choice of coupling strengths in the TFIM bulk excitations can resonantly pass through the boundary between a ferromagnet and a paramagnet, suppressing the SZM. Moreover, the SZM is preserved as long as this resonance condition is avoided, even between ferromagnetic regions with different Ising couplings. We explain how this difference is a natural consequence of the nonlocality of the Jordan–Wigner transformation that connects the two models.

This zero mode has another interesting property: it has poles in the coefficients of its operator expansion at only one location. In fact, we will argue that it is likely to be an *exact* SZM sufficiently far from this pole. We support this with both numerical and analytic evidence, and in particular show that a related toy model is provably exact despite also having a single pole. We summarize these scenarios in Table 3.1.

3.2 Edge strong zero modes

In Ref. [86], Kitaev considered a simple model of a 1D chain of fermions of length L sitting on a superconductor with a quadratic Hamiltonian:

$$H_{\mathrm{K}} = \sum_j \left(-w(c_j^\dagger c_{j+1} + c_{j+1}^\dagger c_j) - \mu(c_j^\dagger c_j - 1/2) + \Delta c_j c_{j+1} + \Delta^* c_{j+1}^\dagger c_j \right) \tag{3.1}$$

which can be transformed, after defining appropriate Majorana fermions a_j and b_j, into

$$H'_{\mathrm{K}} = \frac{i}{2} \sum_j \left(-\mu a_j b_j + (w + |\Delta|) b_j a_{j+1} + (-w + |\Delta|) a_j b_{j+1} \right). \tag{3.2}$$

One note: we will later define H_{Kitaev} as relevant to this chapter in terms of the magnetic field and coupling of the associated Ising model (where we will specialize to the case $|\Delta| = w$).

Kitaev then noted what happens at two special points. When $|\Delta| = w = 0$ and $\mu < 0$, the ground state is one where Majoranas a_j and b_j associated with site j are paired together (into the original c_js), and those modes are all unoccupied. If one instead considers the case

Phase 1	Phase 2	SZM	Exact	Resonances
Kitaev chain				
Vacuum	Topological	✓	✓	None
Trivial	Topological	✓	✓	None
Topological	Topological	×	×	|
Transverse-field Ising model				
Vacuum	Ferromagnetic	✓	✓	None
Paramagnetic	Ferromagnetic	✓	✓	Single
Ferromagnetic	Ferromagnetic	✓	✓	Single
TFIM with interactions				
Any	Ferromagnetic	✓	×	Multiple
XXZ chain				
Vacuum	Ferromagnetic	✓	✓	None
Ferromagnetic	Ferromagnetic	✓	?	Single
XY	Ferromagnetic	✓	?	None

Figure 3.1: Summary of strong zero mode properties on various system edges and boundaries.

$|\Delta| = w > 0$ and $\mu = 0$, however, the Majorana hamiltonian is almost the same as in the first case, except instead of a_j and b_j being coupled, b_j and a_{j+1} are coupled instead. One can then define *new* dirac fermions in terms of b_j and a_{j+1}, and the ground state will be such that all of these modes are unoccupied. But in this case there's a small but crucial difference: a_1 and b_L don't enter the Hamiltonian at all!

Because of this, the ground state of the model must be doubly degenerate based on the occupation of the dirac fermion made from a_1 and b_L. In fact, these two cases are special points in two phases of the model, the first of which is a trivial phase and the second of which is topogically ordered. The zero modes in the second case approximately exist whenever $2|w| > |\mu$ and $\Delta \neq 0$, but now enter the Hamiltonian with a coupling exponentially small in L. Because this is a topologically ordered phase, a_1 and b_L are topological zero modes.

One can go beyond the concept of a topological zero mode to consider modes that split a system's *entire spectrum* into pairs (or triples, etc) of degenerate states. In Ref. [85], Alicea and Fendley named such an object a strong zero mode. As it turns out, the zero modes in the Kitaev model actually are strong zero modes as well as topological zero modes.

Let us now detail the mathematical definition and basic physical consequences of a SZM at the edge of the system, to set the stage for our study of SZMs at the boundary between different phases. An exact strong zero mode is a quasilocal operator Ψ such that Ψ com-

mutes with the Hamiltonian up to an error exponentially small in the size of the system, Ψ anticommutes with a discrete symmetry of $\mathcal{F}$ of the model, and $\Psi^2 = 1$ [87] [1].

Physically, the existence of a SZM implies that observables with large overlap with the SZM will evolve slowly; i.e. they will retain memory of their initial state for anomalously long times. For example, consider the infinite temperature autocorrelator of the edge spin magnetization $A_\infty(t) = \langle \sigma_0^z(t)\sigma_0^z(0)\rangle_{T=\infty}$. If the system supports an exact SZM with finite overlap with the edge spin – for example, if $\Psi^{(0)} = \sigma_0^z$ – then by definition the decay time of this autocorrelator will be infinite in the thermodynamic limit, i.e. $\lim_{t\to\infty}\lim_{M\to\infty} A_\infty(t) \neq 0$.

The simplest possible example of an exact SZM occurs at the edge of the 1D transverse field Ising model (TFIM):

$$H_{\text{Ising}} = -J\sum_{j=0}\sigma_j^z\sigma_{j+1}^z - h\sum_{j=0}\sigma_j^x. \tag{3.3}$$

The TFIM can also be transformed using the non-local Jordan–Wigner (JW) transformations, by defining Majorana fermion operators[92, 93]

$$a_j = \left(\prod_{k=0}^{j-1}\sigma_k^x\right)\sigma_j^z, \qquad b_j = i\left(\prod_{k=0}^{j}\sigma_k^x\right)\sigma_j^z, \tag{3.4}$$

into a free-fermion Hamiltonian equivalent to the Kitaev chain

$$H_{\text{Kitaev}} = -iJ\sum_{j=0} b_j a_{j+1} - ih\sum_{j=0} a_j b_j. \tag{3.5}$$

We also note that this model has the global spin flip symmetry

$$\mathcal{F} = \prod_{j=0}\sigma_j^x = i^L\prod_{j=0} a_j b_j \tag{3.6}$$

where L is the system size. If we consider the TFIM with no transverse magnetic-field term, $H_0 = H_{\text{Ising}}[h=0]$, it's easy to see that $\Psi^{(0)} = \sigma_0^z$ commutes with H_0, anticommutes with the global spin flip symmetry, and squares to the identity. It is, therefore, an edge SZM of H_0.

We can easily use the iterative construction outlined in Ref. [13] to generalize this SZM to any finite h still in the ferromagnetic phase of the TFIM. One first writes $H = H_0 + V$ and expresses the SZM of H as

$$\Psi = \sum_{n=0}\Psi^{(n)} \tag{3.7}$$

[1] Here we are assuming that $\mathcal{F}^2 = 1$; we note that in systems where $\mathcal{F}^n = 1$ for $n > 2$, these criteria will be appropriately modified (e.g. in parafermionic systems) [12, 13, 85].

where $\Psi^{(n)}$ is n^{th} order in the perturbation V. Then because $[H, \Psi] = 0$, collecting the terms of order $n+1$ tells us that

$$[H_0, \Psi^{(n+1)}] = -[V, \Psi^{(n)}]. \tag{3.8}$$

In our current example, $[V, \Psi^{(0)}] = 2ih\sigma_0^y$. One can confirm that $\Psi^{(1)} = (h/J)\sigma_0^x\sigma_1^z$ satisfies Eq. 3.8. The commutator on the left hand side of Eq. 3.8 is not uniquely invertible since we could always add an operator that commutes with H_0 to $\Psi^{(n+1)}$; we can resolve this ambiguity by demanding that $\Psi^2 = 1$ to the appropriate order.

For the TFIM, one can continue this process to infinite order in a straightforward manner; one obtains (after normalizing) [87]

$$\Psi_{\text{Ising}} = \sqrt{1 - \left(\frac{h}{J}\right)^2} \sum_{j=0} \left(\frac{h}{J}\right)^j \sigma_j^z \prod_{k=0}^{j-1} \sigma_k^x. \tag{3.9}$$

Similarly, starting with $\Psi^{(0)} = a_0$ (NB: $a_0 = \sigma_0^z$ under the JW transformation, Eq. (3.4)), the SZM for the Kitaev chain is found to be

$$\Psi_{\text{Ising}} = \sqrt{1 - \left(\frac{h}{J}\right)^2} \sum_{j=0} \left(\frac{h}{J}\right)^j a_j, \tag{3.10}$$

which we could also have obtained directly with a JW transformation of the spin expression.

3.3 Boundary strong zero mode in the transverse field Ising model

In order to consider the boundary between phases we will couple the ends of two chains with different coupling constants together:

$$H_{\text{BI}} = -J_1 \sum_{j=-\infty}^{-1} \sigma_j^z\sigma_{j+1}^z - J_2 \sum_{j=0}^{\infty} \sigma_j^z\sigma_{j+1}^z - h_1 \sum_{j=-\infty}^{-1} \sigma_j^x - h_2 \sum_{j=0}^{\infty} \sigma_j^x. \tag{3.11}$$

Here $J_{1(2)}$ and $h_{1(2)}$ are the Ising coupling and transverse field on the left- (right-) hand chain of the system respectively. The two chains are coupled by J_1 at site 0; see Figure 3.2. If $J_1 = 0$, then the uncoupled second chain would exhibit a phase transition as h_2 is increased between a ferromagnet and paramagnet at $h_2 = J_2$.

As before, this model can also be transformed into two end-to-end coupled Kitaev chains using JW transformations by defining Majorana fermion operators

$$a_j = \left(\prod_{k=-\infty}^{j-1} \sigma_k^x\right) \sigma_j^z, \qquad b_j = i \left(\prod_{k=-\infty}^{j} \sigma_k^x\right) \sigma_j^z \tag{3.12}$$

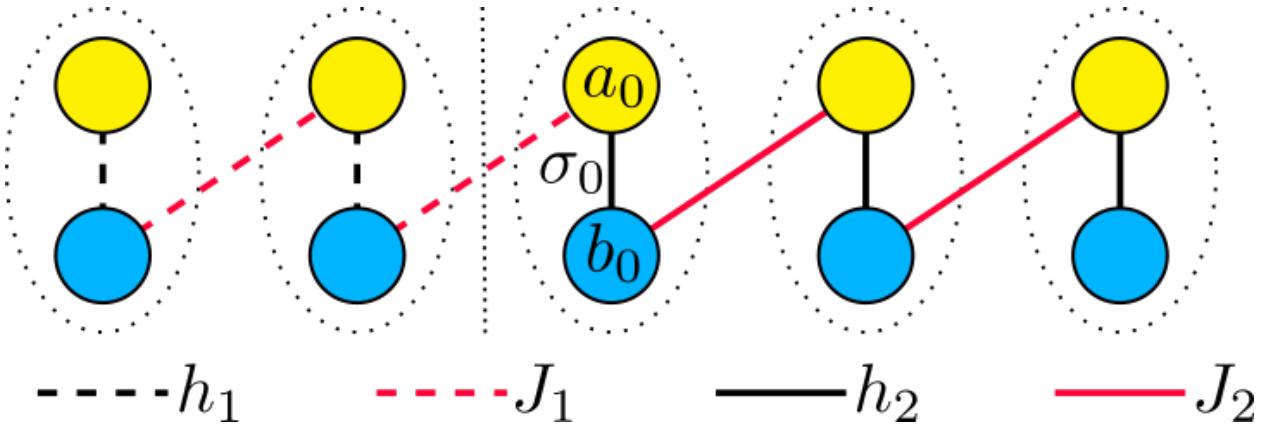

Figure 3.2: Schematic of the boundary Ising model. The ovals denote the spins and the circles the constituent Majorana fermions.

to find the corresponding free-fermion Hamiltonian

$$H_{\mathrm{FBI}} = -iJ_1 \sum_{j=-\infty}^{-1} b_j a_{j+1} - iJ_2 \sum_{j=0}^{\infty} b_j a_{j+1} - ih_1 \sum_{j=-\infty}^{-1} a_j b_j - ih_2 \sum_{j=0}^{\infty} a_j b_j. \tag{3.13}$$

Focusing again on the uncoupled case $J_1 = 0$, the second chain supports a familiar Majorana zero-mode if $J > h$ [86]. In fact, it has been shown that the edge supports not only this famous topological edge mode in the ground state, but furthermore an exact SZM acting on the entire spectrum. The edge mode is given by a_0 with an exponential tail into the bulk [84]. Taking the Jordan–Wigner transformation of this Majorana fermion SZM yields an edge-localized spin operator starting at σ_0^z. This operator is also an exact SZM, even though the TFIM itself has *no* topological edge modes.

It is well-known that *topological* zero modes exist on the boundary between trivial and topological phases, not just on the edge. For example, in our system, the topological edge mode at a_0 survives if we turn on the J_1 coupling between chains as long as the first chain remains in the trivial phase, $J_1 < h_1$. By constructing the SZM perturbatively with respect to the small couplings J_1 and h_2, from the usual zeroth order ansatz $\Psi_{\mathrm{FBI}}^{(0)} = a_0$ [87], we find that an exact SZM also exists at this boundary:

$$\Psi_{\mathrm{FBI}} = \mathcal{N}_{\mathrm{FBI}} \left(a_0 + \sum_{j=1}^{\infty} \left(\left(\frac{J_1}{h_1} \right)^j a_{-j} + \left(\frac{h_2}{J_2} \right)^j a_j \right) \right) \tag{3.14}$$

with

$$\mathcal{N}_{\mathrm{FBI}}^2 = \frac{(1 - (J_1/h_1)^2)(1 - (h_2/J_2)^2)}{1 - (J_1 h_2 / J_2 h_1)^2}. \tag{3.15}$$

Ψ_{FBI} is the same as the exact SZM of the uncoupled second chain, but now dressed by an additional tail into the trivial phase as well as the topological phase. The physics of the

edge and boundary modes are thus essentially the same: in the thermodynamic limit, the autocorrelator will decay to a non-vanishing value given by the normalization $\mathcal{N}^2_{\mathrm{FBI}}$.

We stress that this result does not immediately follow from the existence of the topological edge mode at the boundary. The topological physics occurs at energy densities below the gap; for the SZM, we are interested in infinite temperature behavior.

In this boundary model, the SZM does not start at the edge of the chain, but at the center, at site 0. The operator in the spin boundary Ising model corresponding to a_0 in the fermionic boundary Ising model is not simply σ^z_0, but instead the highly nonlocal operator $\left(\prod_{k=-\infty}^{-1}\sigma^x_k\right)\sigma^z_0$, as it picks up a Jordan–Wigner string from the first chain on the left. Thus, the existence of Ψ_{FBI} does not imply the existence of an SZM at a phase boundary in the TFIM. This is true regardless of how we chose to define our Jordan–Wigner strings (see Sec. 3.7 for more details).

In order to elucidate the difference between spins and Majorana fermions, we again calculate the boundary zero mode perturbatively, but starting from the boundary spin σ^z_0 as our zeroth order estimate for the purported SZM. This time the number of terms grows rapidly in the order n. The first two corrections beyond the zeroth order term $\Psi^{(0)}_{\mathrm{BI}} = \sigma^z_0$ are

$$\Psi^{(1)}_{\mathrm{BI}} = \frac{h_2}{J_2}\sigma^x_0\sigma^z_1 \tag{3.16}$$

$$\Psi^{(2)}_{\mathrm{BI}} = \frac{h_2^2}{J_2^2}\sigma^x_0\sigma^x_1\sigma^z_2 - \frac{J_1h_2}{J_2^2-h_1^2}\sigma^z_{-1}\sigma^x_0 + \frac{J_1h_1h_2}{J_2(J_2^2-h_1^2)}\sigma^y_{-1}\sigma^y_0\sigma^z_1 - \frac{h_2^2}{2J_2^2}\sigma^z_0. \tag{3.17}$$

Immediately we see a stark contrast with the fermionic SZM. Instead of the SZM breaking down at the phase transition $h_1 = J_1$, there is a pole in the expansion at $J_2 = \pm h_1$ in (3.17). These divergent terms in the pertubation theory are called 'resonances', and are caused by energy-conserving processes which change the boundary degrees of freedom [87]. For example, the poles at $h_1 = \pm J_2$ appearing at second order describe the process in which a spin-flip excitation of the paramagnetic chain converts resonantly into a domain-wall excitation of the ferromagnetic chain.

Physically, the appearance of such resonances typically signal that the autocorrelation time is no longer infinite, but ultimately decays to zero. This is because the perturbative expansion of the SZM no longer converges: instead, we are forced to truncate the series before divergent terms appear. This is known as an 'almost', rather than exact, SZM. In other models with known almost SZMs, such as the Ising model with added next nearest neighbor interactions [87], parafermions [12, 16, 84] and the ZXZ model [90], there are an increasing number of different rational values of ratios of the couplings for which there are poles as we go to higher orders in Ψ, representing more and more complicated resonant processes which only appear at higher order.

In our boundary Ising model, however, there is a crucial difference: no further poles emerge; poles at all higher orders are still at $h_1 = \pm J_2$. This can be intuitively understood as the integrability of the model preventing any resonant processes except for the conversion of a single domain wall into a single spin-flip. For example, naively our argument above suggests

a pole should exist at $h_1 = \pm 2J_2$, because we could convert *two* domain walls resonantly into a single spin flip at the boundary. In a non-integrable model, this argument would be correct; however, it is not possible to construct such a three-body resonant conversion at the boundary in an integrable model without it factoring into two two-body processes, one of which does not involve the boundary degree of freedom [94].

As there is only a single resonance, it is not inevitable that the SZM expansion will fail to converge. Indeed, we will now provide convincing numerical and analytical evidence that sufficiently far from this single pole the iterative construction of the boundary zero mode does converge, and there is an *exact* SZM at the boundary of a paramagnetic and ferromagnetic regime in the TFIM. Furthermore, the lack of dependence on the phase transition at $h_1 = J_1$ suggests repeating the calculation above for $J_1 > h_1$. This reveals the SZM is still present at the boundary of two ferromagnetic regions as well, where now the pole is at $J_1 = \pm J_2$. Thus for the spin boundary model a phase boundary is not even a prerequisite for an exact SZM—indeed, the left-hand chain can even be critical, $J_1 = h_1$.

3.4 Exactness of the Spin SZM

We can calculate the autocorrelation time of the edge spin σ_0^z numerically from the free fermion results. Because of the Jordan–Wigner string, this requires the calculation of a many-point correlator, which can be broken down into two-point correlators using a modified version of Wick's theorem for Majorana fermions [95]. In Fig. 3.3 we plot the autocorrelator for the spin at the ferromagnetic-ferromagnetic boundary. Outside the resonance the autocorrelation time increases exponentially with system size [96]. In stark contrast, close to the resonance the autocorrelator immediately decays.

We plot the amplitude of the long-lived component of the autocorrelator of σ_0^z in Fig 3.4. If the SZM is exact, this is the asymptotic value of the autocorrelator in the thermodynamic limit. Unlike for the fermions, we observe that the location of the phase transition is unimportant: rather, the amplitude dramatically decreases around the resonance. The width of this resonance does not increase with system size, suggesting that it remains finite in the thermodynamic limit, and outside the resonance the SZM is exact. This resonance can be understood intuitively as the range of couplings in which excitations in the left-hand chain can move into the right-hand chain without any change in the overall energy of the system. For the disconnected chains, the energy spectrum of the excitations may be calculated exactly, and their bandwidth is linear in the transverse fields. This explains the corresponding linear growth in the width of the resonance in the autocorrelation time as a function of h_1 and h_2 observed in the inset of Fig 3.4.

Analytically, if the SZM is exact, the operator expansion should converge to all orders in perturbation theory. We present two results in Sec. 3.8 suggesting that this indeed the case. Firstly, using simple combinatorial arguments, we bound the number of terms that first appear at order n in perturbation theory to a subexponential in n. Secondly, we have solved exactly a simple toy model where the semi-infinite chain on the left of the boundary is

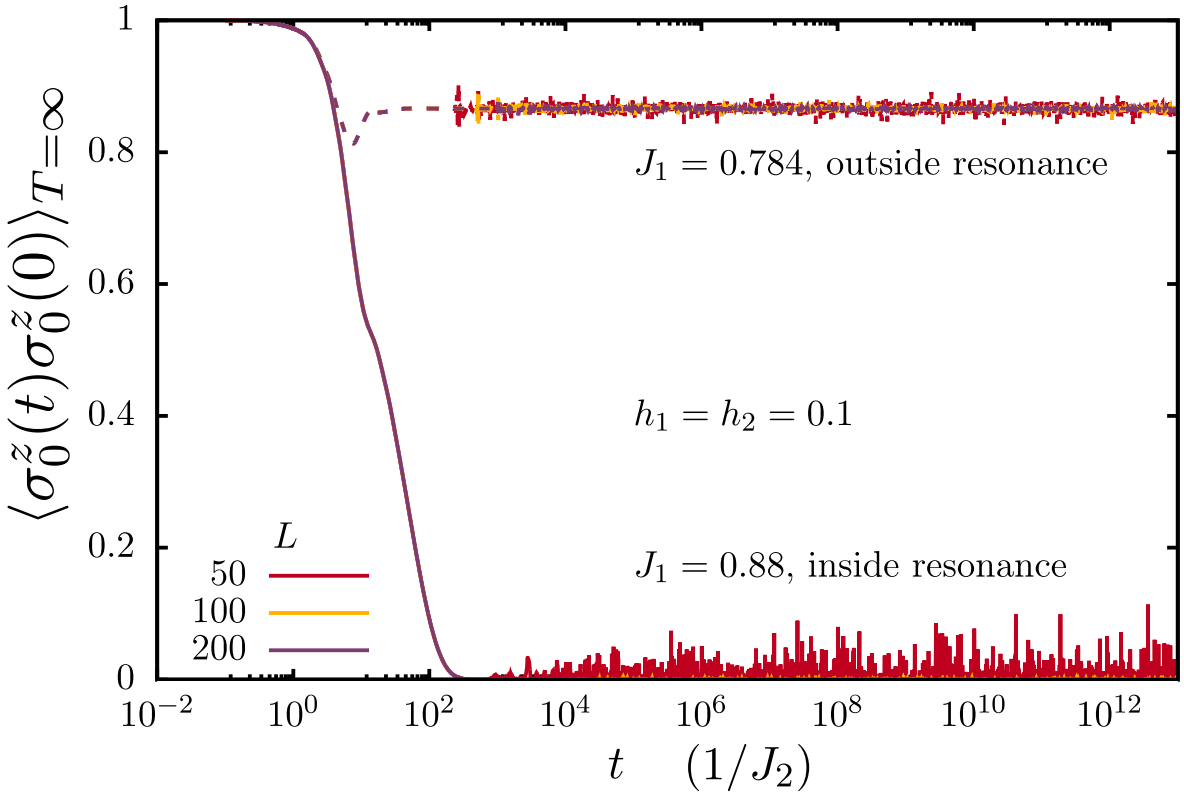

Figure 3.3: The autocorrelator for the spin at the boundary of the boundary transverse-field Ising model for various systems sizes L for a value of J_1 a) outside the resonance, b) inside the resonance.

replaced by a single spin. The solution is valid for all choices of the couplings J_1 and h_1 on the left-hand chain, unless proximity to the resonance prohibits convergence. We confirm that the normalization extracted from this solution agrees precisely with numerics, see Fig 3.5. The boundary Ising model with a single spin at the edge, is, therefore, an exact SZM within the radius of convergence, despite the existence of a pole.

Although the full solution is quite complicated and involves powers of the generating function for the Narayana numbers [97], it is instructive to consider the even simpler case $h_1 = 0$. The solution for the SZM reduces to:

$$\Psi_2 = \mathcal{N}_2 \sum_{n,m=-1}^{\infty} C_{nm} \sigma_{-1}^x \left(\prod_{k=-1}^{n} \sigma_k^x \right) \sigma_{n+1}^z \left(\prod_{k=-1}^{m} \sigma_k^x \right) \sigma_m^z$$

$$C_{nm} = \left(\frac{J_1}{J_2} \right)^{\mathbf{1}_{m>-1}} \left(\frac{h_2 J_2}{J_2^2 - J_1^2} \right)^{n+1} \left(\frac{h_2 J_2}{J_2^2 - J_1^2} \right)^{m+1},$$

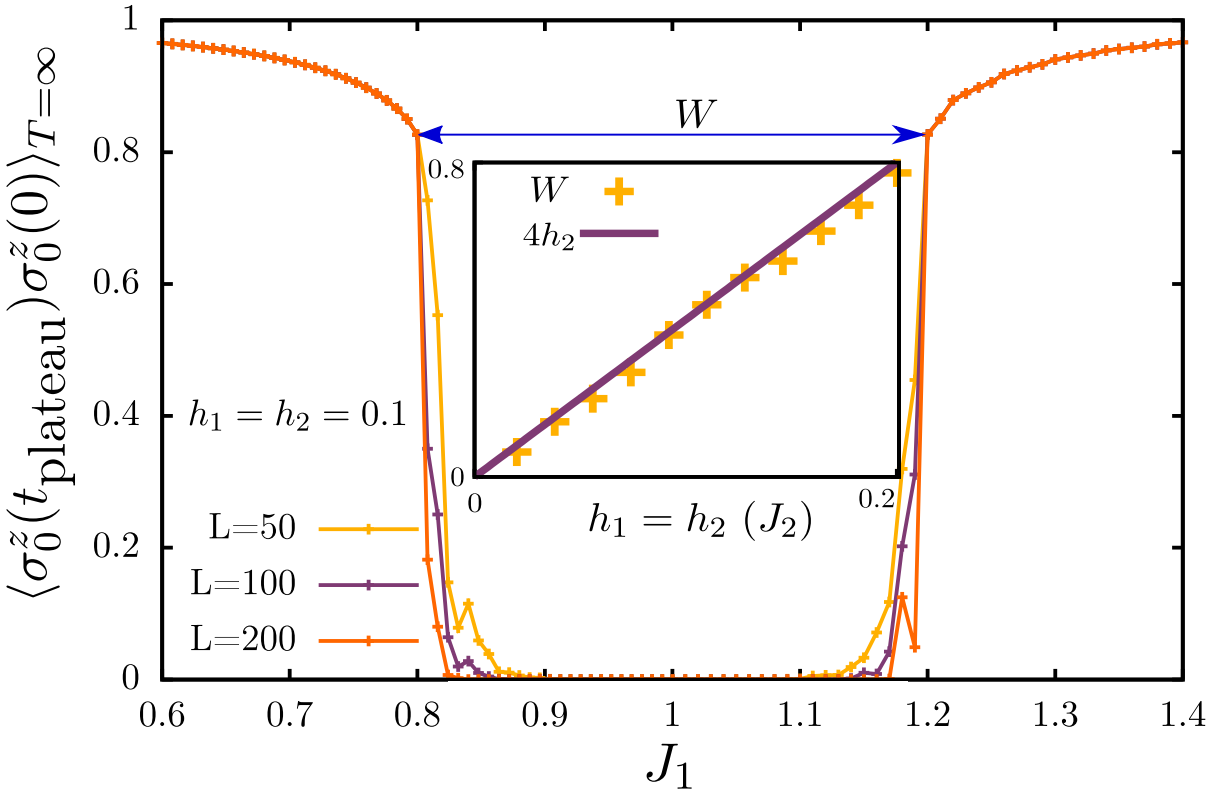

Figure 3.4: The amplitude of the long-lived component of the autocorrelator for the spin at the boundary of the boundary transverse-field Ising model for various systems sizes L as the coupling h_1 is varied, for $J_2 = 1.0$, $J_1 = h_2 = 0.1$. Nearby $J_1 = J_2$ a resonance suppresses the SZM. **Inset:** The width of the resonance at $h_1 = J_2$, as a function of $h_2 = J_1$. This is estimated from the value of h_1 for which the plateau value of the autocorrelator falls below 0.8 or above 1.2.

where $\mathbf{1}_{m>-1} = 1$ if $m > -1$ and otherwise vanishes. It is evident Ψ_2 is normalizable as long as $h_2 J_2/(J_2^2 - J_1^2) < 1$, with a normalization factor:

$$\mathcal{N}_2 = \frac{1}{\sqrt{1 - \frac{h_2^2}{J_2^2 - J_1^2}}} \left(1 - \left(\frac{h_2 J_2}{J_2^2 - J_1^2}\right)^2\right). \tag{3.18}$$

3.5 Interactions

The systems we have so far consider constitute a special case as they are not only integrable but free. We now consider adding interactions. We have two possibilites: most naively, we

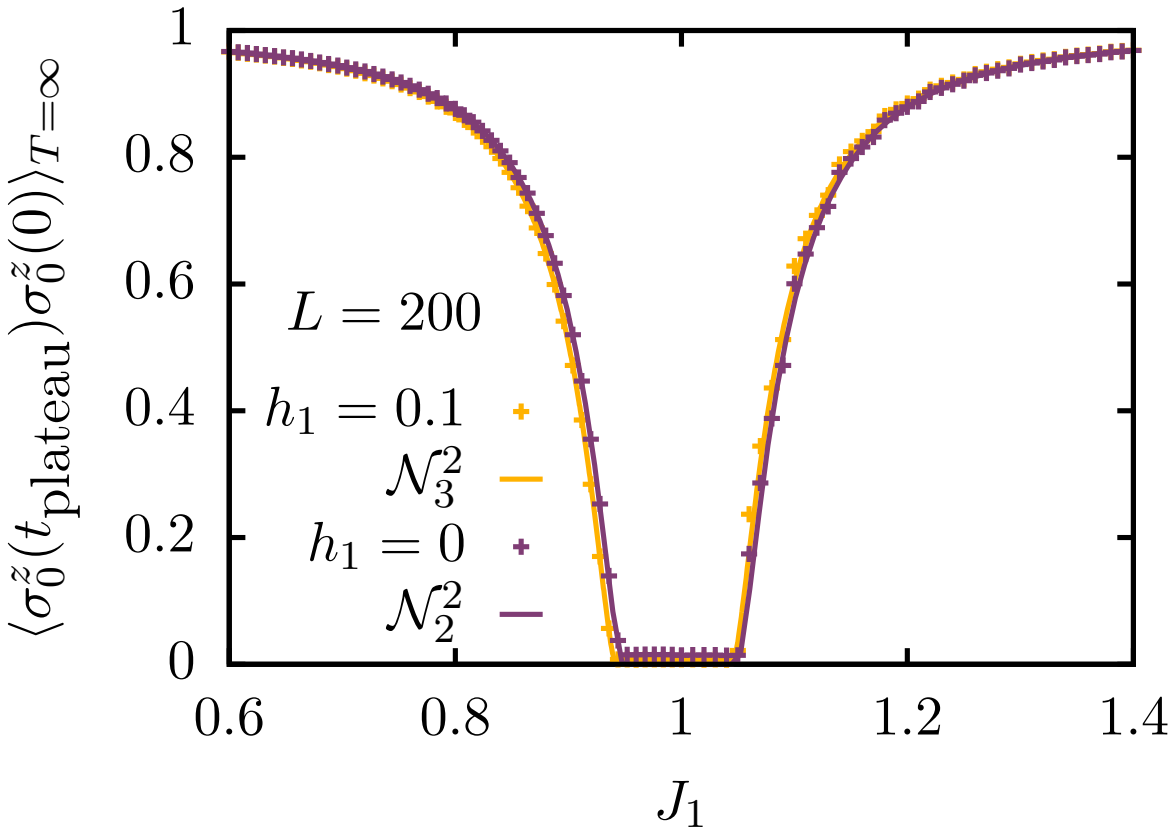

Figure 3.5: The amplitude of the long-lived component of the autocorrelator for a toy model with a single spin at the edge. The numerical and corresponding analytical results agree precisely.

can add integrability breaking interactions, but we can also consider integrable but interacting systems. To study a non-integrable, interacting system we add nearest-neighbor XX interactions as a perturbation to our coupled TFIM chains of the form $-K\sum_{j=-\infty}^{\infty}\sigma_j^x\sigma_{j+1}^x$, with $K \ll J_2$.

With these terms added, both spin and fermion models now have an almost SZM rather than an exact SZM, with additional resonances appearing at higher order in perturbation theory. For example, in addition to resonances at $J_2 = \pm J_1$, $\Psi^*_{\text{BI+XX}}$ also has poles starting at third order at $J_2 = \pm(3)^{\pm 1}J_1$, and generically at order $p+q-1$ for $J_2 = \pm(p/q)^{\pm 1}J_1$ for p, q odd integers.

Numerically, we can extract the decay time from the time taken for the autocorrelator to fall below a threshold value, Fig. 3.6. Even for large values of the interaction strengths, we see that the boundary degrees of freedom have significantly enhanced lifetimes. Additionally, the effect of the resonances can be seen as dips in the autocorrelation times exactly at the

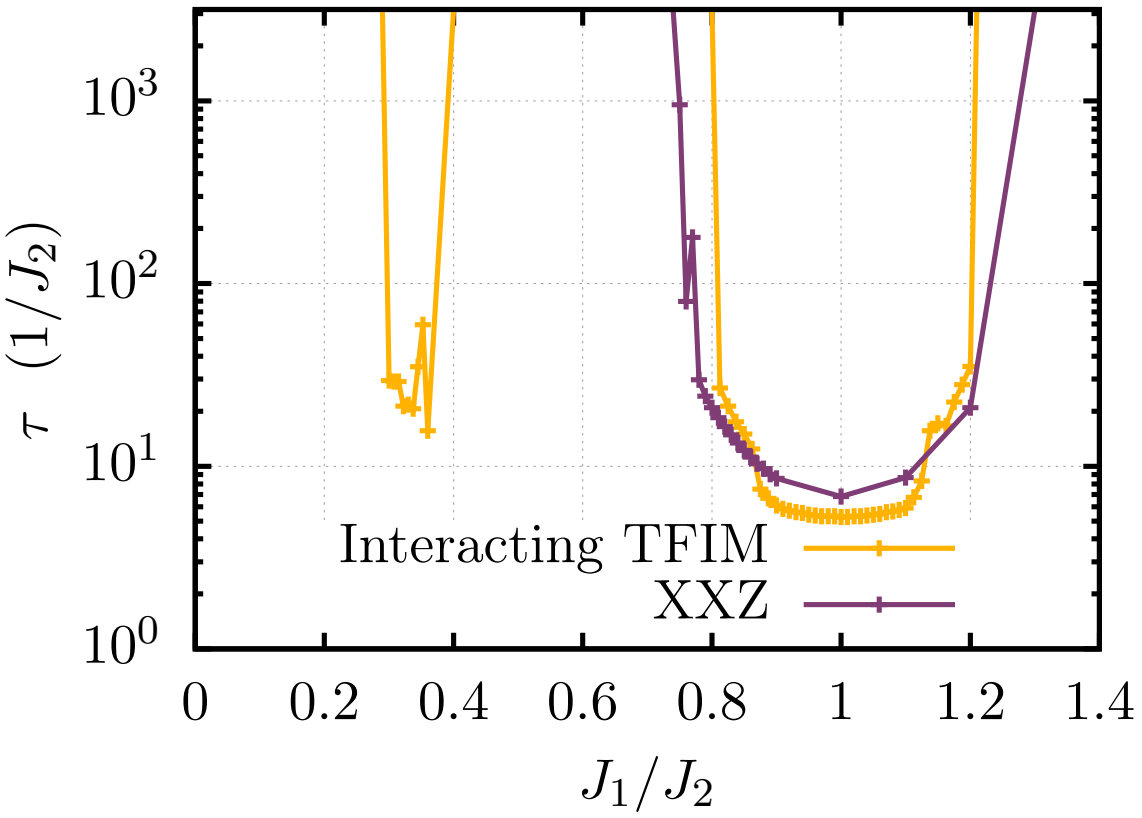

Figure 3.6: The decay time for the boundary spin σ_0^z between ferromagnetic and paramagnetic regimes in the presence of interactions for system size $M = 24$ and $h_1 = h_2 = 0.1J_2$ from Krylov subspace methods [98]. Other than at the poles at $J_1 = J_2$ and $J_2/3$ the decay time is longer than the evolution time.

values predicted above.

For integrable systems, we do not expect this proliferation of resonances, as we have discussed. For example, consider coupling two XXZ chains end-to-end together as we coupled the two TFIM chains:

$$\begin{aligned} H_{\mathrm{XXZ}} = &- \sum_{j=-\infty}^{-1} \left[J_1 \sigma_j^z \sigma_{j+1}^z + h_1 (\sigma_j^x \sigma_{j+1}^x + \sigma_j^y \sigma_{j+1}^y) \right] \\ &- \sum_{j=0}^{\infty} \left[J_2 \sigma_j^z \sigma_{j+1}^z + h_2 (\sigma_j^x \sigma_{j+1}^x + \sigma_j^y \sigma_{j+1}^y) \right] . \end{aligned} \tag{3.19}$$

As for the TFIM, we will set the second chain to always be ferromagnetic, $J_2 > h_2$. If $J_1 < h_1$, then the first chain is gapless, and there are no resonances: the SZM exists if and

only if h_1 is sufficiently smaller than J_2. On the other hand, if both chains are ferromagnetic, there is a single resonance at $J_1 = J_2$; see Fig 3.6.

3.6 Outlook

A number of natural research questions follow from our work. Most directly, the exactness of the SZM in the boundary TFIM must still be proven analytically. Furthermore, it is possible that the boundary SZM is also exact for interacting integrable systems, such as the XXZ chain, which is known to host an exact SZM at the edge. If so, it may be possible to relate this conserved quantity to the hierarchy of conserved quantities that have recently been constructed in the XXZ chain [99–101]. For practical purposes, it will be important to study how stable the SZMs are under dynamical protocols to manipulate them by moving the phase boundaries [21].

3.7 Choice of Jordan–Wigner String

In the main sections, we choose a Jordan–Wignerization starting from the left edge of the system. This means that the operator in the spin boundary Ising model corresponding to a_0 in the fermionic boundary Ising model is not simply σ_0^z, but instead the highly nonlocal operator $\left(\prod_{k=-\infty}^{-1} \sigma_k^x\right) \sigma_0^z$. Starting from the fermionic Hamiltonian, a natural choice for a different set of JW transformations is one that maintains an exact correspondence between a_0 and σ_0^z. In order to do this, we define a new string operator that starts at the center of the chain at site 0 and then wraps around from $+\infty$ to $-\infty$:

$$a_j = \begin{cases} \left(\prod_{k=-\infty}^{j-1} \sigma_k^x\right) \left(\prod_{k=0}^{\infty} \sigma_k^x\right) \sigma_j^z & j < 0 \\ \left(\prod_{k=0}^{j-1} \sigma_k^x\right) \sigma_j^z & j \geq 0 \end{cases} \tag{3.20}$$

$$b_j = \begin{cases} i\left(\prod_{k=-\infty}^{j} \sigma_k^x\right) \left(\prod_{k=0}^{\infty} \sigma_k^x\right) \sigma_j^z & j < 0 \\ i\left(\prod_{k=0}^{j} \sigma_k^x\right) \sigma_j^z & j \geq 0 \end{cases}. \tag{3.21}$$

Under such a JW transformation, a_0 trivially transforms into σ_0^z, allowing us to directly compare the strong zero modes living on the boundary. However, the Hamiltonian H_{BI} also changes:

$$H'_{\mathrm{BI}} = -J_1 \sum_{j=-\infty}^{-2} \sigma_j^z \sigma_{j+1}^z - J_2 \sum_{j=0}^{\infty} \sigma_j^z \sigma_{j+1}^z - h_1 \sum_{j=-\infty}^{-1} \sigma_j^x - h_2 \sum_{j=0}^{\infty} \sigma_j^x - J_1 \left(\prod_{k=-\infty}^{\infty} \sigma_k^x\right) \sigma_{-1}^z \sigma_0^z. \tag{3.22}$$

The JW string attached to σ_{-1}^z is no longer cancelled by that attached to σ_0^z, and thus the coupling between the two chains picks up a nonlocal factor of a global spin flip about the $\hat{x}$ axis, the symmetry operator $\mathcal{F}$. This factor drives a significant difference in physics between the spin and fermionic SZMs, as we have seen.

3.8 Exact Solution for the spin boundary SZM

In this Appendix, we shall prove the existence of an exact SZM starting at the boundary spin σ_0^z between two transverse field Ising chains with different couplings. In particular we focus on the same Hamiltonian as we considered earlier but with the left-hand chain a finite N sites long:

$$H_{\mathrm{BI}} = -J_1 \sum_{j=-N}^{-1} \sigma_j^z \sigma_{j+1}^z - J_2 \sum_{j=0}^{\infty} \sigma_j^z \sigma_{j+1}^z - h_1 \sum_{j=-\infty}^{-1} \sigma_j^x - h_2 \sum_{j=0}^{\infty} \sigma_j^x. \tag{3.23}$$

We will solve the case $N = 1$ exactly, and provide evidence that as $N \to \infty$ the SZM converges.

We will often consider the same Hamiltonian written in terms of a_i, b_i, the usual Majorana fermion operators defined with a Jordan–Wigner string starting from the left edge of the chain, see Eq. 3.12:

$$H_{\mathrm{FBI}} = -iJ_1 \sum_{j=-N}^{-1} b_j a_{j+1} - iJ_2 \sum_{j=0}^{\infty} b_j a_{j+1} - ih_1 \sum_{j=-\infty}^{-1} a_j b_j - ih_2 \sum_{j=0}^{\infty} a_j b_j. \tag{3.24}$$

3.8.1 Ansatz

We will use the following ansatz for the SZM:

$$\Psi_N = i^N \mathcal{N} \sum_{\substack{i_0 < \cdots < i_N \\ j_0 < \cdots < j_{N-1}}} A_{i_0 \ldots i_N} B_{j_0 \ldots j_{N-1}} a_{i_0} b_{j_0} a_{i_1} b_{j_1} \ldots a_{i_N}, \tag{3.25}$$

for real scalar coefficients A, B and normalization $\mathcal{N}$. Additionally, to ensure the normalization $\mathcal{N}$ measures the overlap with the boundary spin $\sigma_0^z = i^N (\prod_{j=-N}^{-1} a_j b_j) a_0$, we fix the coefficent of this term in the sum to one: $A_{-N,-N+1,\ldots,0} = B_{-N,-N+1,\ldots,-1} = 1$.

The use of this ansatz enforces two major assumptions: firstly, every term in the SZM expansion has the same number of a and b Majorana fermion operators; secondly, the magnitude of each term in the expansion can be factorized into two contributions which only depend on which a or b operators are present independently. As observed earlier, the *total* number of Majorana operators remaining constant in each term of Ψ_N immediately follows from the quadratic, free-fermion nature of H_{BI}. The further separate conservation of a and b operator number is natural if we insist that, as well as commuting with the Hamiltonian, the SZM must be related to the boundary spin by a unitary transform: $\Psi_N = U^\dagger \sigma_0^z U$. This ensures that the SZM squares to the identity, $\Psi_N^2 = 1$. It is also consistent with the understanding that the SZM is a consequence of the emergent U(1) symmetry revealed by a local unitary transformation of the Hamiltonian to a new Hamiltonian under which the boundary spin is conserved exactly[14].

In order to explain the separate conservation of a and b operator number, let us first assume the converse, so that Ψ_N consists of the sums of arbitrary strings of a and b operators

total length $2N+1$. Let the number of a operators in a given string s be $N_a(s)$, and let the commutator $C = [H_{\mathrm{BI}}, \Psi_N]$. For Ψ_N to commute with the Hamiltonian every term in C must individually vanish. Notice that one commutation with H_{BI} changes the number of a operators in a string by ± 1; thus, each operator string s with $N_a(s) = n$ in C originated from an operator string s' with $N_a(s') = n \pm 1$ in Ψ_N. This means that enforcing commutation with the Hamiltonian only relates the coefficients of operator strings in Ψ_N with the same parity of $N_a(s)$. We can thus neglect any operator string in Ψ_N with opposite N_a-parity to the zeroth order term σ_0^z.

Having established this condition on operator strings in Ψ_N, let us turn to the form of the unitary transform U. Without loss of generality, we may write as $U = e^G$ for anti-Hermitian G. Every possible operator string with the same total Majorana fermion operator number as σ_0^z can be generated by a unitary transform defined by

$$G = \sum_{i,j=-N}^{\infty} \left(\alpha_{ij} a_i a_j + \beta_{ij} b_i b_j + \gamma_{ij} a_i b_j\right), \tag{3.26}$$

for arbitrary constants α_{ij}, β_{ij} and γ_{ij}. However, the $a_i b_j$ terms in G will result in operator strings in Ψ_N of arbitrary N_a-parity; thus, from the discussion above, we must set $\gamma_{ij} = 0$. Possible additional terms in G greater than quadratic in Majorana fermion operators, which could feasibly conserve N_a-parity by changing $N_a(\sigma_0^z)$ by an even number, such as $a_i a_j b_k b_l$, will generically not conserve total Majorana fermion operator number. The remaining terms in G conserve the number of a and b operators exactly. Furthermore, notice that if $\gamma_{ij} = 0$, U splits into two mutually commuting parts: $U = U_a U_b = e^{G_a} e^{G_b}$, where $G_a = \sum \alpha_{ij} a_i a_j$ and $G_b = \sum \beta_{ij} b_i b_j$. This justifies the factorization of the magnitude of each term in our ansatz for Ψ_N into two contributions A and B which only depend on which a or b operators are present respectively.

3.8.2 Counting terms involving a fixed number of hops

Having defined the ansatz, we now wish to consider how many terms there are of a given order when we send N to infinity. The order in perturbation theory each term in this ansatz appears is given by the minimum number of 'hops' each Majorana fermion operator a_i and b_j must make on their respective sublattices to reach that term from their initial positions at zeroth order, Sa_0, where S is the product of all a_is and b_is for $i < 0$. For example, in the ferromagnetic regime of both chains, a fermion-operator product that can be reached from Sa_0 in no fewer than n hops will appear at leading order $\propto (\prod_{\mathrm{j}} h(j)J(j))/(J_1^2 - J_2^2)^n$, where $h(j)$ and $J(j)$ are the h and J associated with hop j of n. One can calculate the coefficients using the appropriate G, which we find to be

$$\begin{aligned} G \approx \sum_{n=0}^{\infty} \frac{1}{2(J_1^2 - J_2^2)^n} \sum_{m=0}^{n-1} (-1)^{m+1} \binom{n-1}{m} \big((J_1 h_1)^m (J_2 h_2)^{n-m} a_{-m} a_{n-m} + \\ (h_2/h_1)(J_1 h_1)^{n-m} (J_2 h_2)^m b_{m-n} b_m\big) \end{aligned} \tag{3.27}$$

to term-wise leading order in $(J_1^2 - J_2^2)^{-1}$.

In particular, we can map terms of order n with m 'a' hops and $n-m$ 'b' hops to simultaneous partitions of the integers m and $n-m$. To see this, note that any given 'a' or 'b' can't have made any more hops than a fermion of the same type to its right; therefore, we can associate any partition with a collection of hops of one type of fermion uniquely, assigning the largest integer to the rightmost fermion of that flavor, the second largest integer to the fermion immediately to its left, and so on. The number of partitions $p(n)$ of an integer n is well known to be bounded by $(1/4\sqrt{3}n)\exp\left(\pi\sqrt{2n/3}\right)$. We can then bound the number of n hop terms $q(n)$ for even $n \geq 8$ by

$$q(n) = \sum_{m=0}^{n} p(m)p(n-m) < np\left(\frac{n}{2}\right)^2 < \frac{1}{12n}\exp\left(\pi\sqrt{\frac{4n}{3}}\right) \tag{3.28}$$

which is subexponential in n. This inequality in fact also holds for odd $n \geq 9$ if we replace $p(n/2)^2$ in the middle expression with $p((n-1)/2)p((n+1)/2)$. If the coefficients of the terms themselves are also at most exponential in n, the norm of the operator formed by just keeping the leading order coefficients of terms in the SZM can be bounded by a geometric series, and will therefore be finite within some radius of convergence. We have not set such a tight enough bound for the coefficients, but from our programmatic calculation up to 10th order in perturbation theory, we believe this to be the case.

3.8.3 Single boundary spin

We turn to dealing exactly with the case $N = 1$, that is, when there is a single spin on the edge. In this case, our ansatz becomes

$$\Psi_3 = i\mathcal{N}\sum_{l=-1}^{\infty}\sum_{j=-1}^{\infty}\sum_{k=j+1}^{\infty} A_{j,k}B_l a_j a_k b_l, \tag{3.29}$$

where we set $A_{-1,0} = B_{-1} = 1$.

We want to find the appropriate $A_{j,k}, B_l$ such that each term in the commutator $C = [H_{\mathrm{BI}}, \Psi_3]$ vanishes. Given the form of the ansatz and the Hamiltonian, operator strings in C necessarily have the form $a_m b_n b_p$ or $a_m a_n a_p$. In order to visualize the contributions to each term in C, it is helpful to represent operator strings as diagrams as in Fig. 3.7. Splitting each lattice site in two, the presence of Majorana fermion operators a and b on a lattice site in a string are represented by filled circles on the upper or lower chain respectively. The action of commuting the string by H_{BI} amounts to 'hopping' filled circles in this diagram to neighboring sites, with a hard-core constraint.

In particular, the diagram in Fig. 3.7 shows the contributions to the operator strings in C of the form $a_{-1}b_{-1}b_m$ for $m \geq 0$. Here two of the Majorana operators remain in their original positions in σ_0^z and one moves away. Demanding these terms vanish thus leads to

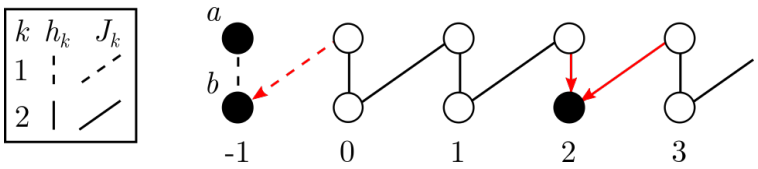

Figure 3.7: The links of the chain depict the Hamiltonian couplings, while the filled circles denote an operator string, in this case $a_{-1}b_{-1}b_2$. The red arrows show how this string may be obtained from strings in Ψ_3 by the commutation $[H, \Psi_3]$.

the conditions:

$$\begin{aligned} J_2 A_{-1,m+1} - h_2 A_{-1,m} - J_1 B_m &= 0 \\ A_{-1,m+1} = \frac{h_2}{J_2} A_{-1,m} - \frac{J_1}{J_2} B_m &\qquad m \geq 0 \end{aligned} \tag{3.30}$$

Recursively substituting the left hand side of equation (3.30) into the right hand side, we may eliminate the $A_{1,j}$ entirely from the right hand side to find:

$$A_{-1,m+1} = \sum_{j=0}^{m} \frac{h_2^{m-j}}{J_2^{m-j+1}} J_1 B_j + \left(\frac{h_2}{J_2}\right)^{m+1} \qquad m \geq 0, \tag{3.31}$$

where we have used $A_{-1,0} = 1$. We find $A_{0,m}$ from similar constraints on strings in C of the form $a_0 b_{-1} b_m$:

$$J_2 A_{0,m+1} - h_2 A_{0,m} - h_1 B_m = 0 \qquad m \geq 1$$
$$J_2 A_{0,1} - h_1 B_0 = 0 \tag{3.32}$$
$$\implies A_{0,m+1} = \sum_{j=0}^{m} \frac{h_2^{m-j}}{J_2^{m-j+1}} h_1 B_j \qquad m \geq 0. \tag{3.33}$$

Continuing to focus on strings in C with only one Majorana fermion operator different from σ_0^z, let us consider those of form $a_{-1}a_0a_m$ for $m > 0$ (Fig 3.8). These impose the conditions:

$$J_2 B_{m-1} - h_2 B_m - h_1 A_{0,m} - J_1 A_{-1,m} + h_2 B_0 A_{-1,m} = 0 \qquad m \geq 1$$

Rewriting $A_{0,m}$ and $A_{1,m}$ using equations (3.31) and (3.33) we find:

$$h_2 B_m = J_2 B_{m-1} + \sum_{j=0}^{m-1} \left[(h_2 B_0 - J_1) \frac{h_2^{m-j-1}}{J_2^{m-j}} J_1 - \frac{h_2^{m-j-1}}{J_2^{m-j}} h_1^2 \right] B_j + (h_2 B_0 - J_1) \left(\frac{h_2}{J_2}\right)^m . \tag{3.34}$$

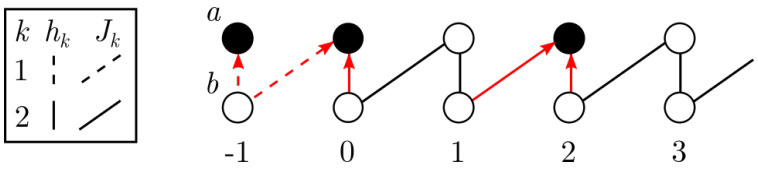

Figure 3.8: As in Fig. 1, the filled circles denote an operator string, in this case $a_{-1}a_{-0}a_2$. The red arrows show how this string may be obtained from strings in Ψ_3 by the commutation $[H, \Psi_3]$.

This is a recurrence relation for B_m in terms of B_j with $j < m$, suggesting we may be able to solve for arbitrary B_m in terms of some initial set. Considerable simplification is possible if we first extract the last, $(m-1)$-th term from the sum on the right hand side:

$$h_2 B_m = \frac{1}{J_2}(J_2^2 + h_2 B_0 J_1 - h_1^2) B_{m-1} + \frac{h_2}{J_2}\left(\sum_{j=0}^{m-2}\left[(h_2 B_0 - J_1)\frac{h_2^{m-j-2}}{J_2^{m-j-1}}J_1 - \frac{h_2^{m-j-2}}{J_2^{m-j-1}}h_1^2\right]B_j + (h_2 B_0 - J_1)\left(\frac{h_2}{J_2}\right)^{m-1}\right)$$

We can now replace the term in the large brackets using equation (3.34) but with $m \to (m-1)$:

$$\begin{aligned} h_2 B_m &= \frac{1}{J_2}(J_2^2 + h_2 B_0 J_1 - h_1^2) B_{m-1} + \frac{h_2}{J_2}(h_2 B_{m-1} - J_2 B_{m-2}) \\ B_m &= \alpha B_{m-1} - B_{m-2}, \end{aligned} \tag{3.35}$$

for $\alpha = \frac{1}{h_2 J_2}(J_2^2 - J_1^2 + h_2^2 - h_1^2 + h_2 J_1 B_0)$. Equation (3.35) is a recurrence relation with constant coefficents and two unknown initial conditions, B_0 and B_1. However, B_1 can be directly calculated in terms of B_0 from equation (3.34) with $m = 1$ as $B_1 = \alpha B_0 - J_1/J_2$. Thus, using basic combinatorics, we can now immediately solve for arbitrary B_m in terms of B_0.

The most illuminating form of the solution for our purposes will be the generating function for the B_m, which is simply

$$G(x) = \sum_{j=0}^{\infty} B_j x^j = \frac{B_0 - (J_1/J_2)x}{1 - \alpha x + x^2}. \tag{3.36}$$

Notice that the polynomial on the denominator is palindromic: it is self-reciprocal. Thus its roots can be written as λ and λ^{-1}. Let us assume for the moment that both roots are real, and choose $\lambda \geq 1$, so that $\lambda^{-1} \leq 1$. Factoring the denominator as $(1-\lambda x)(1-\lambda^{-1}x)$ and expanding $G(x)$ as partial fractions, we find:

$$\begin{aligned} G(x) &= \frac{c_1}{1-\lambda x} + \frac{c_2}{1-\lambda^{-1}x} \\ &= c_1(1 + \lambda x + \lambda^2 x^2 + \dots) + c_2(1 + \lambda^{-1}x + \lambda^{-2}x^2 + \dots), \end{aligned}$$

for constants c_1, c_2. Because $\lambda > 1$, $G(x)$ diverges, which means that B_m becomes larger and larger with m, and the SZM is delocalized. In order to avoid this fate, we must choose B_0 such that the numerator polynomial in equation (3.36) *cancels* the factor of $(1 - \lambda x)$ in the denominator:

$$\frac{B_0 - (J_1/J_2)x}{(1 - \lambda x)} = B_0 \qquad \forall x, \tag{3.37}$$

where the constant on the right hand side must be B_0 for $G(0) = B_0$. Notice also λ depends on B_0 through α. Thus finally

$$\begin{aligned} B_0 &= \frac{J_1}{J_2}\lambda^{-1} \\ &= \frac{J_1}{h_2}\frac{\Delta_{h^2} + \Delta_{J^2} \pm \sqrt{\left((h_1 - h_2)^2 + \Delta_{J^2}\right)\left((h_1 + h_2)^2 + \Delta_{J^2}\right)}}{2\Delta_{J^2}} \end{aligned} \tag{3.38}$$

where we have defined $\Delta_{h^2} = h_1^2 - h_2^2$ and $\Delta_{J^2} = J_1^2 - J_2^2$. If $\Delta_{h^2} + \Delta_{J^2} > 0$ we take the negative branch of the solution, and vice versa, in order to minimize λ^{-1} and ensure convergence if possible.

On substituting (3.37) into (3.36), we obtain the standard geometric series generating function, immediately implying

$$B_m = \left(\frac{J_2}{J_1}\right)^m B_0^{m+1} \tag{3.39}$$

As an interesting aside, although we have not made any assumptions in the derivation above as to the phase of the underlying transverse-field Ising chains, we remark here that if we do assume both chains are in the ferromagnetic phase and Taylor expand B_0 around $h_1 = 0$ and $h_2 = 0$, we find that the $h_1^{2n} h_2^{2k+1}$ term has numerical coefficient equal to $N(n, k)$, the number on the n-th row and k-th column of the Narayana triangle, for $n, k \geq 1$. In fact, B_0 is equivalent to the generating function for the Narayana numbers under the substitution $t = h_2^2/h_1^2$ and $z = -h_1^2/\Delta_{J^2}$. [97]. One way of understanding this combinatorially is the following: in the perturbative construction of the SZM, after acting once with h_2 to obtain the lowest order possible operator string with b_0 present, the number of ways to act $2n$ times with the h_1 part of the Hamiltonian and $2k$ times with the h_2 part of the Hamiltonian and return to an operator string with b_0 present is exactly equal to number Dyck words of n pairs of matching brackets [and] with k nestings.

Let us now return to solving for the SZM by calculating the $A_{n,m}$. Substituting B_m from equation (3.39) into equations (3.31) and (3.33) yields solutions for $A_{-1,m}$ and $A_{0,m}$ as the results of partial geometric sums. To calculate $A_{n,m}$ for $n > 0$, we will need to appeal to further conditions on the vanishing commutator $C = 0$. In particular, consider strings in C

of the form $a_n b_{n-1} b_m$ for $n > 0$:

$$\begin{aligned} &J_2 A_{n,m+1} B_{n-1} - h_2 A_{n,m} B_{n-1} - h_2 A_{n-1,n} B_m = 0 \qquad m \geq n+1 \\ &J_2 A_{n,n+1} B_{n-1} - h_2 A_{n-1,n} B_n = 0 \qquad n > 0 \end{aligned} \tag{3.40}$$

$$\implies A_{n,m+1} = \frac{A_{n-1,n}}{B_{n-1}} \sum_{j=n}^{m} B_j \left(\frac{h_2}{J_2}\right)^{m-j+1} \qquad n > 0,\, m > n. \tag{3.41}$$

Substituting $B_n/B_{n-1} = (J_2/J_1)B_0$ and $A_{0,1} = (h_1/J_2)B_0$ from equation (3.32) into equation (3.40) trivially leads to $A_{n-1,n} = \frac{h_1}{J_2}\left(\frac{h_2}{J_1}\right)^{n-1} B_0^n$ for $n > 0$. This allows us to evaluate the sum (3.41) as another geometric series. Finally, we obtain the following solution for all $A_{n,m}$:

$$A_{n,m} = \begin{cases} \gamma\left[(h_2 J_1 + B_0 \Delta_{J^2})\left(\frac{h_2}{J_2}\right)^m - B_0 J_1^2 \left(\frac{B_0 J_2}{J_1}\right)^m\right], & n = -1 \\ \gamma \frac{h_1 B_0}{J_2}\left(\frac{h_2 B_0}{J_1}\right)^n \left[h_2 J_1 \left(\frac{h_2}{J_2}\right)^{m-n-1} - B_0 J_2^2 \left(\frac{B_0 J_2}{J_1}\right)^{m-n-1}\right], & n > -1 \end{cases} \tag{3.42}$$

where we have defined $\gamma = (h_2 J_1 - B_0 J_2^2)^{-1}$.

Now that we have a complete solution for B_n and $A_{n,m}$, several remarks are in order. Firstly, while we have used the fact that specific terms in the commutator with the Hamiltonian C vanish to fully specify the $A_{n,m}$ and B_m, one should, and can, check that for solutions of the above form, all terms in C vanish. Secondly, for the SZM we require localization, such that the $A_{n,m}$ and B_m are exponentially decreasing functions of n and m. This is manifestly satisfied if the magnitudes of the ratios $\frac{h_2}{J_2}$ and $\frac{J_2 B_0}{J_1}$ are less than one. Of course, we also require that B_0 be real so that the SZM is Hermitian.

The final calculation and condition on the exact strong zero mode is that the normalization $\mathcal{N}$ must converge. For an ansatz of the form (3.29), the normalization is given by

$$\mathcal{N}^{-2} = \left(\sum_{l=-1}^{\infty} B_l^2\right)\left(\sum_{j=-1}^{\infty}\sum_{k=j+1}^{\infty} A_{j,k}^2\right) \tag{3.43}$$

Using the explicit forms of B_m and $A_{j,k}$, this sum can be easily computed as the sum of several geometric series, yielding:

$$\begin{aligned} \mathcal{N}^{-2} =& ((h_2^2 - J_2^2)(J_1 - B_0 h_2)^2 \left(B_0^2 J_2^2 - J_1^2\right))^{-1} (B_0 J_1^4 \left(B_0 \left(h_1^2 - 2h_2^2 + J_1^2\right) + 2h_2 J_1 - B_0^3 h_2^2\right) \\ &+ J_1^2 J_2^2 (J_1 - B_0 h_2)\left(J_1 - \left(2B_0^3 + B_0\right) h_2\right) - B_0^2 J_2^4 (J_1 - B_0 h_2)^2) \end{aligned} \tag{3.44}$$

The normalization converges under the same conditions for the A_j, k and B_m remain localized. In particular, solving for the roots of the denominator which give the limit of

convergence, we find:

$$h_2 = J_2,$$
$$J_1 = \pm\sqrt{J_2 \frac{h_1^2 - (h_2 - J_2)^2}{h_2 - J_2}},$$
$$J_1 = \pm\sqrt{J_2 \frac{-h_1^2 + (h_2 + J_2)^2}{h_2 + J_2}}.$$

For example, for $h_1 = h_2 = 0.1$ and $J_2 = 1$, the normalization converges for $J_1 < 0.9428\ldots$ and $J_1 > 1.0444\ldots$, in agreement with the numerics in Figure 3.5.

3.9 Operator perturbation theory

3.9.1 Background and proof of SZM construction

Earlier we gave the intuition that resonances occur when there is an energy conserving process to flip the degree of freedom associated with the 0^{th} order term of the almost SZM using terms from the perturbative part of the Hamiltonian. However, there were other resonances we could imagine existing based on this reasoning that we don't actually observe. In the boundary Ising model, for instance, if in addition to flipping spin -1 with $-J_1\sigma^z_{-1}\sigma^z_0$ and spin 0 with $-h_2\sigma^x_0$ we also flipped spins -3 and -2 with $-J_1\sigma^z_{-3}\sigma^z_{-2}$, we could have an energy conserving process at $h_1 = J_2/3$ coming in at third order, but no such term exists.

Here we lay out another way to construct almost SZMs (or SZMs) that is helpful for gaining insight into why certain poles appear or do not appear in a given mode. This construction uses an operator perturbation theory; the intuition is that because the (almost) SZM (approximately) does not evolve in time, we should be able to write it as a linear combination of operators that are stationary under evolution by the Liouvillian (i.e. the commutator with the Hamiltonian). When we perturb the Hamiltonian, and thus the Liouvillian and its stationary operators, the corresponding linear combination of perturbed operators should still be approximately stationary. We can think of this in analogy to ordinary perturbation theory on a system's eigenstates. Here instead we're concerned with eigen*operators* of the Louivillian, which is a linear superoperator (i.e. a map from operator space to itself).

We will utilize the operator perturbation theory derived in Ref. [102] to construct SZMs. First we will restate the relevant definitions. We consider perturbing a Hamiltonian $H_0 \to H_0 + \lambda H_1$, where we know how to diagonalize H_0,

$$H_0|n^{(0)}\rangle = E_n^{(0)}|n^{(0)}\rangle. \tag{3.45}$$

We will also define the Liouville superoperators

$$L_0 = [H_0, \cdot] \tag{3.46}$$
$$L_1 = [H_1, \cdot] \tag{3.47}$$
$$L = [H, \cdot]. \tag{3.48}$$

Analogously to applying perturbation theory to wavefunctions, Ref. [102] describes how operators change in the Heisenberg picture under the effect of the perturbation. To do this, we need some set of unperturbed basis operators $\{R_n^{(0)}\}$ that are eigenoperators of L_0:

$$L_0 R_n^{(0)} = \omega_n^{(0)} R_n^{(0)} \tag{3.49}$$

such that

$$L_0 \omega_n^{(0)} = 0, \tag{3.50}$$

where generically the eigenvalues $\{\omega_n^{(0)}\}$ are themselves allowed to be operators. In particular, one choice that will work for any H_0 is $\{R_{ij}^{(0)}\}$, with

$$R_{ij}^{(0)} = |i^{(0)}\rangle\langle j^{(0)}| \tag{3.51}$$

and

$$\omega_{ij}^{(0)} = E_i^{(0)} - E_j^{(0)}, \tag{3.52}$$

as can be readily verified using Eq. (3.49).

Finally, we define perturbed versions of the eigenoperators and eigenvalues, and demand that they obey analogous conditions to Eqs. (3.49) and (3.50):

$$S_n = \sum_m \lambda^n R_n^{(m)} \tag{3.53}$$
$$\Omega_n = \sum_m \lambda^n \omega_n^{(m)} \tag{3.54}$$

such that

$$LS_n = \Omega_n S_n \tag{3.55}$$
$$L\Omega_n = 0. \tag{3.56}$$

With these definitions out of the way, we will decompose the unperturbed SZM into the $\{R_{ij}^{(0)}\}$ basis,

$$\Psi^{(0)} = \sum_{i,j} c_{ij} R_{ij}^{(0)} \tag{3.57}$$

and prove that by replacing each $R_{ij}^{(0)}$ with S_{ij} we get the SZM in the perturbed system (or an almost SZM, truncating appropriately):

$$\Psi = \sum_{i,j} c_{ij} S_{ij}. \tag{3.58}$$

as long as the perturbation does not break the symmetry associated with the SZM.
Proof. Let $\psi = \sum_{i,j} c_{ij} S_{ij}$. Then acting with L we have

$$L\psi = \sum_{i,j} c_{ij} L S_{ij} = \sum_{i,j} c_{ij} \Omega_{ij} S_{ij}. \tag{3.59}$$

Now, since

$$\begin{aligned} \Psi^{(0)} &= \sum_{ij} |i^{(0)}\rangle\langle i^{(0)}|\Psi^{(0)}|j^{(0)}\rangle\langle j^{(0)}| \\ &= \sum_{ij} \langle i^{(0)}|\Psi^{(0)}|j^{(0)}\rangle R_{ij}^{(0)}, \end{aligned} \tag{3.60}$$

we have that $c_{ij} = \langle i^{(0)}|\Psi^{(0)}|j^{(0)}\rangle$. Furthermore, we know that, up to corrections exponentially suppressed in L, $\Psi^{(0)}$ takes each eigenstate of H_0 to a state in another sector of the associated symmetry [87]. These pairs (or, generally, groups of m states for SZMs with $\Psi^m = 1$) will also be degenerate up to exponentially small corrections in L, and if the pertubation doesn't break the SZM's symmetry that degeneracy will be preserved.

Then since for this basis $\omega_{ij}^{(n)} = E_i^{(n)} - E_j^{(n)}$[102], we have $\Omega_{ij} = E_i - E_j$. So for any i, j, either c_{ij} or Ω_{ij} is exponentially small in L. Thus $\|L\psi\| = \left\|\sum_{i,j} c_{ij}\Omega_{ij}S_{ij}\right\| < e^{-\alpha L}$ for some constant α, and ψ is an SZM. □

3.9.2 Operators SZM construction for the boundary Ising model

Now we will apply operator perturbation theory to reconstruct the almost SZM for the boundary Ising model to second order. In doing so, we will be a little more general and not specify H_0 other than requiring that it has an unperturbed SZM $\Psi^{(0)} = \sigma_0^z$ and the eigenstates we will specify below. We will, however, specify V:

$$V_{\mathrm{BI}} = -J_1 \sum_{j=-\infty}^{-1} \sigma_j^z \sigma_{j+1}^z - h_2 \sum_{j=0}^{\infty} \sigma_j^x. \tag{3.61}$$

We will also work in the basis of states

$$\left\{ \left(\bigotimes_{\alpha=-\infty}^{-1} |\leftrightarrow_\alpha\rangle \right) \otimes \left(\bigotimes_{\beta=0}^{\infty} |\updownarrow_\beta\rangle \right) \right\} \tag{3.62}$$

where $|\leftrightarrow_\alpha\rangle$ is an eigenstate of σ_α^x and $|\updownarrow_\beta\rangle$ is an eigenstate of σ_β^z. In particular, these are eigenstates for $H_{\mathrm{BI}}[J_1 = h_2 = 0]$. Finally, for simplicity we will adopt some notation. First, in the expressions that follow we will drop (0) superscripts for the unperturbed states and energies. Indices i and j will refer to elements of the basis Eq. (3.62), whereas α and β will refer to sites. A prime on a Greek letter or a number, e.g. α', will refer to flipping that spin,

and a double prime refers to flipping a spin as well as the spin to the right (so β'' refers to flipping spins β and $\beta+1$).

For the R_{ij} basis we're using, corrections to a basis operator can be written in terms of the perturbative corrections to the eigen*states*[102]:

$$R_{ij}^{(n)} = \sum_{m=0}^{n} |i^{(m)}\rangle\langle j^{(n-m)}|. \tag{3.63}$$

We then note that since $\Psi^{(0)} = \sigma_0^z$ is diagonal in this basis, we only need corrections to R_{ii}:

$$\Psi^{(0)} = \sum_{ij}\langle i|\sigma_0^z|j\rangle R_{ij}^{(0)} = \sum_{i}\langle i|\sigma_0^z|i\rangle R_{ii}^{(0)}, \tag{3.64}$$

and therefore

$$\Psi^{(n)} = \sum_{i}\langle i|\sigma_0^z|i\rangle R_{ii}^{(n)}. \tag{3.65}$$

The first and second order corrections are

$$R_{ii}^{(1)} = -h_2\sum_{\alpha\geq 0}\frac{|i;\alpha'\rangle\langle i| + \text{h.c.}}{E_i - E_i^{\alpha'}} - J_1\sum_{\alpha<-1}\frac{|i;\alpha''\rangle\langle i| + \text{h.c.}}{E_i - E_i^{\alpha''}} - J_1\,\langle i|\,\sigma_0^z\,|i\rangle\,\frac{|i;-1'\rangle\langle i| + \text{h.c.}}{E_i - E_i^{-1'}} \tag{3.66}$$

and

$$\begin{aligned}
R_{ii}^{(2)} = {} & h_2^2\Bigg(\sum_{\substack{\alpha,\beta\geq 0\\ \alpha\neq\beta}}\frac{|i;\alpha'\beta'\rangle\langle i| + \text{h.c.}}{(E_i - E_i^{\alpha'})(E_i - E_i^{\alpha'\beta'})} - \sum_{\alpha\geq 0}\frac{|i\rangle\langle i|}{(E_i - E_i^{\alpha'})^2} + \sum_{\alpha,\beta\geq 0}\frac{|i;\alpha'\rangle\langle i;\beta'|}{(E_i - E_i^{\alpha'})(E_i - E_i^{\beta'})}\Bigg)\\
& + J_1^2\Bigg(\sum_{\substack{\alpha,\beta<-1\\ \alpha\neq\beta}}\frac{|i;\alpha''\beta''\rangle\langle i| + \text{h.c.}}{(E_i - E_i^{\alpha''})(E_i - E_i^{\alpha''\beta''})} - \sum_{\alpha<-1}\frac{|i\rangle\langle i|}{(E_i - E_i^{\alpha''})^2} + \sum_{\alpha,\beta<-1}\frac{|i;\alpha''\rangle\langle i;\beta''|}{(E_i - E_i^{\alpha''})(E_i - E_i^{\beta''})}\Bigg)\\
& + J_1h_2\sum_{\substack{\alpha\geq 0\\ \beta<-1}}\left(\frac{(2E_i - E_i^{\alpha'} - E_i^{\beta''})\,|i;\alpha'\beta''\rangle\langle i| + \text{h.c.}}{(E_i - E_i^{\alpha'})(E_i - E_i^{\beta''})(E_i - E_i^{\alpha'\beta''})} + \frac{|i;\alpha'\rangle\langle i;\beta''| + \text{h.c.}}{(E_i - E_i^{\alpha'})(E_i - E_i^{\beta''})}\right)\\
& + J_1h_2\sum_{\alpha\geq 0}\Bigg(\left(\frac{\langle i|\,\sigma_0^z\,|i\rangle}{(E_i - E_i^{-1'})(E_i - E_i^{-1'\alpha'})} + \frac{\langle i;\alpha'|\,\sigma_0^z\,|i;\alpha'\rangle}{(E_i - E_i^{\alpha'})(E_i - E_i^{-1'\alpha'})}\right)(|i;-1'\alpha'\rangle\langle i| + \text{h.c.})\\
& + \frac{\langle i|\,\sigma_0^z\,|i\rangle\,(|i;\alpha'\rangle\langle i;-1'| + \text{h.c.})}{(E_i - E_i^{\alpha'})(E_i - E_i^{-1'})}\Bigg)\\
& + J_1^2\sum_{\alpha<-1}\Bigg(\left(\frac{(2E_i - E_i^{-1'} - E_i^{\alpha''})\,\langle i|\,\sigma_0^z\,|i\rangle}{(E_i - E_i^{-1'})(E_i - E_i^{\alpha''})(E_i - E_i^{-1'\alpha''})}\right)(|i;-1'\alpha''\rangle\langle i| + \text{h.c.})\\
& + \frac{\langle i|\,\sigma_0^z\,|i\rangle\,(|i;\alpha''\rangle\langle i;-1'| + \text{h.c.})}{(E_i - E_i^{\alpha''})(E_i - E_i^{-1'})}\Bigg) + \frac{J_1^2}{(E_i - E_i^{-1'})^2}(|i;-1'\rangle\langle i;-1'| - |i\rangle\langle i|).
\end{aligned} \tag{3.67}$$

When we plug the $R^{(1)}_{ii}$s into Eq. (3.65) to get $\Psi^{(1)}$, we find that all of the terms cancel except for those with $\alpha = 0$. This makes sense; this just means that the perturbation needs to flip the edge spin (which was conserved when σ^z_0 was the SZM) to modify the SZM. Flipping spin zero has an energy cost of $\pm 2J_2$ in the boundary Ising model, so there are no poles at first order.

For $\Psi^{(2)}$, all terms not involving a flip of spin 0 will cancel. Furthermore, almost all terms will also cancel given the energy of both excitations together above the unperturbed state is simply the sum of each separately; specifically, they will cancel if

$$E^{ab}_i - E_i = (E^a_i - E_i) + (E^b_i - E_i) \tag{3.68}$$

where a and b denote an excitation (i.e. either flipping one spin on the ferromagnetic side or two adjacent spins on the paramagnetic side). Here, of course, one of those excitations will be flipping spin 0. For the boundary Ising model, all pairs of excitations except for adjacent spins flips in the ferromagnetic phase and overlapping pairs of spin flips in the paramagnetic phase obey Eq. (3.68), and therefore will not contribute poles where this condition applies. If we were to flip a sequence of adjacent spins in the ferromagnet starting from spin 0, however, any domain wall created/destroyed by flipping spin i will be destroyed/created by flipping spin $i+1$, and we can only create or destroy one domain wall on net, changing the energy by $\pm 2J_2$. Similarly, suppose only spin i is flipped in the paramagnetic phase (the first paramagnetic spin we flip must be spin -1 with the boundary term $-J_1\sigma^z_{-1}\sigma^z_0$, as described below). Then we could flip spin i and $i-1$, evading Eq. (3.68), but now only spin $i-1$ is flipped (i having been flipped and flipped back). Just as with the domain walls, we can only flip one paramagnetic spin on net. If we were to add some terms to H_0 (that didn't change our assumed eigenstates) to make additional pairs of excitations that broke the separability condition (3.68) (for example, next nearest neighbor ZZ interactions) we would get additional poles at $E_i = E^{ab}_i$.

As we implied above, there is an exception to this condition enforcing that terms cancel. Specifically, it does not apply when one of the excitations involves the boundary term $-J_1\sigma^z_{-1}\sigma^z_0$, since that term measures the sign of the boundary spin σ^z_0, which flips during any processes which contribute to the perturbation theory. Instead, the cancellation condition becomes

$$E^{ab}_i - E_i = (E^a_i - E_i) - (E^b_i - E_i), \tag{3.69}$$

such that the excitations now *subtract* independently to give the total energy above the unperturbed state. In general, this means such terms will not cancel.

For the boundary Ising model, then, we can create one spin flip in the paramagnetic phase and one domain wall in the ferromagnetic phase using $-J_1\sigma^z_{-1}\sigma^z_0$ and $-h_2\sigma^x_0$ and then move those excitations further into their respective phases, but we can only change the system's energy by $\pm 2h_1 \pm 2J_2$ on net after creating a spin flip/domain wall pair and moving either/both, explaining the lack of additional poles in Ψ. We could make additional excitations at the boundary after making room by moving away any previous excitations,

but after forming m excitations the total change in energy will just be $\pm 2mh_1 \pm 2mJ_2$, again generating no new resonances.

We have demonstrated the conditions under which a SZM has a resonance in boundary Ising-like models up to second order in perturbation theory. The key intuition we developed is that a resonance requires not only states of equal energy with the spin of interest flipped, but also a process connecting those two states driven by a sequence of excitations, whose energies depend on each others' presence and the spin of interest. We expect this criterion to be of general importance to SZMs in free and integrable spin chains.

Chapter 4

Characterization of scrambling in the Sachdev–Ye–Kitaev model

4.1 Introduction

In 2015, a paper [1] by Maldacena, Shenker, and Stanford provided a universal upper bound (under a few assumptions) for the rate at which a system can be "scrambled," a strong form of thermalization; when a system is scrambled, we cannot reconstruct information about the initial state without making a number of measurements on the order of the total number of degrees of freedom [103]. The method Maldacena *et al* used to find the scrambling time is based on the characteristic timescale it takes for a certain four operator thermal expectation value $F(t)$ to decay to zero. At the shorter dissipation time t_d, characterizing the decay of two operator correlators, $F(t)$ approaches some nonzero constant value F_d, where it will approximately remain until the system's scrambling time t_*. $F(t)$ is a so-called "out of time order correlator" (OTOC), and measures the effect of a perturbation of one operator on another at a different time [104]. They show that $F_d - F(t)$ will grow exponentially as $\varepsilon e^{\lambda_L t}$ with a Lyapunov exponent $\lambda_L \leq 2\pi k_B T/\hbar$; in that sense, scrambling constitutes quantum chaos. This bound is saturated by black holes [105], which are conjectured [106] to scramble information as fast as possible (i.e., they are "fast scramblers"). There have since been various proposals for how to measure OTOCs in the lab [107–112].

Meanwhile, there are a wide range of different materials that have a resistivity which varies linearly with temperature. A 2013 paper [113] by Bruin *et al* found that a diverse group of these materials have resistive scattering rates $1/\tau = \alpha k_B T/\hbar$ for α of order 1 despite having different scattering processes. This is suggestive of some universal bound on the scattering rate, which motivates an interest in finding realistic condensed matter Hamiltonians that saturate Maldacena's bound. Some progress to this end has been made; for example, Lashkari *et al* found that Brownian quantum circuits are fast scramblers (but have a time dependent Hamiltonian), and the Ising model on a random graph scrambles the eigenstates of σ_x (but not a generic state)[103]. Scrambling has been studied in other models

as well [114–118] and also experimentally [70, 119–121]. But the model that has generated the most interest has been a simplified Sachdev–Ye model [122] introduced by Kitaev and shown to saturate the Maldacena bound at low temperatures [123, 124]. This model, now known as the Sachdev–Ye–Kitaev (SYK) model, and its holographic dual have been the subject of extensive study over recent years [125–128].

In this chapter, we study the scrambling rate by calculating $C(t)$ through exact diagonalization, considering both the aforementioned Sachdev–Ye–Kitaev (SYK) model and a spinless Sachdev–Ye model analyzed by Sachdev in [129]. The goal was to develop methods with which to diagnose scrambling using finite size numerics by calibrating them in a system where we already knew how OTOCs were supposed to behave in the thermodynamic limit. This chapter mostly details the work done while I was the sole graduate student involved with the project, based on my notes rather than a publication-quality manuscript. Consequently, the analysis here is not quite as polished as in the other chapters of this thesis. For the second arc of this project most of my time was being spent on s-source, and I acted in more of a supporting role here with my fellow graduate student Bryce Kobrin leading; Ref. [24] summarizes our final results.

4.2 Background

We use the same definitions and notation as Maldacena *et al* in Ref. [1], and summarize their main result. They define a four operator correlation function $C(t)$ by

$$C(t) = -\langle [W(t), V(0)]^2 \rangle, \tag{4.1}$$

where $W(0)$ and $V(0)$ are in general any operators that are sums of products of $\mathcal{O}(1)$ degrees of freedom; note that the operators in the expansion of $C(t)$ are not time ordered. Here, angle brackets denote a thermal expectation value, $\langle A \rangle = Z^{-1} \operatorname{tr}\left[e^{-\beta H} A\right]$, and operators evolve as in the Heisenberg picture, $A(t) = e^{iHt} A(0) e^{-iHt}$. The authors also assume that V and W have zero thermal expectation value themselves, though we will consider some operators for which this is not the case. For a system that scrambles, $C(t)$ will start off at 0 at $t = 0$, and will remain negligibly small until the scrambling time t_*, after which it will saturate towards $2\langle VV \rangle \langle WW \rangle$. We are also interested in the dissipation time t_d, which is the characteristic time scale in which two operator expectation values decay.

The authors regularize $C(t)$ by moving one of the commutators halfway through the factor of $e^{-\beta H}$:

$$C'(t) = -\operatorname{tr}\left[y^2 \left[W(t), V(0)\right] y^2 \left[W(t), V(0)\right]\right], \tag{4.2}$$

where

$$y = e^{-\beta H/4}. \tag{4.3}$$

They then define a related function $F(t)$ as

$$F(t) = \operatorname{tr}\left[yV(0)yW(t)yV(0)yW(t)\right]. \tag{4.4}$$

$C'(t)$ can be rewritten as

$$C'(t) = \mathrm{tr}\left[y^2W(t)V(0)y^2V(0)W(t)\right] + \left[y^2V(0)W(t)y^2W(t)V(0)\right] - F(t+i\beta/4) - F(t-i\beta/4), \tag{4.5}$$

where the first two terms can be written as norms of states and thus remain of order 1. The Fs will initially cancel the first two terms, but will eventually decay giving rise to non-negligible value of $C'(t)$.

For a chaotic system for $t_d \ll t \ll t_*$, $F(t)$ will be approximately a constant F_d, where $F_d = \mathrm{tr}[y^2V(0)y^2V(0)]\,\mathrm{tr}[y^2W(0)y^2W(0)]$. In this regime, to lowest order in ϵ, we expect $F(t)$'s deviation from F_d to have the form

$$F_d - F(t) = \epsilon e^{\lambda_L t}, \tag{4.6}$$

where λ_L is a Lyapunov exponent. The main result of [1] is that

$$\lambda_L \leq \frac{2\pi}{\beta}. \tag{4.7}$$

For large N systems, $\epsilon = 1/N^2$, and we thus have a scrambling time of $t_* \sim \frac{\beta}{2\pi}\log N^2$ when the bound is saturated. These same systems are expected to have $t_d \sim \beta$.

4.3 Exact Diagonalization

4.3.1 SYK Model

In this study we calculate $C(t)$ for the Sachdev Ye Kitaev (SYK) model using exact diagonalization. The SYK Hamiltonian for a system of $2N$ Majorana fermions γ_i is

$$\mathcal{H}_{SYK} = \left(\frac{6}{(2N)^3}\right)^{1/2} \sum_{i<j<k<l} J_{ijkl}\gamma_i\gamma_j\gamma_k\gamma_l \tag{4.8}$$

The coefficients J_{ijkl} are taken to be independent random Gaussian variables with standard deviation J, which we set to 1 unless otherwise noted. We normalize our Majoranas such that $\{\gamma_i, \gamma_j\} = \delta_{ij}$.

For this model we choose our observables to be two of the Majoranas, $W = \gamma_i$ and $V = \gamma_j$ for $i \neq j$, and modify $C(t)$ slightly as γ_i and γ_j anticommute:

$$C(t) = \langle\{W(t), V(0)\}^2\rangle. \tag{4.9}$$

We then fit $C(t)$ to an analytic form derived for the infinite N limit in Ref. [125]:

$$C_f(t) = M(1 - (N_*e^{-\lambda t})^d U(d, 1, N_*e^{-\lambda t})), \tag{4.10}$$

where M is the long time limit of $C(t)$ (1/2 for the SYK model), U is the confluent hypergeometric U function, and d, N_*, and λ are fit parameters. Here U has the integral representation

$$U(a,b,z) = \frac{1}{\Gamma(a)} \int_0^\infty e^{-zt} t^{a-1} (t+1)^{b-a-1} dt, \quad \mathrm{Re}\, a > 1 \tag{4.11}$$

where $\Gamma(z)$ is the well-known gamma function

$$\Gamma(z) = \int_0^\infty e^{-t} t^{z-1} dt, \quad \mathrm{Re}\, z > 1. \tag{4.12}$$

Because this analytic form was derived in the large N limit, whereas we are studying small N systems, we make a distinction between $2N$, the number of Majoranas in our system, and the fit parameter N_*. We also expect that in the large N limit the scaling dimension d should be 1/2. Furthermore, we note that N_* and d should be independent of temperature; ultimately our aim is to find $\lambda(T)$ and see if it saturates the Maldacena bound.

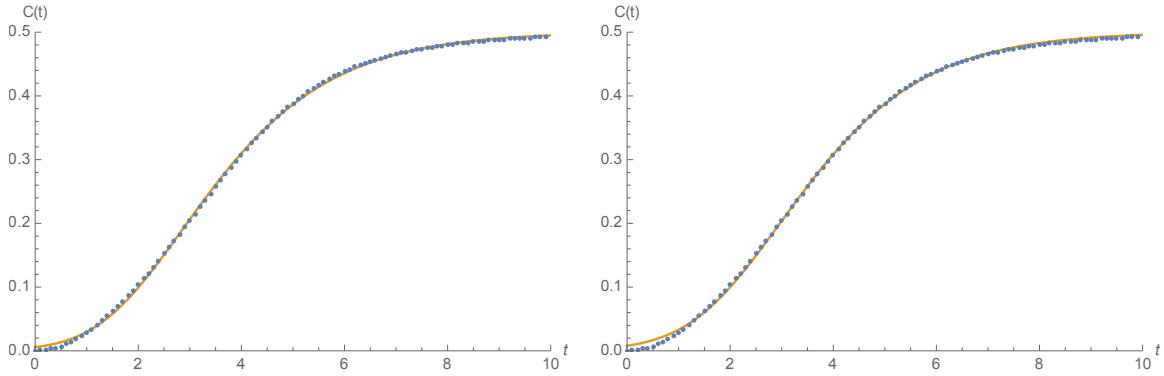

(a) (b)

Figure 4.1: Fits of $C(t)$ for the SYK model to the functional form $C_f(t)$. (a) Fit for N=10 and $T = 10^{-0.6}$ allowing all three parameters λ, N_*, and d to vary. (b) Fit for the same data only allowing λ and N_* to vary and fixing $d = 1/2$. Both fits approximate $C(t)$ quite well except in the vicinity of $t = 0$ where $C(t) = 0$; $C_f(t)$ can only reach 0 in the infinite N_* limit. We note that fixing a value of d results in a poorer fit in the vicinity of $t = 0$, but is otherwise still very good.

We first try fitting our numerical data of $C(t)$ for each temperature separately. A representative fit for $N = 10$ (20 Majorana fermions) at $T = 10^{-0.6}$ is shown in Fig. 4.1a. The functional form $C_f(t)$ which was derived in the infinite system size limit turns out to fit the data remarkably well despite the small size of our system. The one place that fails to be fit well is in the vicinity of $t = 0$; here we know that $C(0)$ must be identically 0, but $C_f(0)$

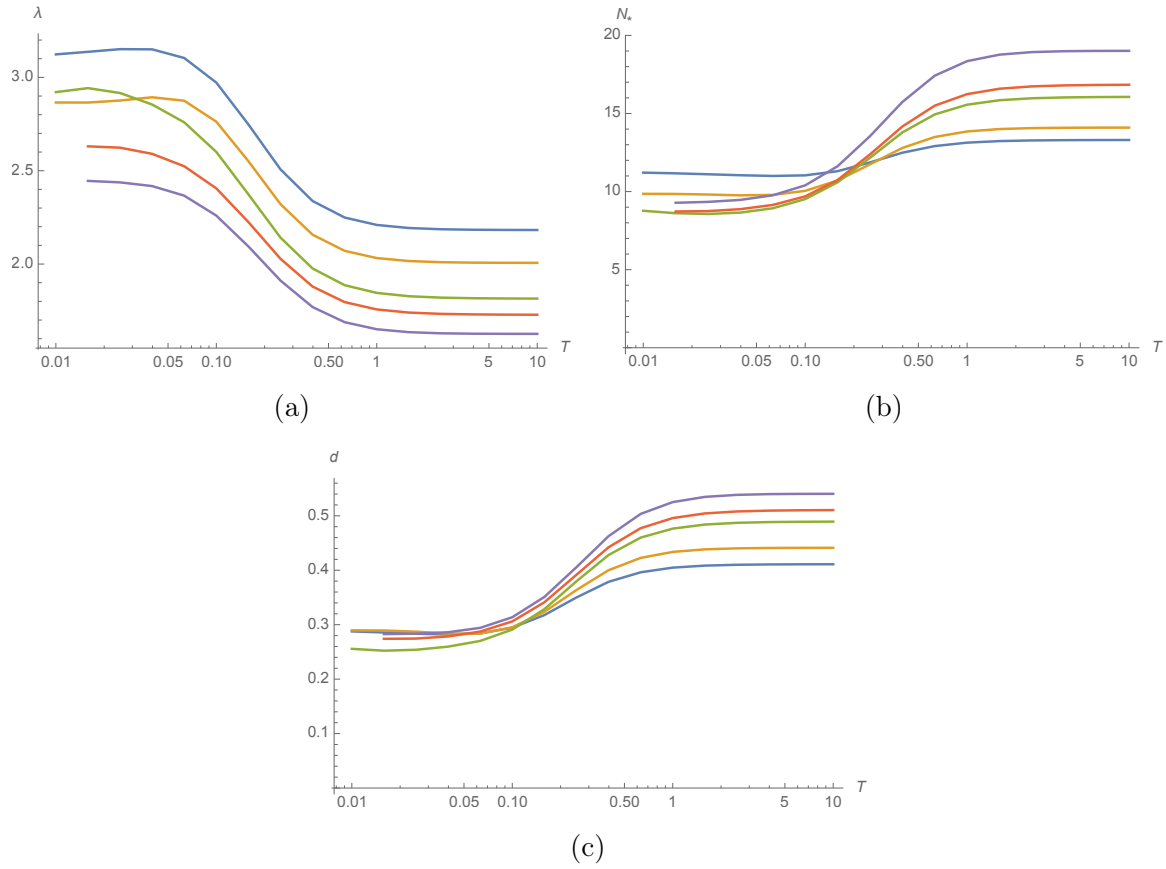

Figure 4.2: Extracted fit parameters (a) λ, (b) N_*, and (c) d for $C(t)$ for the SYK model of $2N$ Majorana fermions as functions of T. Here a separate fit is done for each value of T. Blue, orange, green, red, and purple correspond to N=6, 7, 8, 9, 10 respectively. Curves use 1000 disorder realizations for N=6, 7, 8, and 100 realizations for N=9, 10. The model self averages, so fewer disorder realizations are needed at larger system sizes.

can only be 0 in the infinite N_* limit. The extracted fit parameters are plotted in Fig. 4.2. Here the dependence of λ on T is actually opposite what we would expect from the bound; it decreases with temperature. This is because we are also allowing d and N_* to be fit, and indeed we see both parameters vary quite a bit from low T to high T. We also see that λ decreases as a function of system size, but the shape of the curve does not appear to change.

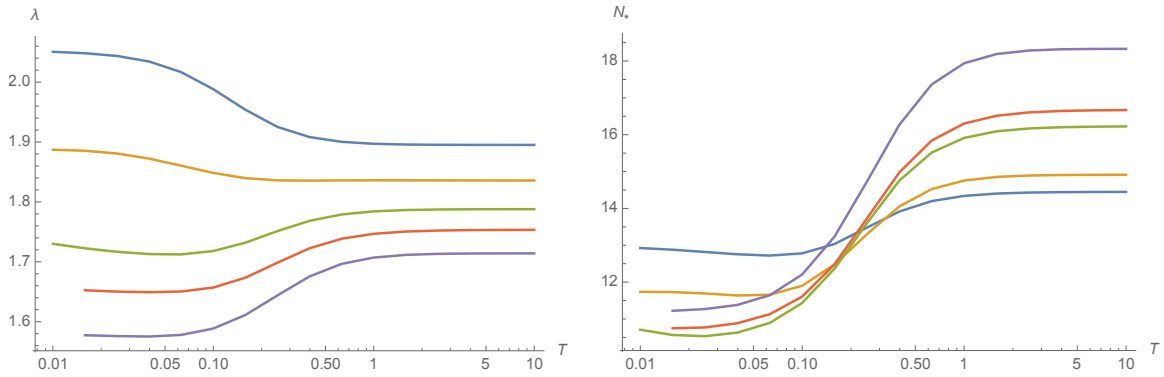

(a) (b)

Figure 4.3: Extracted fit parameters (a) λ and (b) N_* with d fixed to 1/2 for $C(t)$ for the SYK model of $2N$ Majorana fermions as functions of T. Again a separate fit is done for each value of T. Blue, orange, green, red, and purple correspond to N=6, 7, 8, 9, 10 respectively. Curves use 1000 disorder realizations for N=6, 7, 8, and 100 realizations for N=9, 10.

Next we fit the numerical data fixing d to 1/2 but still allowing λ and N_* to vary independently for each temperature. A representative fit for the same data as before ($N = 10$, $T = 10^{-0.6}$) is shown in Fig. 4.1b. The fit is still quite good besides in the vicinity of $t = 0$ where the fit is a bit worse than before. Fig. 4.3 shows the extracted fit parameters; notably, for systems of $2N = 16$ or more Majoranas λ actually increases as a function of T as we would expect from the Maldacena bound.

Physically, however, we know that d and N_* should not be temperature dependent like λ. This leads us to try fitting all of the data with separate fit parameters λ_i for each temperature, but only one N_* and d shared between all of the individual fit functions. We can do this by adding an index i to each data set and fitting the function $\sum_j \delta_{ij} C_f(\lambda_j, N_*, d; t)$. The results of this fit are shown in Fig. 4.4; similarly to the fixed d case we see that λ is decreasing as a function of T for small N, but then crosses over to the expected increasing behavior (slightly) for $N \geq 10$. N_* and d generally appear to increase with N, though we cannot tell if d will saturate towards the theorized value of 1/2. We are limited to small system sizes as the calculation takes an exponentially long time in N using exact diagonalization. Fits are shown in Figs. 4.4d–4.4f for $T = 10^{-1.8}$, $10^{-0.4}$, and 10 respectively, again for $N = 10$. These are noticeably worse than the earlier fits, which is to be expected; there is only one

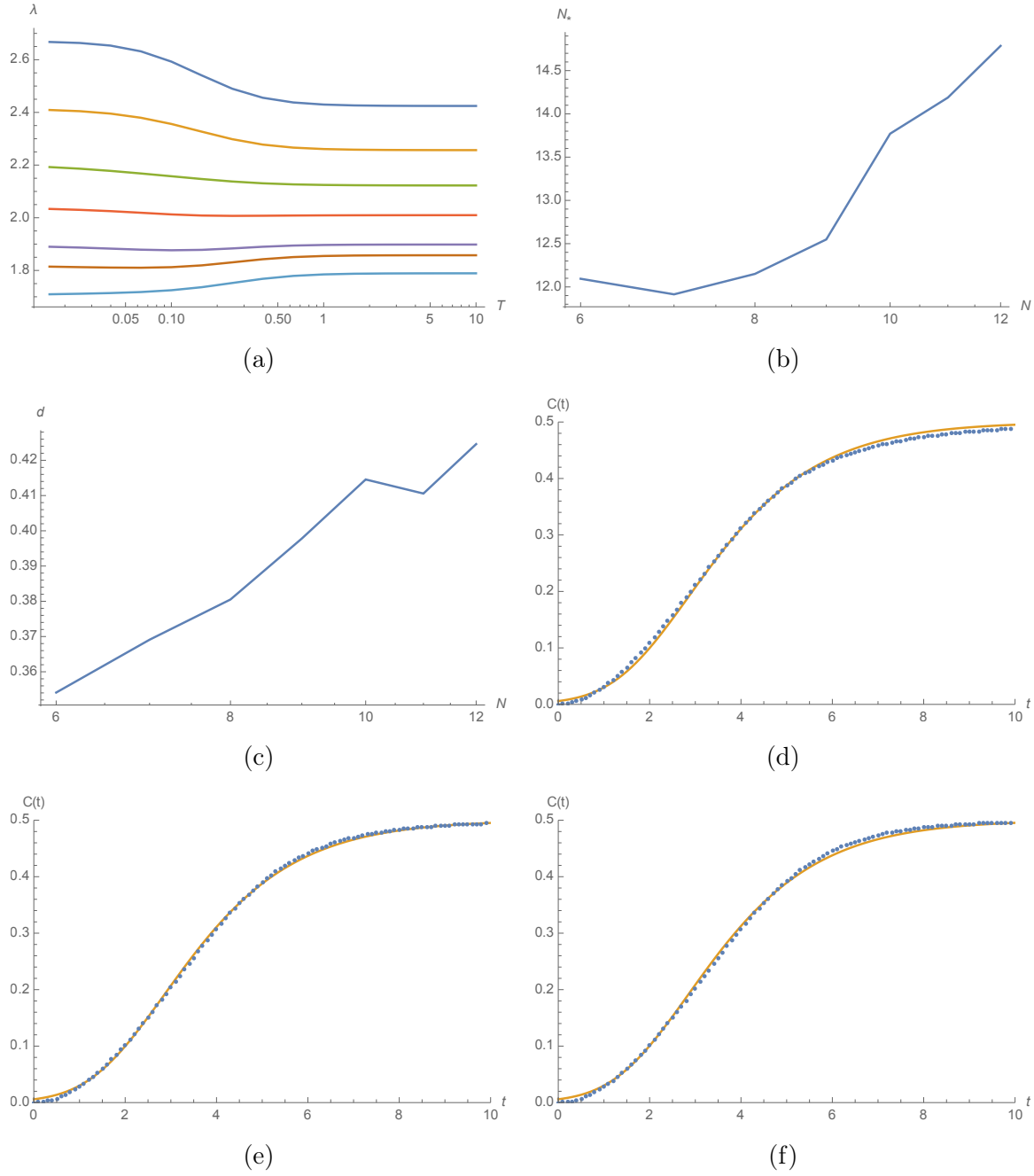

Figure 4.4: Extracted fit parameters (a) λ, (b) N_*, and (c) d for $C(t)$ for the SYK model of $2N$ Majorana fermions as functions of T. Here a single fit is done across all values of T with only λ allowed to vary with T; N_* and d are plotted as functions of half system size N. Dark blue, orange, green, red, purple, brown, and light blue correspond to N=6, 7, 8, 9, 10, 11, 12 respectively. Curves use 1000 disorder realizations for N=6, 7, and 8, 100 realizations for N=9, and 10, and 50 realizations for N=11. The next three plots show fits for an $N = 10$ system for (d) $T = 10^{-1.8}$, (e) $T = 10^{-0.4}$, and (f) $T = 10$.

parameter (λ) which independently varies for a given T, rather than two or three as before. The fits are still pretty good though, and are better for intermediate temperatures than very low or high temperatures.

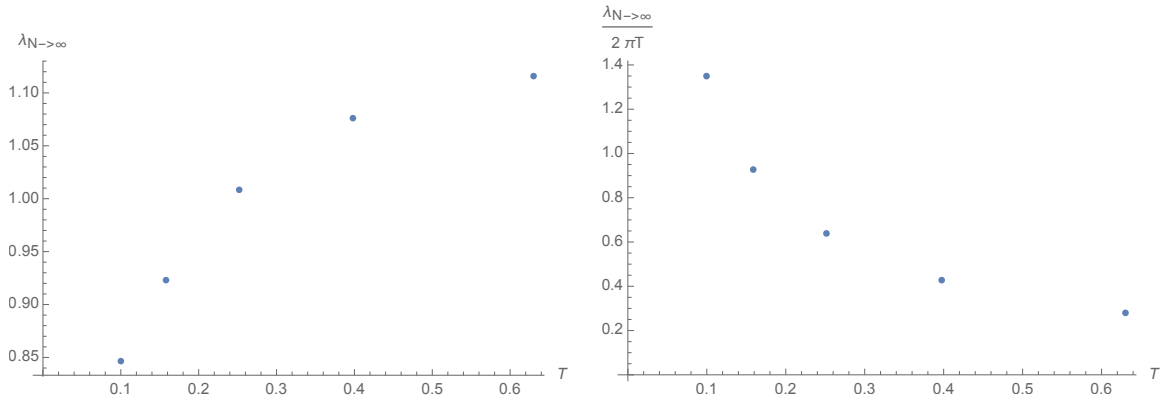

(a) (b)

Figure 4.5: (a) Extrapolated λ in the $N \to \infty$ limit, found by fitting $\lambda(N)$ to the form $a + b/N$ for each fixed value of T and taking the resulting values of a to be $\lambda_{N\to\infty}$. (b) Extrapolated λ in the $N \to \infty$ limit divided by the Maldacena bound, $2\pi T$. Note that the T axis is not on a log scale, in contrast to earlier plots.

In an effort to see beyond the small systems for which we can directly calculate $C(t)$, we next extrapolate our scrambling rate data (specifically, we use the λ values shown in Fig. 4.4) to the $N \to \infty$ limit. We do this by fitting $\lambda(N)$ to the form $a + b/N$ for each fixed value of T and plotting $a(T)$, as shown in Fig. 4.5a. We also plot $a(T)$ divided by the Maldacena bound, $2\pi T$, in Fig. 4.5b. For small T, $a(T)/(2\pi T)$ crosses through 1, but clearly we're not finding our desired temperature scaling. Considering the finite size effects at play here, this is not entirely surprising. For a finite size system we will be essentially in the ground state at low enough temperature and essentially in a $T = \infty$ state for a high enough temperature, as we indeed see from the fit parameters for around $T < 0.1$ or $T > 1$, respectively. Going up to much higher system sizes and more careful finite size scaling analysis in our paper [24] produce a more favorable comparison to theoretical expectations.

Finally, there is the question of the stability of our fits as a function of which temperatures we collectively fit. Recall that we are fitting across a range of temperatures each of which want their own optimal values of N_* and d, so if we were to change the scope of the data we were fitting we might expect that our fit parameters shift. The data above used logarithmically spaced values of T from $T = 10^{-1.8}$ to $T = 10$, each point separated by a factor of $10^{0.2}$. λ only varies substantially around the middle of that range, so we don't expect our fit to be unduly biased by high or low T data. Nevertheless, we check the extent of variations due to this choice in Fig. 4.6. Here we see that as we successively drop the

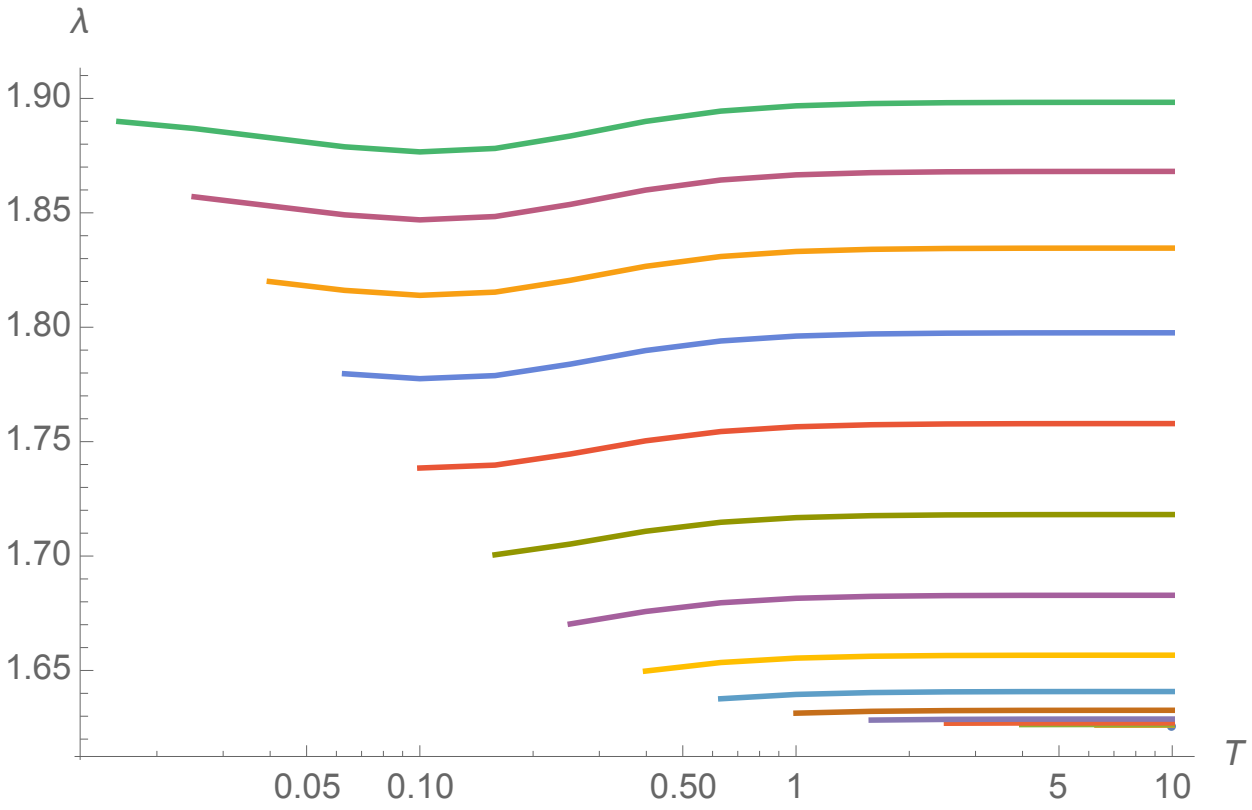

Figure 4.6: Plot of $\lambda(T)$ for $N = 10$ with the fit taken across temperatures from $T = 10^{-1.8}$ and ending at $T = 10$, successively dropping the lowest temperature (as can be seen by each line starting further to the right). This results in λ dropping from around 1.9 to 1.6 once we are only using one temperature's worth of data. The drop in λ is fairly uniform as a function of T.

lowest temperature data λ decreases (more or less uniformly in T) by around 15%, from 1.9 to 1.6.

4.3.2 Sachdev Model

We also consider a variant of the Sachdev–Ye model which was analyzed analytically by Sachdev in [129]. This model, however, is spinless, and unlike SYK does not use Majoranas. The Hamiltonian we use for an N site system is

$$\mathcal{H}_S = \frac{4}{(2N)^{3/2}} \sum_{i<j,k<l} J_{ijkl} c_i^\dagger c_j^\dagger c_k c_l \tag{4.13}$$

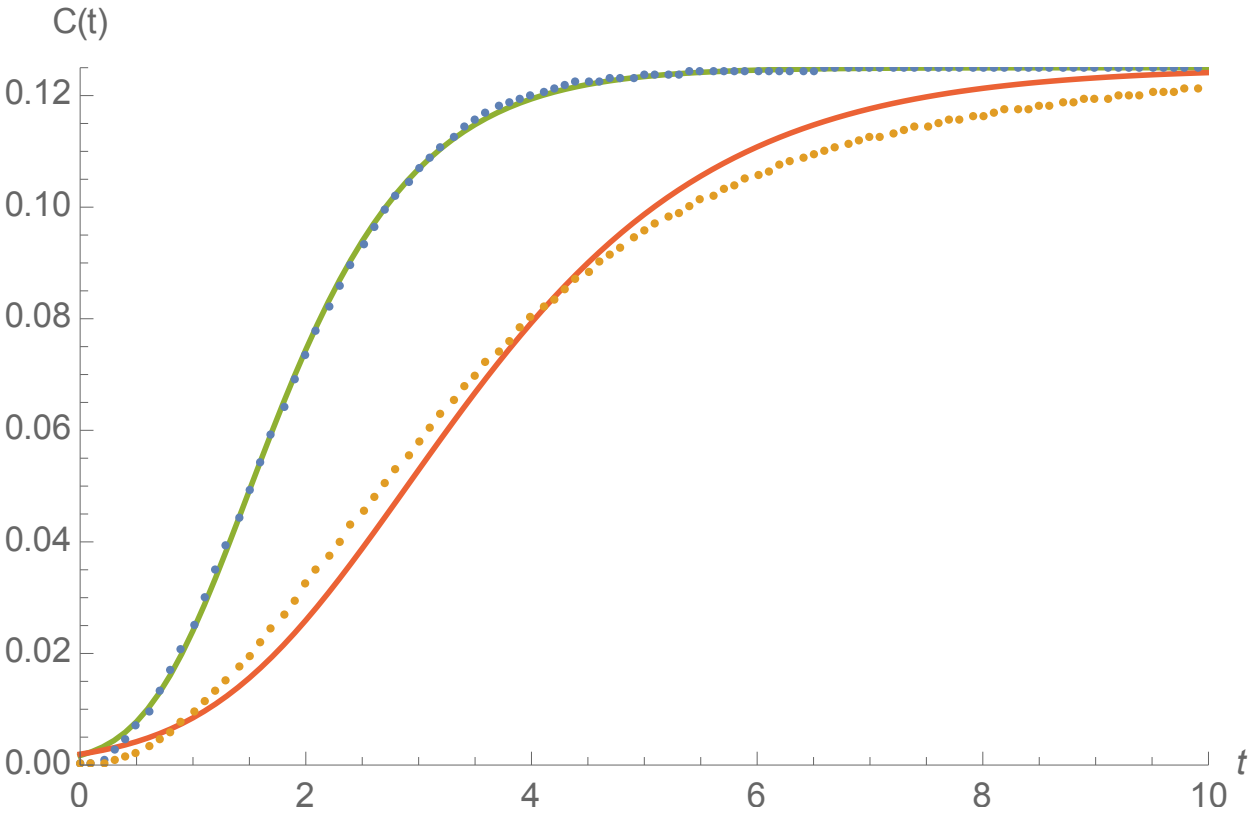

Figure 4.7: Fits for the Sachdev model with $N = 10$ and $T = 0.5$ for $R = 10$ (blue/green) and $R = 6$ (orange/red). The same functional form as for the SYK model, $C_f(t)$, (with $M = 0.125$) fits the full range ($R = 10$) Sachdev model, but does not fit well for $R < N$. The multi-parameter fit for $R = 6$ does not converge, so here we adjust N_* and d by hand and then fit λ to get an approximate fit.

where we do not consider an onsite potential as Sachdev does. The c_i's obey the standard fermionic anticommutation relations, $\{c_i, c_j\} = \{c_i^\dagger, c_j^\dagger\} = 0$ and $\{c_i, c_j^\dagger\} = \delta_{ij}$. The J_{ijkl}'s are again independent Gaussian variables with standard deviation J. Finally, we define a maximum range of interaction R, such that $J_{ijkl} = 0$ if any two indices are more than R away from each other. Because the total density $\rho = \frac{1}{N}\sum_i c_i^\dagger c_i$ is conserved, we calculate $C(t)$ at half filling $\rho = 1/2$ and use $V = n_0 = c_0^\dagger c_0$ and $W = n_{N/2} = c_{N/2}^\dagger c_{N/2}$, though as mentioned before the qualitative results will not depend on the specific choice of W and V. We also take open boundary conditions as this allows us to examine a wider range of R.

The same functional form $C_f(t)$ (with $M = 1/8$) turns out to fit $C(t)$ for the maximum range version of this model very well, as can be seen in the green curve in Fig. 4.7; here $N = 10$, $T = 0.5$, and $R = 10$. However, if we decrease the range of the interaction we no longer obtain a good fit; this can be seen in the red curve in the same figure for $R = 6$. The

multi-parameter fit does not converge here for $R < N$, so we adjust N_* and d by hand and then do a single variable optimization for λ to get an approximate fit. We conclude that $C_f(t)$ is the correct functional form for $C(t)$ for the full range version of the Sachdev model, but unsurprisingly not for the limited range version.

4.3.3 Final results

As mentioned previously, the work described in this chapter was not the end of the story for this project. Over the few years following the story I've presented so far, we used more powerful numerical techniques than exact diagonalization (in particular, Krylov subspace methods and mass parallelization [98, 130]) to push to much larger system sizes, and did more sophisticated analysis to extrapolate the Lyapunov exponent. The full details are given in our paper, Ref. [24], but the final results are given in Fig. 4.8. Note that the x axis for subfigure b is βJ rather than T, and that what we've been calling N is $2N$ in the caption's notation. The black dashed line is the more sophisticated analytic expectation for λ found by solving the Schwinger–Dyson equations, as derived in Refs. [123, 124]. As seen in the figure, we actually do end up with excellent agreement to the theory just based on inferences from our finite size numerics.

4.4 Conclusions

To summarize, we calculate the four operator out of time ordered correlator $C(t)$ for small system sizes for the SYK model using exact diagonalization. We fit to an analytic expression for $C(t)$ derived for the SYK in the large N limit, and find that the functional form is valid even for small system size. We extract the scrambling rate $\lambda(T)$ from our fits, extrapolate our data to infinite N, and compare it to the Maldacena bound, $2\pi T$. Our numerics do not match the bound, but come within a factor of order 1 for the relevant temperature range. Finally, we show that the same functional form for $C(t)$ is also valid for an ordinary fermion variant of the Sachdev-Ye model, but does not fit a shorter range version of the model.

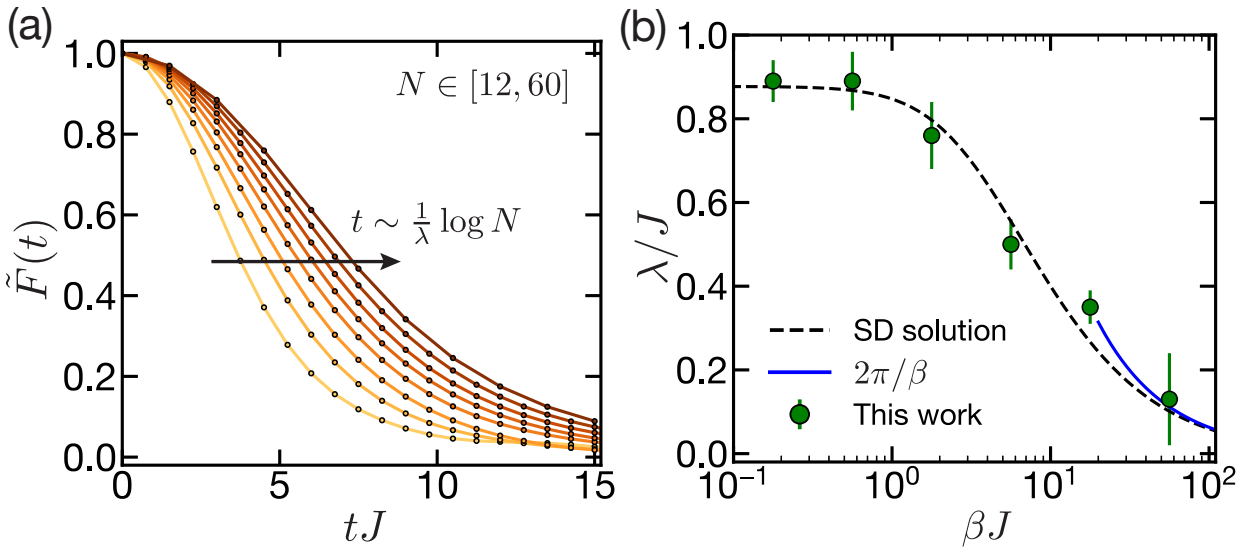

Figure 4.8: Regularized OTOCs in the SYK model, $\tilde{F}(t) \equiv F(t)/F(0)$, as shown for $\beta J = 10$ and system sizes $N \in [12, 60]$. The early-time behavior is characterized by $1 - \tilde{F}(t) \sim e^{\lambda t}/N$ and different system sizes are approximately related by a time translation symmetry, $t \to t + 1/\lambda \log N$. (b) Applying a finite-size rescaling procedure to the data, we determine λ as a function of temperature (points). Our results exhibit excellent agreement with the theoretical predictions of the Schwinger–Dyson (SD) equations (dashed line), including in the regime where λ approaches the bound on chaos $2\pi/\beta$ (blue). Figure taken from Ref. [24].

Chapter 5

Symmetric Bloch oscillations

This last chapter is reproduced from Ref. [25]. The original paper details both the experimental realization of large momentum splitting states created through symmetric Bloch oscillations as well as the theory behind the protocol. I was involved only in the latter, and have thus removed the experimental sections from this thesis chapter (though some summary of the experimental results remain in the introduction and conclusion to help contextualize the theory). It was already known that one can create a large momentum state by accelerating an optical lattice, with the initial state adiabatically evolving through a series of higher momentum states through successive Landau–Zener transitions [131, 132]. Here, the experiment showed that one could also take an initial zero momentum state and create a symmetric superposition of left and right moving states by accelerating *two* optical lattices in opposite directions.

The experiment was, in fact, already done prior to my involvement; the method worked much better than had been expected. The lead graduate student on the project, Zachary Pagel, had already started doing numerical simulations. After joining on, I worked to help develop the theoretical basis for the protocol's success. Early in our collaboration, I made probably my most important contribution by showing that if one moves to a basis of symmetric and antisymmetric momentum states, those two sectors completely decouple. I also worked out the explicit condition required for the rotating wave approximation we needed to make to be valid. Taken together, these two simplifications reduce the problem to one analogous to that of the single accelerated lattice (at least when said rotating wave approximation applies).

5.1 Introduction

Bloch oscillations and the Wannier–Stark ladder of matter waves in a periodic potential were first studied in the context of electrons in crystals in the presence of a homogenous electric field [133, 134]. Their counterintuitive nature—that a constant electric field should lead to an ac current—triggered a debate about their existence [135, 136] and led to the formulation

of criteria for their observability [137]. Bloch oscillations were first experimentally observed in semiconductor superlattices [138, 139], and have since been studied in a wide variety of physical systems ranging from Bloch oscillations of light [140, 141] to cold atoms [142, 143]. Bloch oscillations are particularly useful in matter wave interferometers, which have found widespread applications in precision measurements of fundamental constants [144–147], tests of the weak equivalence principle [148, 149] and dark energy theories [150, 151], as well as precision gravimetry [152, 153] and gradiometry [154].

Matter wave interferometers use optical lattices to coherently transfer momentum, allowing one to split a matter wave between different spatial trajectories, then later recombine them and create interference. The measured phase can be increased by using larger momentum splitting between the trajectories [144, 145]; Bloch oscillations enable such a process [142, 155] and have recently shown to coherently transfer the momentum of more than 10^4 photons to the atoms [156]. With two superposed lattices that are independently accelerated, it might even be possible to realize large-momentum-transfer beam splitters for matter waves, by performing Bloch oscillations of two different velocity classes of atoms simultaneously [157]. However, this process has never been demonstrated. Near velocity degeneracy of the two accelerated lattices, it was expected that non-adiabatic effects would prevent coherent ground state dynamics. Instead, Bloch oscillations have only been used to accelerate atoms after an initial momentum splitting was already made with Bragg diffraction [144, 158], resulting in up to $408\hbar k$ momentum splittings [159, 160], where k is the wavevector of the laser.

Here, we show that Bloch oscillations of atoms in two symmetrically accelerated lattices can remain adiabatic and coherent even as the two lattices pass through velocity degeneracy. Theoretically, we show that it is possible to split, reflect, and recombine atoms simply by allowing them to adiabatically follow the ground state of the Hamiltonian while accelerating the two lattices. The dynamics result in symmetric Bloch oscillations where the matter wave is in a coherent superposition of interacting with each of the two lattices, and the relative phase and velocity of the two lattices completely determines the trajectories of different branches of the matter wave. Experimentally, we demonstrate symmetric Bloch oscillations and realize $240\,\hbar k$ coherent momentum splitting of a superposition state as well as interferometry with nearly fully-guided matter waves.

Using only accelerated lattices for momentum transfer is desirable for a number of reasons. In comparison with resonant processes such as Bragg diffraction, 1) the dynamics are adiabatic, and can therefore be much more efficient per $\hbar k$ momentum transfer, 2) the processes require less laser power, 3) the velocity class of atoms addressed can be larger, relaxing temperature requirements on atom clouds, and 4) the optical lattices prevent thermal expansion of the atom cloud, further relaxing temperature requirements. As a result, symmetric Bloch oscillations can find applications in next-generation precision measurements of fundamental constants, searches for gravitational waves, and searches for new physics [149, 151, 161–163].

Section 5.2 presents a theoretical treatment of the Hamiltonian and the resulting dynamics. The Hamiltonian is symmetric under momentum inversion, allowing one to simultane-

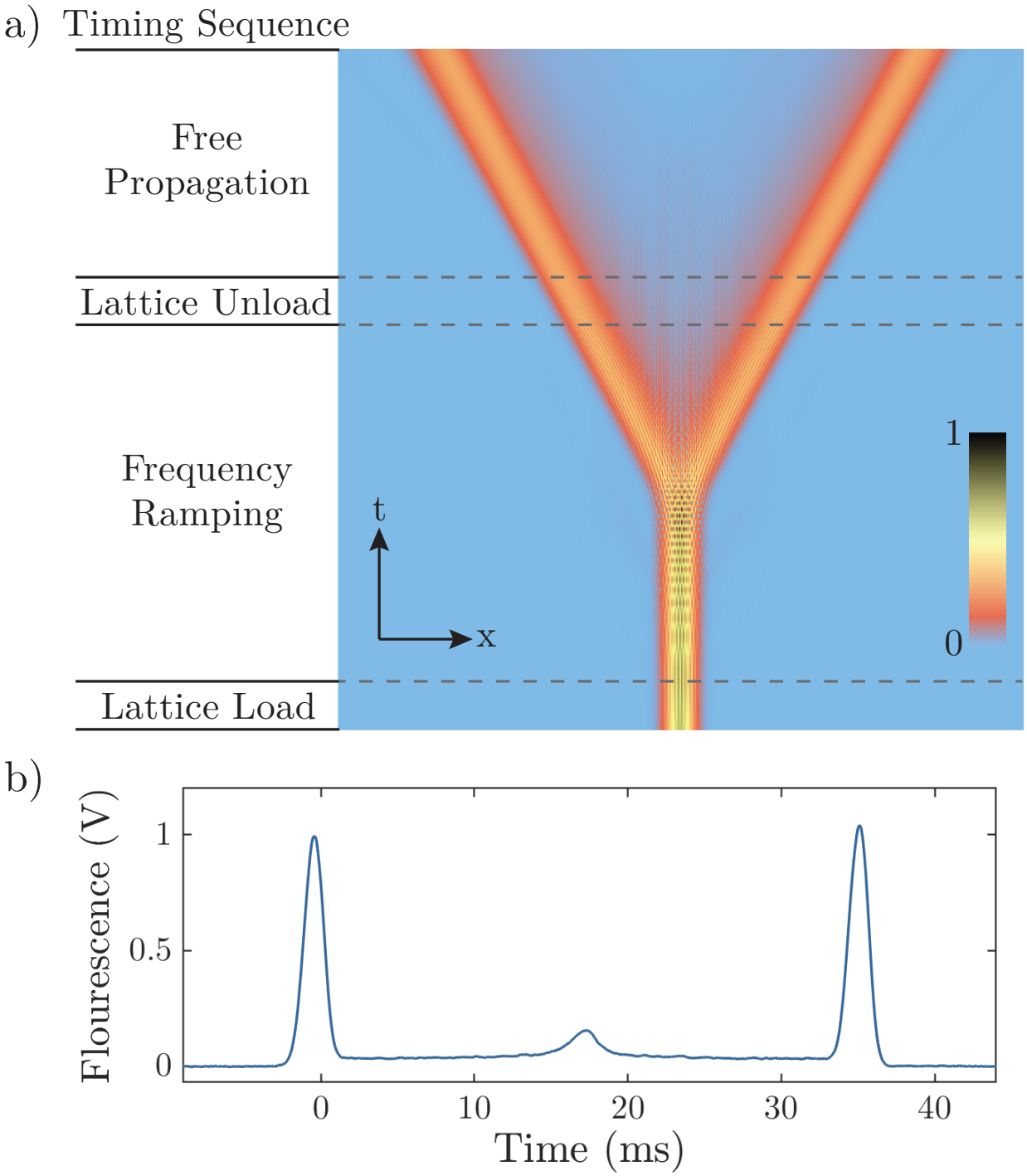

Figure 5.1: a) Density plot of $|\psi(x,t)|$ from numerical simulation of a symmetric beamsplitter with a lattice depth $U_0 = 1.3\,E_r$ and ramp rate $r = 0.2\,\omega_r^2$. Timing sequence is indicated on the left. The initial wavefunction is a Heisenberg-limited gaussian wavepacket with velocity spread $0.05\,v_r$, corresponding to our experimental temperature. Frequencies are ramped for one Bloch period, corresponding to a $4\hbar k$ splitting between arms. b) Experimental time of flight fluorescence trace showing an efficient $60\hbar k$ beamsplitter with a ramp rate $r = 0.26\,\omega_r^2$, and a lattice depth of around $1.5\,E_r$.

ously diagonalize the Hamiltonian in momentum parity and energy. For the beamsplitter process described above, we show that an atom adiabatically follows the even-parity ground state of the Hamiltonian. The momentum-parity basis is then used to study effects such as non-adiabatic losses, dynamics while ramping the lattices through velocity degeneracy, and effects from different experimental imperfections.

Though omitted from this thesis chapter, the interested reader should consult Section III of the paper this chapter is based upon, Ref. [25], in which we describe how we implement symmetric Bloch oscillations experimentally. We use the relative phase between the two lattices to control the populations in the two lattices after ramping through velocity degeneracy; in effect, this creates a fully tunable matter-wave switch each time the lattices cross through velocity degeneracy. We demonstrate the first interferometers created only using accelerated lattices, including a Mach–Zehnder (MZ) interferometer with a momentum splitting of up to $240\hbar k$. Prior to this work, the largest momentum transfer from a single beamsplitter operation was $24\hbar k$ [164]. In order to confirm that symmetric Bloch oscillations are first-order phase coherent, we implement a differential measurement between two simultaneous MZ interferometers and see a stable phase between the interferometer outputs.

Finally, Section 5.4, originally the appendix, expands upon various technical details omitted from the rest of the chapter.

5.2 Theory

When two superposed optical lattices are far apart in velocity, it is well known that atoms can undergo efficient Bloch oscillations in either of the lattices [144, 158–160]. Near velocity degeneracy, however, it was previously expected that near-resonant effects from the second lattice would cause too large of a perturbation to the standard Bloch oscillation dynamics to permit an efficient beamsplitter. We first derive a unitary transformation that isolates the relevant dynamics (Sec. 5.2.1), and then show that the effects of the perturbation terms can remain small within the rotating wave approximation under certain conditions (Sec. 5.2.2). Throughout the analysis, it is useful to stress the parallels between Bloch oscillations in a single lattice (SLBO) and Bloch oscillations in two lattices which we call dual-lattice Bloch oscillations (DLBO). The simplified DLBO Hamiltonian is nearly identical to the SLBO Hamiltonian, differing only in being invariant under momentum inversion. As a result, the eigenstates of DLBO are symmetric and anti-symmetric in momentum space.

We then study non-adiabatic loss mechanisms, which include standard Landau–Zener tunneling due to avoided level crossings as well as higher-order transitions which are possible due to perturbation terms dropped in the rotating wave approximation (Sec. 5.2.3). These conditions are combined to place limits on the permissible lattice accelerations and lattice depths, and in total they allow for the DLBO to approach 100% efficiency in the limit of slowly accelerated lattices (Sec. 5.2.4). The dynamics are also discussed for lattices that are ramped through velocity degeneracy, showing that an offset laser phase can be used to coherently control the output population in the two lattices (Sec. 5.2.5). Lastly, we

discuss some important experimental requirements in order to realize these methods in the laboratory (Sec. 5.2.6), and supporting material is left for Sec. 5.4.

5.2.1 Hamiltonian and unitary transformation

SLBO are most easily studied using a coordinate system that is comoving with the accelerating lattice [132, 165, 166], and a unitary transformation can be used to boost the Hamiltonian between the atom's inertial frame and the accelerating lattice frame [131, 132]. For DLBO, it is not possible to transform to a coordinate system that is simultaneously comoving with both lattices. Instead, using a basis of momentum states it is possible to independently transform each momentum state so that positive (negative) momentum states are boosted to a coordinate system comoving with the positively (negatively) accelerating lattice. This unitary transformation is shown to capture the core coherent dynamics of DLBO. The analysis that follows is relevant for zero temperature atoms comoving with the initially degenerate lattices: a similar analysis can be explored for atoms with a small initial velocity, and the band structure of the Hamiltonian can still be studied. One finds that any initial velocity breaks the parity symmetry discussed in the following sections and leads to asymmetric dynamics. A full analysis is beyond the scope of this chapter.

We begin with a Hamiltonian containing the AC Stark shift of two superposed optical lattices that are far detuned from single-photon transitions (see Fig. 5.2). Experimentally, the lattices are realized with one upward-propagating laser frequency ω_1, and two downward-propagating frequencies $\omega_2 \pm \omega_m(t)$. We work in the frame of reference where $\omega_1 = \omega_2 = \omega$, and denote $\omega_\pm = \omega \pm \omega_m(t)$. The relative speed of the two lattices is given by $\omega_m(t)/k$, where k is the wave number of the laser defined as $k = \omega/c$. Two-photon transitions leave atoms in the same internal state but different external momentum states. After adiabatic elimination of the excited state, the Hamiltonian for an atom in these two optical lattices can be written as:

$$\begin{aligned} H_{\mathrm{BBS}}(t) &= \frac{\hat{p}^2}{2m} + \frac{U_0}{2}\left(\cos\left[2k_+\hat{x} + \int_0^t \omega_m\left(t'\right) dt' + \phi_1\right] + \cos\left[2k_-\hat{x} - \int_0^t \omega_m\left(t'\right) dt' + \phi_2\right]\right) \\ &= \frac{\hat{p}^2}{2m} + U_0\, \cos\left[2k\hat{x}\right] \cos\left[\int_0^t \omega_m\left(t'\right) dt' + \phi_0\right]. \end{aligned} \tag{5.1}$$

Constant terms are dropped in the second form, which will be used for analytics and simulation. The wave numbers $k_+ = \omega_+/c$ and $k_- = \omega_-/c$ are nearly identical to k, so we approximate $k_+ \approx k_- \approx k$ in the second form as well. For Cs atoms separated by $n = 1000$ photon momenta, k_+, k_-, and k differ by less than one part in 10^8. The phases ϕ_0, ϕ_1, and ϕ_2 are offsets between counter-propagating lasers at time $t = 0$. The lattice depth $U_0 = \hbar\Omega_R^2/(2\Delta)$ is the AC Stark shift for a single, far-detuned lattice [165], where Δ is the detuning from the excited state and Ω_R is the on-resonance Rabi frequency between the

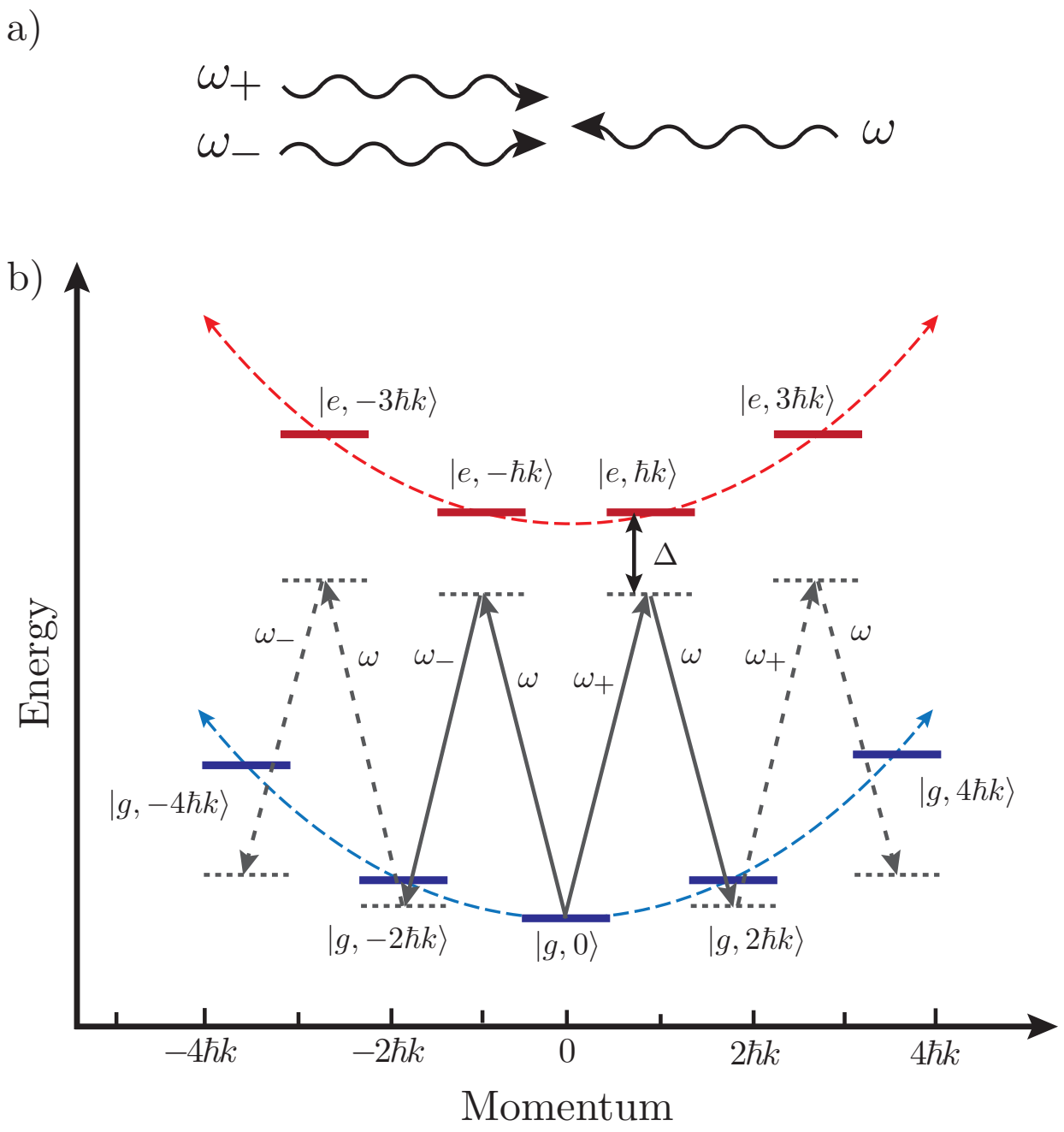

Figure 5.2: a) Counter-propagating lasers form two superposed optical lattices. The frequency differences are $\omega_+ - \omega = \omega - \omega_- = \omega_m$. b) Energy-momentum level diagram showing relevant atomic states. The lasers drive two-photon transitions between neighboring momentum states such that the atom remains in the same internal ground state. The detuning from the excited states Δ (many GHz) is much larger than the separation between adjacent ground states (few kHz). As the modulation frequency ω_m is swept away from zero, the lasers sweep past a succession of two-photon transitions between adjacent ground states. Off-resonant transitions driven by the extra oscillating terms in the Hamiltonian (Eq. 5.4) are omitted for clarity.

ground and excited states. The integral $\int_0^t \omega_m(t')\,dt'$ keeps track of the phase evolution of the lattice for time dependent frequencies. Specializing to linear frequency ramps with rate r, the modulation frequency can be written as $\omega_m(t) = rt$ so that the lattices are velocity degenerate at time $t = 0$ and $\int_0^t \omega_m(t')\,dt' = rt^2/2$. This ramp rate corresponds to an acceleration $a = r/2k$.

We now write the Hamiltonian in a momentum-state basis $|l\rangle$, where l is an integer that labels the basis states such that the state $|l\rangle$ has $2l\hbar k$ momentum. Plane-wave basis states are a good approximation to initial atomic states when the velocity spread is much smaller than the recoil velocity $v_r = \hbar k/m$. Projected into this basis, the Hamiltonian is:

$$H = \sum_{l=-\infty}^{\infty} \left(\frac{(2l\hbar k)^2}{2m} |l\rangle\langle l| + U_0 \cos\left(\frac{rt^2}{2} + \phi_0\right) (|l\rangle\langle l+1| + |l\rangle\langle l-1|) \right) \tag{5.2}$$

The unitary transformation used to boost the different momentum states in this Hamiltonian is given by:

$$U = \sum_{l=-\infty}^{\infty} e^{i\frac{d(t)|\hat{p}|}{\hbar}} e^{i\frac{\theta(t)}{\hbar}} |l\rangle\langle l| \tag{5.3}$$

where $d(t) \equiv at^2/2 + \phi_0/k$ and $\theta(t) \equiv ma^2t^3/6$. The first term corresponds to the position translation operator, and the absolute value sign ensures that positive momentum states are translated with the positive-moving lattice while negative momentum states are translated with the negative-moving lattice. The $d(t)$ term in Eq. (5.3) also absorbs the offset phase ϕ_0 into the definition of the basis states. The $\theta(t)$ in Eq. (5.3) corresponds to a global energy shift to each state such that the energy of the ground states comoving with either of the lattices stays near zero at all times [131]. See Section 5.4.1 for the analogous treatment of the SLBO Hamiltonian.

The transformed Hamiltonian $H' = UHU^\dagger + i\hbar\frac{dU}{dt}U^\dagger$ is:

$$\begin{aligned} H' = \sum_{l\neq 0} \Bigg[& \frac{(2|l|\hbar k - Ft)^2}{2m} |l\rangle\langle l| \\ & + \frac{U_0}{2}\left(1 + e^{is_l(rt^2+2\phi_0)}\right)|l\rangle\langle l+1| + \frac{U_0}{2}\left(1 + e^{-is_l(rt^2+2\phi_0)}\right)|l\rangle\langle l-1| \Bigg] \\ & + \frac{(Ft)^2}{2m}|0\rangle\langle 0| + \frac{U_0}{2}\left(1 + e^{-i(rt^2+2\phi_0)}\right)(|0\rangle\langle 1| + |0\rangle\langle -1|) \end{aligned} \tag{5.4}$$

where $s_l \equiv l/|l|$ is the sign of the momentum state, and the force $F = rm/2k$ is adapted from the standard treatment of SLBO [165].

The nearest-neighbor coupling terms proportional to $|l\rangle\langle l \pm 1|$ include both a stationary term and an oscillating term. In a two-level system, oscillating coupling terms of this type can be dropped under a rotating wave approximation (RWA) provided the terms time-average to zero on the relevant timescale of the dynamics. Here, the couplings between neighboring

momentum states can be treated with an analogous RWA to arrive at the reduced DLBO Hamiltonian:

$$H_{\mathrm{DLBO}} = \sum_{l=-\infty}^{l=\infty} \frac{(2|l|\hbar k - Ft)^2}{2m} |l\rangle\langle l| + \frac{U_0}{2} \left(|l\rangle\langle l+1| + |l\rangle\langle l-1|\right) \tag{5.5}$$

The validity of this RWA is discussed in Sect. 5.2.2, where we derive bounds on the ramp rate for which the Hamiltonian in Eq. (5.5) is valid.

The DLBO Hamiltonian in Eq. (5.5) and the SLBO Hamiltonian derived in Section 5.4.1 are nearly identical; the only difference is the absolute value $|l|$ in the kinetic energy term for H_{DLBO}, which makes H_{DLBO} symmetric under momentum inversion. This symmetry is already apparent in the original Hamiltonian (5.1), which commutes with a momentum inversion operator. Using a basis of momentum eigenstates that are also eigenstates of momentum-parity, the even- and odd-parity states are decoupled.

Figure 5.3 (a,b) shows the energy band structure over time of the Hamiltonian (5.5) for even- and odd-parity states, respectively, where the two lattices are ramped away from velocity degeneracy beginning at time $t = 0$. The energy bands are calculated by finding eigenvalues of a truncated version of the Hamiltonian in Eq. (5.5) as a function of time. Note that in plotting the energy bands in Fig. 5.3c, for negative times we use the substitution $d(t) \to -d(t)$ in Eq. (5.3) in order to use the coordinate frame comoving with the lattices driving amplitude towards zero momentum instead of driving amplitude away from zero momentum.

A beamsplitter can be understood as an atom adiabatically following the even-parity ground state of the Hamiltonian (5.5), and higher efficiency beamsplitters can be achieved by making the process more adiabatic. At every time $t = (a + 1/2)T_B$ for integers $a \geq 0$, where the Bloch period $T_B = 8\omega_r/r$ and the recoil frequency $\omega_r = \hbar k^2/(2m)$, there is a level crossing such that the even-parity state receives an additional $4\hbar k$ momentum splitting; the positive momentum component of the even state acquires an additional $+2\hbar k$ momentum and the negative momentum component acquires an additional $-2\hbar k$ momentum. This is the momentum-symmetric analogue of SLBO in the ground Bloch band, where atoms receive $2\hbar k$ momentum at the edge of the first Brillouin zone at each avoided level crossing between the ground band and first excited band.

5.2.2 Limits on ramp rate from the rotating wave approximation

A RWA can be used to drop the oscillating coupling terms in Eq. (5.4) provided that the time-average of the oscillating term e^{irt^2} is $\ll 1$ on the relevant timescale of the dynamics, namely the duration of first level crossing between the ground even band and the first excited even band. This crossing occurs at time $t = T_B/2$, and the time interval during which the level crossing happens is given by $\Delta t = 2\sqrt{2}U_0/(\hbar r)$. A simplified form of the resulting inequality gives an upper limit on the ramp rate for which the RWA is valid:

$$r \ll 4U_0(2\sqrt{2}E_r - U_0)/\hbar^2 \tag{5.6}$$

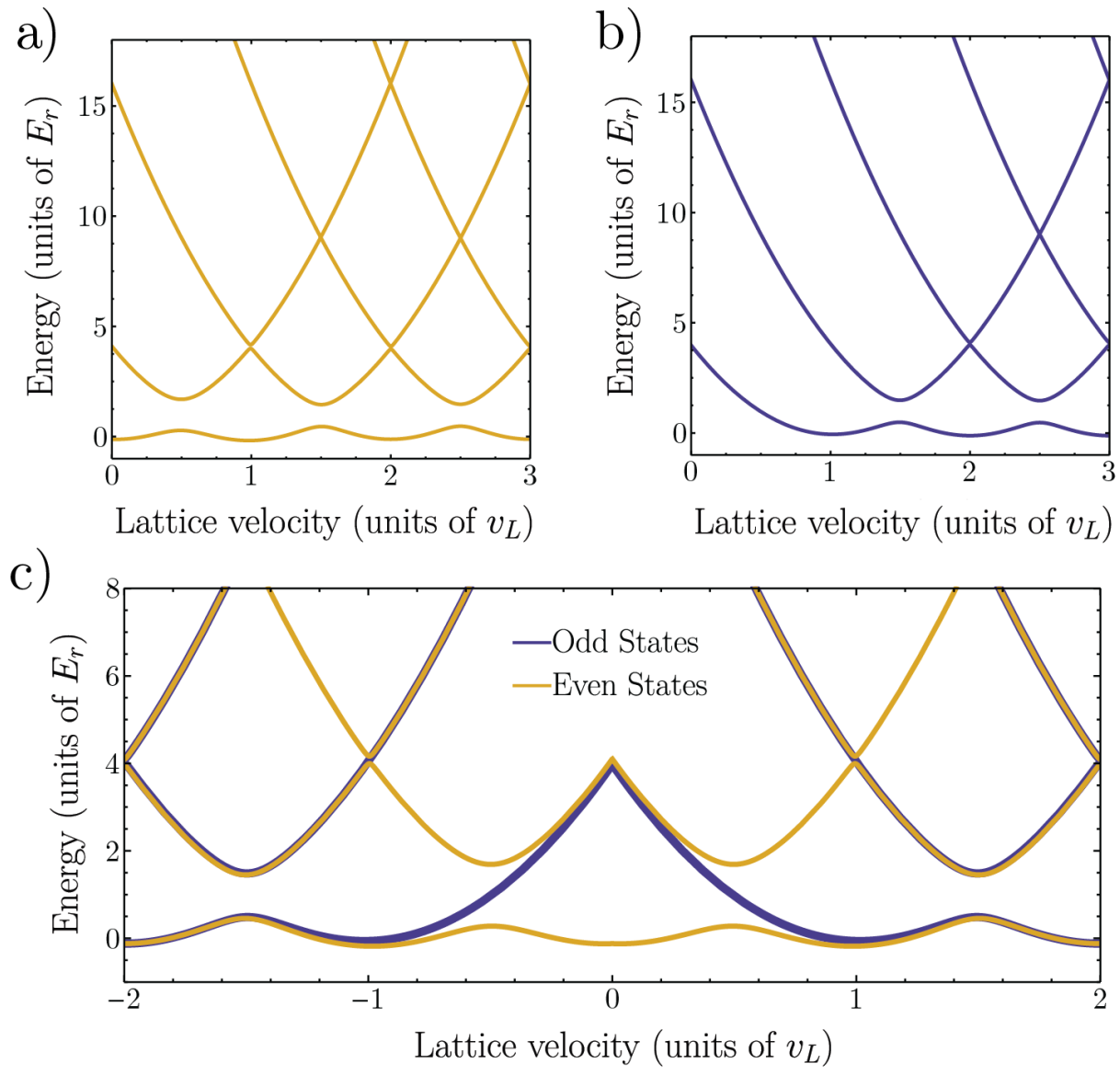

Figure 5.3: Energy band structures of the reduced Hamiltonian (5.5) as a function of the lattice velocity, using a lattice depth $U_0 = 1E_r$. The lattice velocity is defined as $v_L = rt$, such that the two lattices at time t have velocities $\pm v_L$. a) Even-parity and b) Odd-parity energy eigenvalues starting from velocity degeneracy. c) Combined band structure as lattices are ramped through velocity degeneracy.

where we define the recoil energy $E_r = \hbar\omega_r$. The RWA is therefore valid in the limit as $r \to 0$. See Section 5.4.3 for a full derivation of this condition.

The validity of the RWA can be further studied with numerical simulation. By solving for the evolution of $|\psi(t)\rangle$ from the Hamiltonian in Eq. (5.4), the full state evolution is captured without using the RWA. We numerically integrate the Schrödinger equation with the Hamiltonian Eq. (5.2). The initial condition is a free particle (plane-wave) momentum state which is adiabatically loaded into the lattice; the modulation frequency is then ramped to its final value, and finally the lattice is adiabatically unloaded. This state evolution can then be compared with the eigenstates of the Hamiltonian in Eq. (5.5) after the RWA. Fig. 5.4a) shows the probability amplitude in the ground state of Eq. (5.5) during the frequency ramping, defined as $P_0(t) = |\langle +_{gs}(t)|\psi(t)\rangle|^2$. The state $|+_{gs}(t)\rangle$ denotes the even-parity ground state of Hamiltonian (5.5) as a function of time. Fig. 5.4a) shows that the true state evolution is nearly identical to that of the ground state of the Hamiltonian in Eq. (5.5), which generally holds true when Eq. (5.6) is satisfied.

To stress the parallel between SLBO and DLBO, we also plot the probability amplitude in the ground state for SLBO using eigenstates calculated from the Hamiltonian in Eq. (5.10) in Section 5.4.1. In both SLBO and DLBO, the states pass avoided level crossings at times $t = (a+1/2)T_B$ for integer a, where there is mixing with the second band as well as Landau–Zener tunneling losses, which are discussed in Sec. 5.2.3. The dual-lattice simulation doesn't project perfectly onto the ground eigenstate around time $t = 0$ due to the perturbation terms dropped in the RWA.

5.2.3 Limits on ramp rate from Landau–Zener tunneling and higher-order transitions

Non-adiabatic Landau–Zener losses arise from the level crossings in Fig. 5.3 between the first and second even-parity energy bands. For SLBO with weak lattices and slow ramp rates, the survival probability per Bloch oscillation is given by $P_{LZ} = 1 - e^{-2\pi\Gamma_1}$ where $\Gamma_1 = U_0^2/(4\hbar^2 r)$ is the Landau–Zener parameter [167, 168]. For ramp rates $r < \omega_r^2$, this formula also describes losses from all level crossings of the DLBO Hamiltonian, Eq. (5.5), except for the two level-crossings at $t = \pm T_B/2$. These two crossings between even-parity eigenstates have an energy gap that is increased by a factor of $\sqrt{2}$, as derived in Section 5.4.2. The Landau–Zener parameter Γ_2 for these two crossings is therefore given by $\Gamma_2 = U_0^2/2\hbar^2 r$. All subsequent crossings in DLBO have the same energy gap as SLBO and are described by the same tunneling parameter Γ_1. The dual-lattice beamsplitter is therefore more robust to Landau–Zener losses at the first level crossing than SLBO at a fixed lattice depth U_0, as shown in Fig. 5.4a).

Fig. 5.4b) shows the simulated efficiency of a single Bloch oscillation at a constant Landau–Zener parameter for both the SLBO and DLBO Hamiltonians in Eq. (5.2) and (5.7) respectively. The efficiency is defined as the total population in the desired final momentum states relative to the initial population. In order to have the same expected Landau–Zener

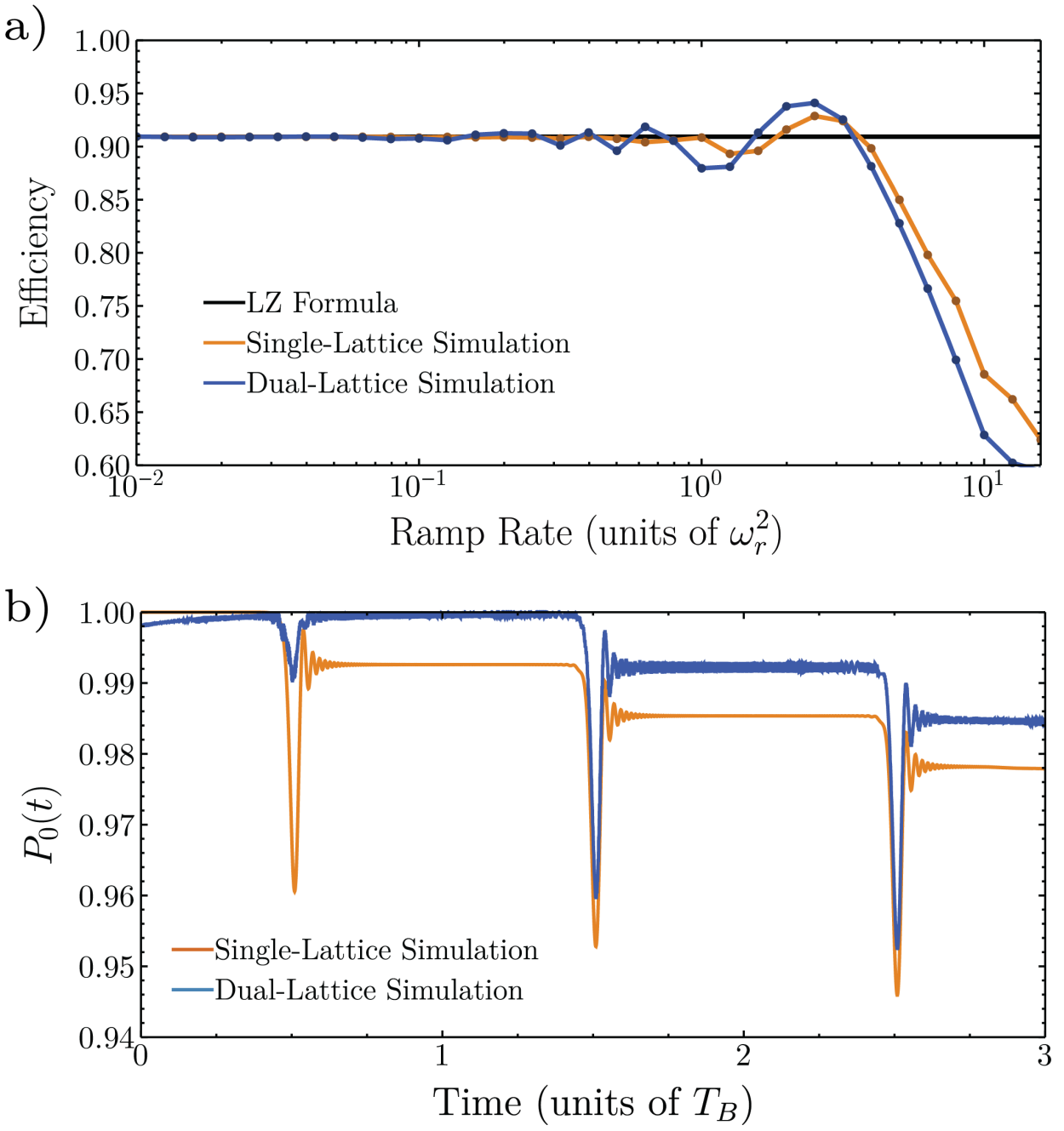

Figure 5.4: Comparison of single-lattice and dual-lattice Bloch oscillations. a) Probability amplitude in the ground state over three Bloch periods. A lattice depth of $U_0 = 0.5E_r$ and ramp rate $r = 0.02\omega_r^2$ are used for both simulations. The lattice depth is intentionally chosen to be low in order to illustrate loss mechanisms for SLBO in comparison with DLBO. See text for discussion. b) Simulation of efficiencies after one level crossing. For each ramp rate, the lattice depth is chosen to keep the Landau–Zener (LZ) parameters constant at $\Gamma_1 = \Gamma_2 = 0.3$ such that the expected losses from the LZ formula are constant. The atom begins in the ground state at time $t = 0$ with $\omega_m(t = 0) = 0$ and $\phi_0 = 0$.

losses for both simulations, the SLBO lattice depth is increased by a factor of $\sqrt{2}$ for each ramp rate compared to the DLBO simulation such that $\Gamma_1 = \Gamma_2 = 0.3$. There is asymptotic agreement with the Landau–Zener formula for ramp rates $r \ll \omega_r^2$ for both single-lattice and dual-lattice level crossings, as well as additional oscillatory behavior of the DLBO efficiency compared to the SLBO efficiency owing to the oscillatory terms dropped in the RWA.

The rotating terms being dropped in the RWA can also contribute to higher-order processes that couple amplitude from the ground band to higher energy bands, and are further discussed in Section 5.4.4. The dominant loss channel is a third-order transition that couples the first and second energy levels around time $t = T_B/6$. These higher-order losses place a lower limit on the ramp rate for a fixed lattice depth, below which losses from the ground band begin to be appreciable.

5.2.4 Comparison of limits on the ramp rate

The RWA condition in Eq. (5.6) and Landau–Zener tunneling losses both place an upper limit on the ramp rate. For Landau–Zener losses, efficient dynamics require $r \ll (\pi/2)U_0^2\hbar^2$; when $U_0 \lesssim \sqrt{2}E_r$, the RWA condition in Eq. (5.15) is automatically satisfied if the lattice depth is large enough to sufficiently suppress Landau–Zener tunneling. The RWA that leads to the Hamiltonian (5.5) is therefore asymptotically correct in the limit $r \to 0$ provided that $\hbar\sqrt{r} \ll U_0 \lesssim \sqrt{2}E_r$. On the other hand, when $U_0 \gtrsim \sqrt{2}E_r$, both the RWA condition and the standard Landau–Zener criterion begin to fail because the time windows for successive transitions begin to overlap non-negligibly.

Higher-order losses place a lower limit on the ramp rate, and for $r \leq \omega_r^2$, this limit and the upper limits on the ramp rate from Landau–Zener losses and the RWA condition can all easily be satisfied. Because of the non-linear scaling of these different limits on the ramp rate, the maximum possible efficiency of the processes quickly approaches 1 as $r \to 0$; for $r = 0.5\omega_r^2$, the maximum efficiency of the initial $4\hbar k$ momentum splitting in a Bloch beamsplitter is already $> 99\%$.

Fig. 5.5 illustrates beamsplitter losses as a function of the ramp rate r and the lattice depth U_0. Losses towards the top-left of the plot correspond to Landau–Zener tunneling losses, and losses towards the bottom-right correspond to higher-order transitions. Moving towards higher lattice depths and ramp rates, the maximum efficiency of the beamsplitter decreases because of the competing loss mechanisms.

The two loss channels result in non-zero wavefunction amplitude in momentum states different from the target states, and these additional momentum states could contribute to parasistic interferometers. This analysis is beyond the scope of the chapter, however we note that there exist methods to reduce the effects of parasitic interferometers [169].

5.2.5 Crossing through velocity degeneracy

In addition to a beamsplitter, one can also ramp the two lattices through velocity degeneracy to create atom mirrors and combiners. This process has previously been attempted

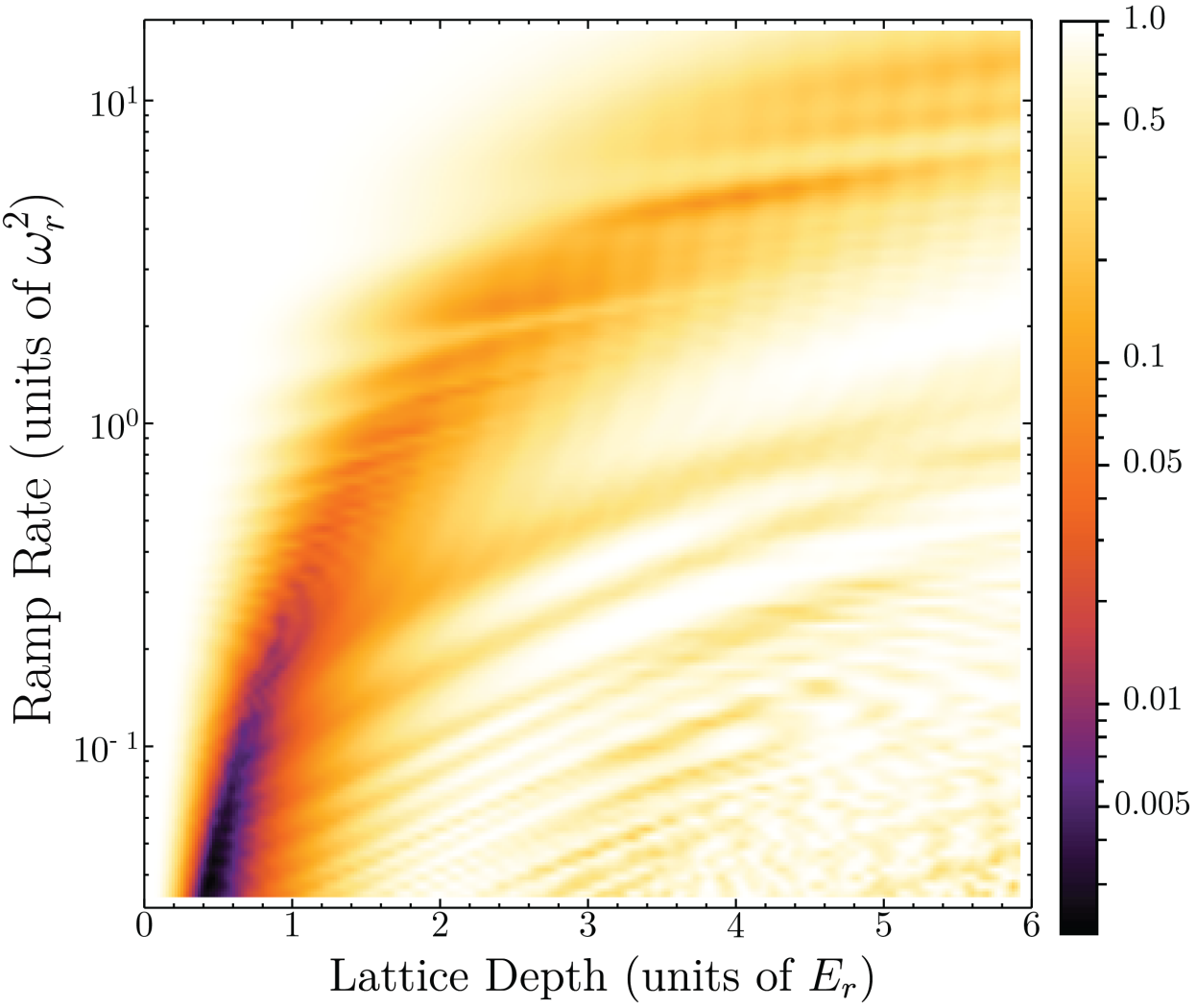

Figure 5.5: Numerical simulation of beamsplitter losses showing the dependence on the two most important parameters in the Hamiltonian: frequency ramp rate and lattice depth. Darker color corresponds to lower losses, or higher efficiency. The simulation includes adiabatic loading of lattice, frequency ramping for four Bloch periods, and adiabatic unload, such that the final momentum splitting is $16\hbar k$. Efficiency is defined as the probability amplitude on the desired momentum states after unloading the lattice. See text for discussion of loss mechanisms.

experimentally [170], but the dynamics were seen to be inefficient and uncontrolled because the ramp rate, lattice depth, and relative phase between lattices were not optimized. The intuition for the dynamics through a level crossing are described below, and for a more mathematical treatment see Section 5.4.5.

Consider two optical lattices with velocities that are initially far apart. One arm of an interferometer that is initially comoving with one of the two lattices can be understood as a superposition of an even-parity and an odd-parity ground state. Relative phase shifts between the even and odd states causes amplitudes to add constructively or destructively for positive or negative momentum states, which means that a controlled relative phase shift between the even- and odd-parity states can be used to control the momentum distribution of the atomic state after crossing through velocity degeneracy.

Figure 5.3c shows the band structure as the lattices are ramped through velocity degeneracy at time $t = 0$. Far from velocity degeneracy, the even and odd ground state energy bands overlap and have the same level crossing structure. Near time $t = 0$, however, these energy bands deviate because, by definition, an odd-parity state in momentum space cannot have amplitude on the zero-momentum basis state $|0\rangle$. As a result, when crossing through velocity degeneracy the odd-parity ground state has no level crossing coupling momentum into or out of the zero momentum state, so the even parity ground state passes through two additional level crossings at times $t = \pm T_B/2$ compared to the odd parity ground state.

Through the coherent interactions with photons from each of the lattices, the relative phase ϕ_0 of the two optical lattices is ultimately added to amplitude in the even-parity state, but not the odd-parity state. As a result, the offset phase ϕ_0 can coherently control the population in the two lattices after a degeneracy crossing. This allows one to create reflection or recombination pulses in an interferometer, and together with the beamsplitter process described previously, this comprises a full set of atom-optics tools for atom interferometry (see Fig. 5.6 for experimental implementation, and the paper this chapter is based on, Ref. [25], for full details).

5.2.6 Experimental considerations

The dynamics of symmetric Bloch oscillations are sensitive to the initial velocity distribution of an atom. Efficient beamsplitter dynamics are observed for atoms with velocity spreads of more than $\sigma_v = 0.5v_r$, where σ_v is the standard deviation in velocity of a Heisenberg-limited Gaussian wavepacket. However, this spatial separation does not necessarily result in a superposition state in momentum space. For matter wave sources where different velocity classes are uncorrelated, only amplitude within a certain momentum window Δp results in a superposition state, and amplitude to the left (right) of this window in momentum space will preferentially follow the right-moving (left-moving) lattice [157]. Intuitively, this can be understood by considering the dynamics in the Brillouin zone. When an atom begins at zero velocity, symmetric Bloch oscillations apply a force in both directions, and the quasimomentum can be thought of as being ramped in both directions simultaneously such that the state reaches both edges of the Brillouin zone at the same time, splitting the atom symmetrically

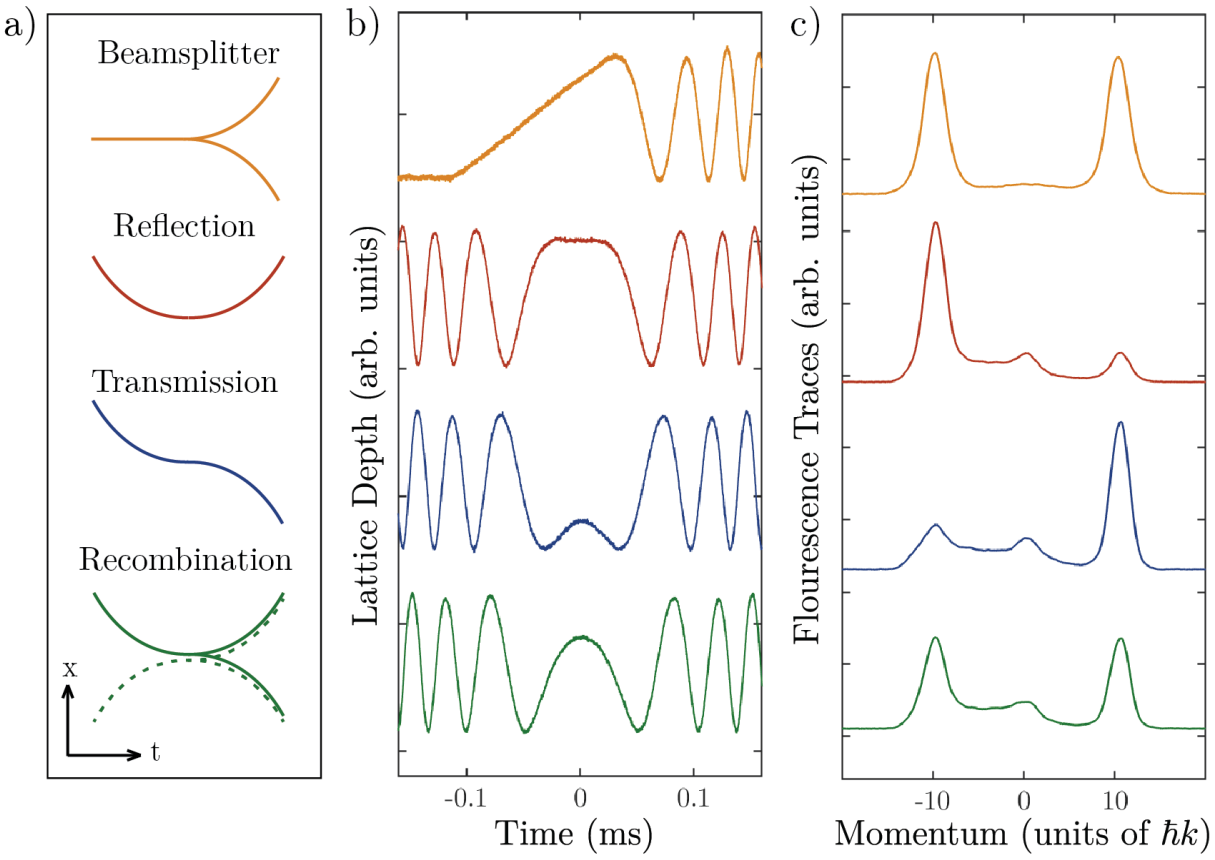

Figure 5.6: Experimental realization of a Bloch beamsplitter (yellow), reflection (red), transmission (blue), and recombination (green) as lattices are ramped through velocity degeneracy. a) Space-time trajectories. b) Intensity profiles of the $\omega_2 \pm \omega_m(t)$ interferometry beams, which are measured by imaging the laser beams on a photodiode just before entering the vacuum chamber. The profiles show beats between the two frequencies, which is the temporal part of the potential in the Hamiltonian (5.1). Time $t = 0$ indicates when $\omega_m = 0$. Different phase offsets ϕ_0 result in different beat profiles on the beam. c) Fluorescence traces of atoms from time-of-flight imaging showing the resulting distribution after various operations.

in a superposition state. If the atom has some initial velocity, however, it will reach one edge of the Brillouin zone before the other, and as a result amplitude will preferentially be driven by this first transition.

Numerical integration of the Hamiltonian (5.1) can be used to solve for evolution of a wavefunction $\psi(x,t)$ with arbitrary initial conditions (see Fig. 5.1) using the Crank–Nicolson method to discretize the Schrödinger Equation [171, 172]. These simulations confirm that faster ramp rates result in higher fidelity superposition states in momentum states, which in turn results in higher contrast interferometers.

Diffraction phases are fundamental to any asymmetric Bragg diffraction beamsplitter [173, 174], and must be accounted for in precision measurements [144]. For symmetric Bloch oscillations, if the center of the initial atomic velocity distribution is non-zero, the initial state has some projection onto the odd-parity eigenstates which leads to asymmmetry and diffraction phases. The symmetry of the Bloch beamsplitter (see Fig. 5.1) ensures that there is no diffraction phase that is fundamental to the technique. An initial velocity of the atoms, however, breaks the symmetry and creates a diffraction phase between interferometer arms. The numerical study discussed in Section 5.4.6 shows that there are "magic" lattice depths where the diffraction phase vanishes. For realistic experimental control over the stability of the lattice depth, the diffraction phase can be limited to $\pm 10\,\mathrm{mRad}$, independent of the momentum splitting. Increasing the momentum splitting will therefore fractionally suppress the diffraction phase, and diffraction phases can also be measured directly by varying the time between pulses in an interferometer. Note also that an ensemble of atoms with different center velocities will result in phase spreading in an interferometer.

The analytic results derived for Landau–Zener tunneling and the rotating wave approximation only apply to slow ramp rates that satisfy the condition in Eq. (5.6). Experimentally, we use larger ramp rates of up to $r = 10\omega_r^2$ and lattice depths around $8E_r$ in order to maximize interferometer contrast, which is a region of parameter space that breaks the assumptions used to derive this inequality. Although the analytical efficiency predictions break down in this regime, we still observe reasonably efficient dynamics both numerically and experimentally. In fact, the velocity bandwidth of the beamsplitter is larger at faster ramp rates which results in higher contrast interferometers. See Fig. 5.5 for an illustration of a beamsplitter for different values of lattice depth and ramp rate. Notably, even in regions of parameter space outside where the RWA is valid, one can still achieve relatively low loss beampslitters.

5.3 Conclusions and Outlook

We have developed new techniques for coherently controlling superpositions of momentum states by generalizing Bloch oscillations to two independently accelerated optical lattices. First, the Hamiltonian was treated analytically, and it was shown that the dynamics can produce efficient and coherent atom optics elements, even when the lattices pass through velocity degeneracy. For slow ramp rates, the process is adiabatic and atoms can adiabatically

follow the even-parity ground state of Hamiltonian (5.5). When ramping lattices through velocity degeneracy, the populations in the two lattices can be controlled by changing the relative phase of the two optical lattices, allowing for all atom-optics elements required to form an interferometer. Using only accelerated lattices, we create LMT interferometers with high contrast, and we showed that the resulting dynamics were first-order coherent using a differential measurement.

Compared to existing atom optics techniques [158, 160, 175], DLBO offer a number of advantages. Applications with constraints on laser power and free-fall distance, such as space-based interferometry [176, 177] or portable gravimeters [153], can use these techniques to maximize momentum transfer and thus sensitivity. Being based on adiabatic processes, these methods are robust to fluctuations in experimental parameters like lattice depth or laser frequency [165]. Symmetric Bloch oscillations are more robust to small laser intensity variations than Bragg diffraction beam splitters, and can eliminate systematic phase shifts known as diffraction phases [174, 178, 179]. Moreover, large momentum transfer can be obtained with modest laser power, whereas in multi-photon Bragg diffraction the required laser intensity scales proportional to n^2 or even n^4, if scattering losses are to be kept constant [180]. In contrast, the laser power required for DLBO is independent of the momentum splitting, relaxing the laser power requirements in an experiment. Compared to combinations of Bragg diffraction and Bloch oscillations [158, 159], DLBO requires less laser power and can achieve higher efficiencies. For example, two sequential $4\hbar k$ double-Bragg beamsplitters used in reference [160] use a peak lattice depth of $3 - 4E_r$ and achieve a total efficiency around 90%, and higher-order double Bragg pulses require considerably more laser power. In contrast, the $60\hbar k$ beamsplitter in Fig. 5.1b uses a lattice depth of $1.5E_r$ while achieving an efficiency greater than 90%.

A generalization of these dual-lattice techniques shows promise for new measurements of the fine-structure constant α. A set of realistic experimental parameters are outlined in Section 5.4.8, where we show that 10^8 radians of phase are attainable. This paves the way for a measurement of alpha at the 10^{-11} level, an order of magnitude improvement on existing measurements. Another generalization of the Bloch beamsplitter uses a multi-photon, $4n\hbar k$ transition to open the interferometer where $n > 1$. Our numerical simulations show that this multi-photon process also leads to an efficient beamsplitter for appropriate ramp rates and lattice depths, see Section 5.4.4 for further discussion.

5.4 Supplemental Information

5.4.1 Unitary transformation for single-lattice Bloch Hamiltonian

In an inertial frame initially comoving with the atoms, the SLBO Hamiltonian can be written as:

$$H = \sum_{l=-\infty}^{\infty} \left(\frac{(2l\hbar k)^2}{2m} |l\rangle\langle l| + U_0 e^{i\left(\frac{rt^2}{2}+\phi_0\right)} \left(|l\rangle\langle l+1| + |l\rangle\langle l-1|\right) \right) \tag{5.7}$$

The Hamiltonian, Eq. (5.10), is derived by transforming this Hamiltonian, Eq. (5.7), into a rotating frame that puts the time dependence of the rotating terms into the diagonal. This is achieved with the following unitary:

$$U = \sum_{l=-\infty}^{\infty} e^{i\frac{d(t)\hat{p}}{\hbar}} e^{i\frac{\theta(t)}{\hbar}} |l\rangle\langle l| \tag{5.8}$$

$$= \sum_{l=-\infty}^{\infty} e^{il\left(\frac{rt^2}{2}+\phi_0\right)} e^{i\frac{ma^2t^3}{6\hbar}} |l\rangle\langle l| \tag{5.9}$$

with $d(t) \equiv at^2/2 + \phi_0/k$ and $\theta(t) \equiv ma^2t^3/6$. This same transformation is used in reference [181], and it is almost identical to the transformation used in Eq. (5.3), except there is no longer a absolute value sign on the momentum operator. Acting on the Hamiltonian, Eq. (5.7), with the unitary transformation in Eq. (5.8) results in H_{SLBO}:

$$H_{\text{SLBO}} = \sum_{l=-\infty}^{\infty} \frac{(2l\hbar k - Ft)^2}{2m} |l\rangle\langle l| + \frac{U_0}{2} \left(|l\rangle\langle l+1| + |l\rangle\langle l-1|\right) \tag{5.10}$$

The Ft term that appears in the kinetic energy is related to the quasimomentum k_q through the relation $\hbar k_q = Ft$.

5.4.2 Symmetrized Hamiltonian

The Hamiltonian in Eq. (5.5) can be explicitly symmetrized by applying a rotation to the basis states. This is achieved by rotating to new basis states that are symmetric and antisymmetric combinations of the free-space momentum basis states, namely we will have (unnormalized) even parity basis states $|+_l\rangle = |l\rangle + |-l\rangle$ and odd parity states $|-_l\rangle = |l\rangle - |-l\rangle$. The zero momentum state remains unchanged under this rotation, as it is already an even-parity state. The following rotation matrix achieves this transformation:

$$R = |0\rangle\langle 0| + \sum_{l>0} \frac{1}{\sqrt{2}} \left(|l\rangle\langle l| + |-l\rangle\langle -l|\right) + \frac{1}{\sqrt{2}} \left(|l\rangle\langle -l| - |-l\rangle\langle l|\right) \tag{5.11}$$

The Hamiltonian (5.5) can then be rotated to the symmetric Hamiltonian $H_{\text{sym}} = R\,H_{\text{DLBO}}\,R^T$ to arrive at the following:

$$\begin{aligned} H_{\text{sym}} =& \frac{(Ft)^2}{2m}\,|0\rangle\langle 0| + \sum_{l>1}\Bigg(\frac{(2|l|\hbar k - Ft)^2}{2m}\,(|+_l\rangle\langle +_l| + |-_l\rangle\langle -_l|) \\ &+ \frac{U_0}{2}\Big(\,|+_l\rangle\big(\,\langle +_{l+1}| + \langle +_{l-1}|\,\big) + |-_l\rangle\big(\,\langle -_{l+1}| + \langle -_{l-1}|\,\big)\Big)\Bigg) \\ &+ \frac{U_0}{2}\,(|+_1\rangle\langle +_2| + |-_1\rangle\langle -_2|) + \frac{U_0}{\sqrt{2}}\,(|0\rangle\langle +_1| + |+_1\rangle\langle 0|) \end{aligned} \tag{5.12}$$

In this rotated basis, there is no coupling between $|0\rangle$ and $|-_1\rangle$, so we can explicitly see why the odd-parity states have no level crossing at times $t = \pm T_B/2$ in Fig. 5.3c). Moreover, the coupling between $|0\rangle$ and $|+_1\rangle$ is $\sqrt{2}$ larger than any of the other couplings, resulting in suppressed Landau–Zener tunneling from the level-crossings of the even-parity ground state at times $t = \pm T_B/2$ in Fig. 5.3c).

5.4.3 Rotating wave approximation condition

To make the rotating wave approximation (RWA) in Eq. (5.4), we average the oscillating term e^{irt^2} over the duration of the transition between momentum states. This term is oscillating most slowly around the first level crossing between the first and second even bands at time $t = T_B/2$. In the limit of small lattice depths $U_0 \ll 4E_r$, the energy gap $E_g(t)$ near this level crossing is given by

$$E_g(t) = \sqrt{\hbar^2 r^2 (t - T_B/2)^2 + 2U_0^2} \quad , \tag{5.13}$$

such that the center of the level crossing occurs at time $t = T_B/2$, and the duration of the level crossing is $\Delta t = 2\sqrt{2}U_0/\hbar r$.

Taking the time average of the rotating term e^{irt^2} over the duration of the level crossing gives the following:

$$\langle e^{irt^2}\rangle \approx -\frac{i\hbar^2 r}{4U_0} e^{i\alpha} \frac{U_0\cos\beta - 2\sqrt{2}iE_r\sin\beta}{8E_r^2 - U_0^2} \tag{5.14}$$

where we define $\alpha = 2(8E_r^2 + U_0^2)/(\hbar^2 r)$ and $\beta = 8\sqrt{2}E_r U_0/(\hbar^2 r)$, and we have assumed that $r \ll 2(2\sqrt{2}E_r - U_0)^2/\hbar^2$. The rotating term can be dropped so long as this average is small compared to 1, i.e., when

$$|\langle e^{irt^2}\rangle| < \frac{\hbar^2 r}{4U_0(2\sqrt{2}E_r - U_0)} \ll 1 \tag{5.15}$$

or equivalently, $r \ll 4U_0(2\sqrt{2}E_r - U_0)/\hbar^2$. We note that varying the time window of integration in Eq. (5.14) changes the numerical factors in Eq. (5.15), but not the limiting behavior as $r \to 0$.

5.4.4 Higher-order loss mechanisms

When the lattice depth is too large, the oscillating terms dropped in the rotating wave approximation from the Hamiltonian in Eq. (5.4) can contribute to higher-order parasitic transitions. The dominant loss mechanism at ramp rates $r \ll \omega_r^2$ is a third-order (six-photon) process coupling the states $|0\rangle$ and $|+_1\rangle$ around time $t = T_B/6$, where $|+_l\rangle$ refers to the symmetrized basis states derived in Section 5.4.2. There are two possible energy and momentum conserving pathways for the transition to occur; $|0\rangle \to |+_1\rangle \to |0\rangle \to |+_1\rangle$ and $|0\rangle \to |+_1\rangle \to |+_2\rangle \to |+_1\rangle$. For lattice depths much less than the spacing between energy levels, $U_0/2 \ll 4E_r$, the effective coupling between these states scales like $(U_0/2)^3/(4E_r)^2$, which is the same scaling as the Rabi frequency in higher-order Bragg diffraction [180, 182].

During a Bloch beamsplitter, the laser frequencies are swept across this parasitic resonance, as seen in Fig. 5.7a, which can be thought of as a parasitic level-crossing between $|0\rangle$ and $|+_1\rangle$; for an efficient Bloch beamsplitter, amplitude should remain in $|0\rangle$ by tunneling through this level-crossing diabatically. To first order, the adiabatic population transfer to the state $|+_1\rangle$ during this level crossing is given by $P_{LZ} = 1 - e^{-2\pi\Gamma} \approx 2\pi\Gamma$ when the Landau–Zener parameter Γ is close to zero. For $U_0 \ll 8E_r$ and $r \ll \omega_r^2$, we therefore expect losses from the Bloch beamsplitter $P_{\text{loss}} = 2\pi\Gamma_3 \propto (\omega_r^2/r)\,(U_0/8E_r)^6$ where $\Gamma_3 \propto (\omega_r^2/r)\,(U_0/8E_r)^6$. This scaling of the higher-order losses in the limit of $r \to 0$ agrees with our numerical simulations.

In addition to the third-order process discussed above, there are an infinite number of these higher-order processes that conserve energy and momentum, but the transition rates are highly suppressed at lower lattice depths. Fig. 5.7b show the result of a simulation with an increased lattice depth, to a regime in which many of these higher-order transitions can couple amplitude to higher-excited states. The parameters chosen for this simulation happen to drive five of these higher-order transitions within the first Bloch period. A ramp rate $r \ll \omega_r^2$ is chosen for the simulation so that the transitions are well-resolved. In contrast, Fig. 5.4a) illustrates negligible higher-order losses because all higher-order transitions are highly suppressed at lower lattice depths.

5.4.5 Crossing through velocity degeneracy

The dynamics while crossing through velocity degeneracy are determined by studying the eigenstates of the DLBO Hamiltonian, Eq. (5.5). An initial momentum state $|n\rangle$, where $n > 0$, can be decomposed as

$$|n\rangle = \frac{1}{\sqrt{2}}(|+_n\rangle + |-_n\rangle) \tag{5.16}$$

where are the symmetric and antisymmetric combinations of the free-space momentum basis states $|\pm n\rangle$ as derived in Section 5.4.2. Similarly, $|-n\rangle$ can be decomposed as

$$|-n\rangle = \frac{1}{\sqrt{2}}(|+_n\rangle - |-_n\rangle) \tag{5.17}$$

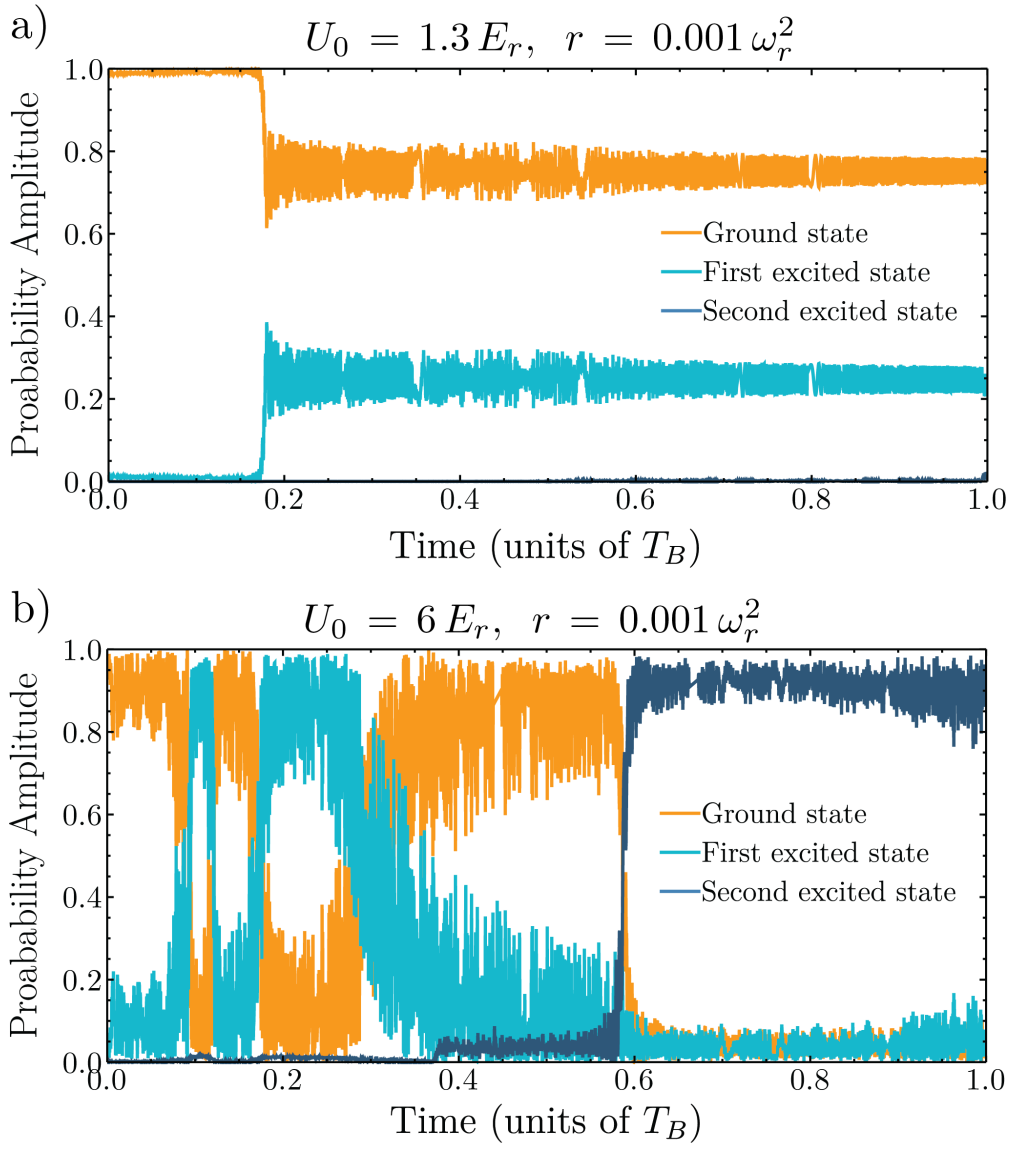

Figure 5.7: Simulations of one Bloch period of a Bloch beamsplitter illustrating losses from the ground band due to higher-order transitions. The states used for determining the probability amplitude are even-parity eigenstates of Hamiltonian (5.5). A slow ramp rate is used so that the various transitions are resolved from one another. a) The first losses to occur are due to a third-order transition coupling the ground state and first excited state. b) A much larger lattice depth shows a number of different higher-order transitions. Before time $t = T_B/2$ there are four separate higher-order resonances between the ground state and first excited state that transfer population between the levels. Around time $t = 0.6\,T_B$ there is a transition between the ground state and the second excited state.

Without loss of generality, we restrict our attention to one arm of an interferometer with momentum $|n\rangle$. Then when one of the two lattices is initially comoving with the state $|n\rangle$, this state will be loaded into the ground state of the DLBO Hamiltonian in Eq. (5.5) as a superposition of odd-parity and even-parity ground states according to Eq. (5.16).

Crucially, relative phase shifts between the even- and odd-parity eigenstates cause amplitude to add constructively or destructively for the positive momentum or negative momentum states; for example, if the state $|-_n\rangle$ acquires a π phase shift relative to the state $|+_n\rangle$, then the state $|n\rangle$ in Eq. (5.16) will transform the the state $|-_n\rangle$ in Eq. (5.17). There are two sources of relative phase shifts between the even- and odd-parity states as the lattices are swept through velocity degeneracy. First, since these states are energy eigenstates of the Hamiltonian, there is a dynamical phase difference ϕ_d between the two states given by $\phi_d = (1/\hbar)\int dt'(E_-(t') - E_+(t'))$, where $E_\pm$ denotes the energy of the even- and odd-parity ground states over time, as shown in Fig. 5.3c. Since the even- and odd- parity states have different level structure near the degeneracy crossing, this gives a non-trivial phase shift. In addition, there are two additional level crossings for the even state near velocity degeneracy compared to the odd-parity state, as discussed in Sec. 5.4.2. These level crossings correspond to transferring photons to and from the laser field, so the phase of the laser field is imparted to the atomic state during these crossings.

Laser phase is a well known source of phase in atom interferometers, and is the primary phase contribution for certain interferometer configurations such as Mach–Zehnder interferometers [183]. In a single optical lattice, laser phase arises when the position of the laser standing wave shifts position with respect to the atom, resulting in a phase shift $\Delta\phi = 2k\Delta x$. In the case of two optical lattices, there is an additional degree of freedom, namely the relative position of the two lattices. This changes the offset phase ϕ_0 in Eq. (5.1), and it is reasonable to expect this phase term to play a coherent role in the dynamics.

There are two ways to understand the laser phase effects, mathematically and physically. Mathematically, one can see that the even-parity state is shifted relative to the odd-parity state from the definition of the unitary transformation in Eq. (5.3). As mentioned previously, the sign on $d(t)$ in Eq. (5.3) is changed at time $t = 0$, which changes the phase offset on every basis state except for the zero momentum state $|0\rangle$. Just before time $t = 0$, the odd-parity ground state is approximately given by $|-_{gs}\rangle = (e^{-i\phi_0}|1\rangle - e^{-i\phi_0}|-1\rangle)/\sqrt{2} = e^{-i\phi_0}|-_1\rangle$, whereas after time $t = 0$ the state becomes $|-_{gs}\rangle = (e^{i\phi_0}|1\rangle - e^{i\phi_0}|-1\rangle)/\sqrt{2} = e^{i\phi_0}|-_1\rangle$. The odd state is therefore phase shifted by $2\phi_0$. Since the state $|0\rangle$ is unchanged, the even- and odd-parity states see a relative phase shift of $2\phi_0$. Physically, the nature of the degeneracy crossing is a result of constructive or destructive interference between amplitudes. Since there are two additional level crossings of the even state compared to the odd state, the even state receives a laser phase shift $\phi_l = 2\phi_0$. At time $t = T_B$, after the two additional crossings, both the even- and odd-parity states are mostly superpositions of the states $|\pm l\rangle$, but the extra phase shift of the even state results in coherent interference and changes the resulting output state. This phase shift can also be observed in our numerical simulations, where the even-parity state is phase shifted by ϕ_0 at each of the two level crossings near velocity degeneracy.

Up to a global phase, the new state after the degeneracy crossing can be written as:

$$|\psi_f\rangle = \frac{1}{\sqrt{2}}(e^{i(\phi_d+\phi_l)}|+_n\rangle + |-_n\rangle) \tag{5.18}$$

By controlling the phase shifts ϕ_d and ϕ_l in an experiment, one has control over the output nature of the degeneracy crossing. For example, arranging for $\phi_d + \phi_l = 2m\pi$ for some integer m ensures that the state after the crossing will be identical to the state before the crossing, which corresponds to transmission through the crossing. For $\phi_d + \phi_l = (2m+1)\pi$ for some integer m, the output state becomes $-|+_n\rangle + |-_n\rangle = |-n\rangle$, which has opposite momentum compared to the input state $|n\rangle$ and corresponds to a reflection. Intermediate values of the phase can be used to split amplitude between the two momentum states $|\pm n\rangle$. In practice, it is easiest to change ϕ_0, and therefore ϕ_l, since this phase is directly controllable experimentally. Our simulations show that ϕ_d also depends on ϕ_0 at the moment that the lattices are velocity degenerate, but this dependence does not prevent one from continuously transforming between different output behaviours by changing only ϕ_0.

The phase ϕ_d is dependent on the lattice depth, and therefore the lattice depth needs to be well controlled in order to see coherent dynamics after the zero-crossing. In the limit $U_0 = 0$, the dynamical phase ϕ_d is given by $\phi_d = 16\omega_r^2/r$, such that $\phi_d \gg 2\pi$ when $r \ll \omega_r^2$. When $U_0 > 0$, this phase term is also a function of the lattice depth; as a result, fluctuations in U_0 lead to fluctuations in ϕ_d. Similarly, variable U_0 across a finite laser beam leads to a variable ϕ_d across an atom cloud. Both of these effects result in unreliable zero-crossing behaviour at slow ramp rates, and both effects likely explain why we see the largest interferometer contrast for fast ramp rates around $r = 10\omega_r^2$.

5.4.6 Diffraction phase

Here, we consider the diffraction phase acquired from a beamsplitter, which is the phase difference between the positive and negative momentum components of the resulting wavefunction. If the atomic state initially has some free-space velocity with respect to the lattice, the momentum-parity symmetry of the problem is broken and the resulting dynamics will be asymmetric, leading to a diffraction phase.

Figures 5.8 and 5.9 show numerical simulations of the diffraction phase for a $16\hbar k$ Bloch beamsplitter. Almost all of the diffraction phase from the beamsplitter comes from the first $8\hbar k$ momentum splitting near velocity degeneracy; further increasing the momentum transfer beyond this does not further increase the dynamical phase ϕ_d. The diffraction phase for a beamsplitter scales like the square root of the initial velocity, but the prefactor in front of this scaling can be controlled by varying the lattice depth and the details of loading or unloading the lattice. The simulations in Figures 5.8 and 5.9 use a linear intensity ramp for loading an unloading over a time $t_{\text{load}} = 6\pi\omega_r^{-1}$.

Figure 5.9 shows the diffraction phase as a function of the lattice depth, and oscillations in the diffraction phase allow one to operate at a "magic" lattice depth with suppressed sensitivity to diffraction phases from missing the center velocity of the atom cloud. For

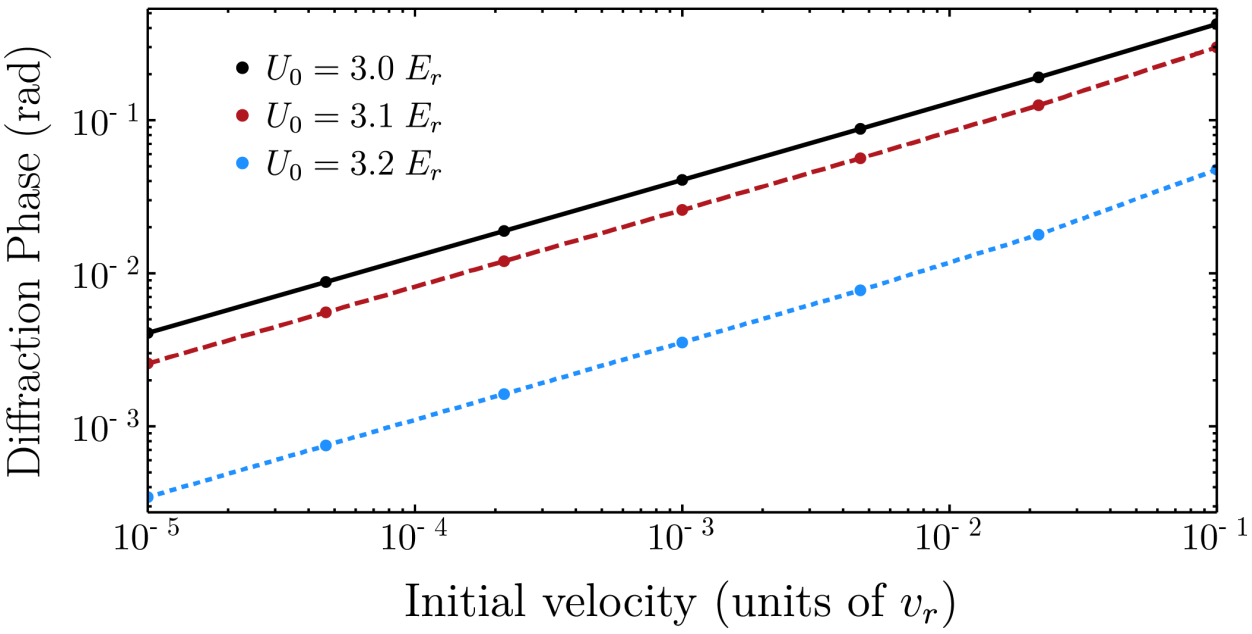

Figure 5.8: Numerical simulation of diffraction phase from a Bloch beamsplitter as a function of velocity with respect to the initial optical lattice. Simulation includes adiabatically loading the lattice, frequency ramping at a rate $r = 1.0\,\omega_r^2$ for four Bloch periods, then adiabatic unloading of the lattice. See text for further discussion.

precision measurement, such magic lattice depths could be used to significantly reduce the diffraction phases caused by fluctuations in experimental parameters. For example, a ramp rate of $r = 4\omega_r^2$ and a lattice depth around $U_0 = 5.9E_r$ gives 80% efficient beamsplitters with minimized diffraction phase sensitivity (see Figures 5.5 and 5.9). We can reasonably operate within $0.001v_r$ of the center velocity of the atom cloud, and by intensity stabilizing the lattice to 1% fluctuations, the diffraction phase can be limited to ± 10 mRad. This diffraction phase can then be measured directly by varying the duration of the interferometer, as done in reference [144].

5.4.7 Higher-order generalization of the dual-lattice methods

The transitions driven in DLBO are two-photon processes that transfer $2\hbar k$ momentum. By sweeping past multiple of these transitions in successions, LMT can be easily achieved. In contrast, higher-order transitions are also possible that transfer $2n\hbar k$ momentum in a single, multi-photon process.

It is instructive to first understand single-lattice higher-order processes before understanding the dual-lattice analogues. SLBO can be though of as adiabatically sweeping past a successions of $2\hbar k$ Bragg transitions [132]. The higher-order, multi-photon analogue has

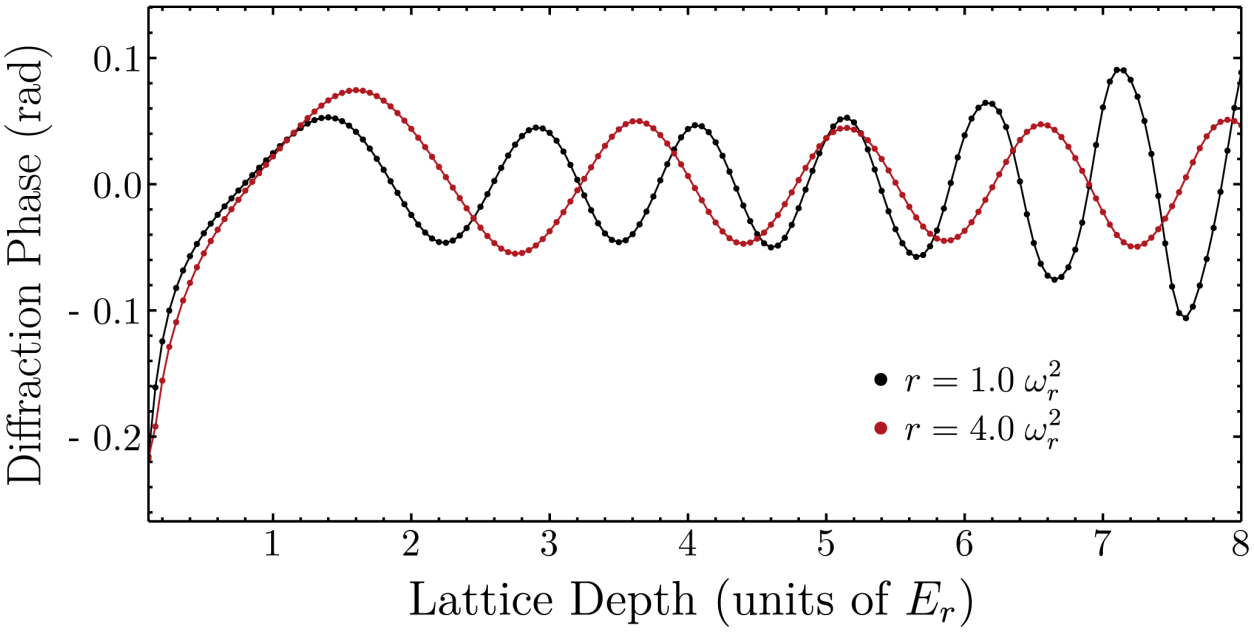

Figure 5.9: Numerical simulation of diffraction phase from a Bloch beamsplitter as a function of lattice depth for two different ramp rates, using an initial velocity with respect to the lattice of $0.001v_r$. Points are from simulation, lines are an interpolation between points to guide the eye. The zero crossings in the diffraction phase allow for one to operate an interferometer at a "magic" lattice depth to suppress sensitivity to diffraction phase. See text for further discussion.

been implemented experimentally in reference [184]. The laser is adiabatically swept across a $2n\hbar k$ Bragg resonance, which adiabatically drives a $2n$-photon process. Though not discussed directly in [184], this process can be interpreted using a Bloch band picture where atoms have an initial quasimomentum outside of the first Brillouin zone such that they are loaded into higher Bloch bands. As the lattice is accelerated, the state sweeps past a level crossing between higher Bloch bands, and successful momentum transfer requires the state to adiabatically traverse the crossing and stay in the same Bloch band.

DLBO can be thought of as adiabatically sweeping past a succession of "double Bragg" transitions [185]. A first-order double Bragg transition symmetrically drives $\pm 2\hbar k$ Bragg resonances such that the two arms are split by $4\hbar k$ momentum. One can also symmetrically drive two higher-order Bragg resonances that transfer $\pm 2n\hbar k$ momentum to obtain a $4n\hbar k$ beamsplitter, as are implemented in references [159, 160].

It is also possible to adiabatically sweep past a higher-order double Bragg transition. In terms of the modulation frequency ω_m in Eq. (5.1), these resonances occur at $\omega_m = (2m+1)\omega_r$ for integers m. A $4n\hbar k$ adiabatic dual-lattice beamsplitter can be achieved by sweeping past one of these resonances adiabatically. An experimental sequence would consist of the follow-

ing: 1) atoms are adiabatically loaded into a lattice with a modulation frequency slightly below the desired resonance, 2) the modulation frequency is swept across the resonance, and 3) the atoms are adiabatically unloaded from the lattice. It is important that the modulation frequency does not become close to other resonances during this sequence. Unlike a Bloch beamsplitter, continued ramping of ω_m after a high-order beamsplitter process will not transfer more momentum, but rather alternate between increasing and decreasing the momentum splitting between arms. The average momentum transfer per Bloch period will still be $4\hbar k$, as in the ground band.

Our simulations of this process show that it can be more efficient than a Bloch beamsplitter at a given ramp rate. However, there are two major downsides to these higher-order dual-lattice techniques. First, much more laser power is required to drive the transition; the power required to drive an n^{th}-order Bragg transition scales sharply with the order n, namely as n^2 to maintain the same Rabi frequency, and n^4 to also maintain the same single-photon scattering rate [180]. Second, continued ramping of the lattices does not continue to increase momentum splitting in any advantageous way compared to using the ground band. As a result, the first-order dual-lattice methods discussed in the main text are easier to use if the goal is to achieve very large momentum splitting without the need for significantly more laser power.

5.4.8 Application to recoil measurements

A generalization of DLBO shows promise for atom recoil measurements, and therefore in measurements of the fine-structure constant α [144]. This section is included as an example of the potential applictaions of DLBO, however we note that before such a measurement, many new systematic effects would likely need to be studied.

By removing the assumption that $\omega_1 = \omega_2$ and are independent of time in the Hamiltonian in Eq. (5.1), asymmetric lattice guided geometries can be created [131]. Additional light frequencies can also be added to the laser in order to address more than two velocity classes of atoms at the same time. Figure 5.10 shows an example interferometer configuration that would be sensitive to an atom recoil phase. The phase in the interferometer can be calculated by integrating the energy of the atoms over the various trajectories [182]. Assuming that the time to accelerate atoms is much less than the time between beamsplitter or reflection pulses, the phase of the interferometer is given by

$$\phi = 16\omega_r n_s^2 T \tag{5.19}$$

where ω_r is the recoil frequency of the matter wave, n_s is defined in Fig. 5.10, and T is the time between beamsplitter and reflection pulse in the upper (or lower) interferometer.

The following outlines a set of realistic experimental parameters that could lead to 10^8 radians of recoil phase, an order of magnitude improvement in sensitivity over the leading recoil measurement [144]. Based on the results discussed in Section III of Ref. [25], atoms in our apparatus can interact with up to 1000 photons inside an interferometer where contrast

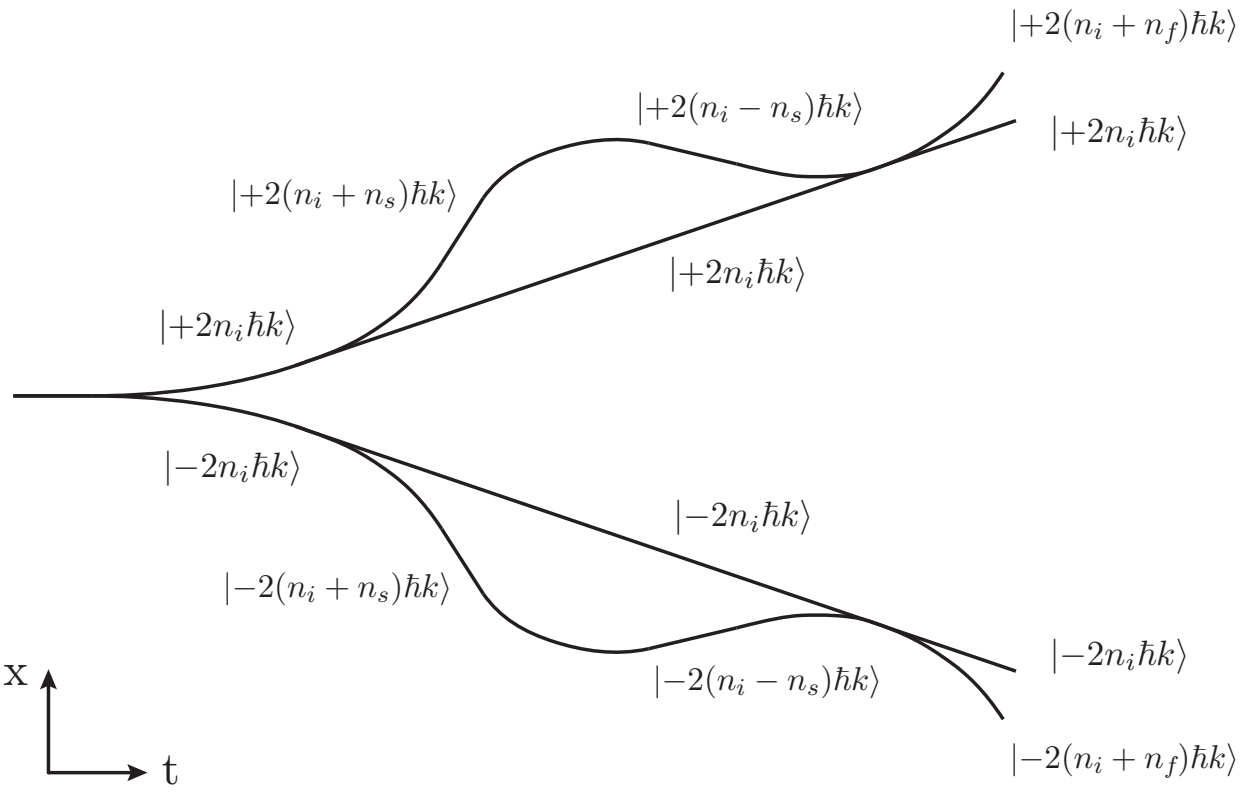

Figure 5.10: Interferometer geometry sensitive to an atomic recoil phase. The asymmetry between the two upper (lower) trajectories leads to a kinetic recoil phase acquired by the upper (lower) interferometer. The simultaneous conjugate interferometer configuration is used for a differential measurement that cancels gravitational phase to fist order, and adds the recoil phases in the upper and lower interferometers. Addressing the four velocity classes of light requires one left-moving frequency and four right-moving frequencies, similar to Fig. 5.2a).

can still be observed. Choosing $n_i = 100$, $n_s = 80$ and $n_f = 100$ (defined in Fig. 5.10) requires atoms to interact with 840 photons before closing the interferometers. For the calculation, we use a time of 80 ms between opening the interferometers and slowing the arms back to having the same velocity, the same timing used in reference [144]. Using a frequency ramp rate of $r = 250$ MHz/s, Cesium atoms can be accelerated from $|2n_i\hbar k\rangle$ to $|2(n_s + n_i)\hbar k\rangle$ in roughly 6 ms, which is much less than the time between different pulses. This ramp rate was shown to give good interferometer contrast in the main text for atoms with a vertical velocity spread of $0.05v_r$.

Bibliography

[1] Juan Maldacena, Stephen H. Shenker, and Douglas Stanford. "A bound on chaos". In: *Journal of High Energy Physics* 2016.8 (2016), p. 106. DOI: 10.1007/JHEP08(2016)106. URL: https://doi.org/10.1007/JHEP08(2016)106.

[2] Brian Swingle and John McGreevy. "Renormalization group constructions of topological quantum liquids and beyond". In: *Phys. Rev.* B93.4 (2016), p. 045127. DOI: 10.1103/PhysRevB.93.045127. arXiv: 1407.8203 [cond-mat.str-el].

[3] Stefan Rommer and Stellan Östlund. "Class of ansatz wave functions for one-dimensional spin systems and their relation to the density matrix renormalization group". In: *Phys. Rev. B* 55 (4 Jan. 1997), pp. 2164–2181. DOI: 10.1103/PhysRevB.55.2164. URL: https://link.aps.org/doi/10.1103/PhysRevB.55.2164.

[4] Ian P McCulloch. "From density-matrix renormalization group to matrix product states". In: *Journal of Statistical Mechanics: Theory and Experiment* 2007.10 (Oct. 2007), P10014–P10014. DOI: 10.1088/1742-5468/2007/10/p10014. URL: https://doi.org/10.1088%2F1742-5468%2F2007%2F10%2Fp10014.

[5] Aaron Szasz, Johannes Motruk, Michael P. Zaletel, and Joel E. Moore. *Observation of a chiral spin liquid phase of the Hubbard model on the triangular lattice: a density matrix renormalization group study*. 2018. arXiv: 1808.00463 [cond-mat.str-el].

[6] Wen Wei Ho, Soonwon Choi, Hannes Pichler, and Mikhail D. Lukin. "Periodic Orbits, Entanglement, and Quantum Many-Body Scars in Constrained Models: Matrix Product State Approach". In: *Phys. Rev. Lett.* 122 (4 Jan. 2019), p. 040603. DOI: 10.1103/PhysRevLett.122.040603. URL: https://link.aps.org/doi/10.1103/PhysRevLett.122.040603.

[7] Robert N.C. Pfeifer, Glen Evenbly, and Guifre Vidal. "Entanglement renormalization, scale invariance, and quantum criticality". In: *Phys.Rev.* A79 (2009), p. 040301. DOI: 10.1103/PhysRevA.79.040301. arXiv: 0810.0580 [cond-mat.str-el].

[8] Glen Evenbly and Guifre Vidal. "Quantum Criticality with the Multi-scale Entanglement Renormalization Ansatz". In: *Strongly Correlated Systems: Numerical Methods*. Ed. by Adolfo Avella and Ferdinando Mancini. Berlin, Heidelberg: Springer Berlin Heidelberg, 2013, pp. 99–130. ISBN: 978-3-642-35106-8. DOI: 10.1007/978-3-642-35106-8_4. URL: https://doi.org/10.1007/978-3-642-35106-8_4.

[9] G. Evenbly and G. Vidal. "Algorithms for entanglement renormalization". In: *Phys. Rev. B* 79 (14 Apr. 2009), p. 144108. DOI: 10.1103/PhysRevB.79.144108. URL: https://link.aps.org/doi/10.1103/PhysRevB.79.144108.

[10] Lukasz Cincio, Jacek Dziarmaga, and Marek M. Rams. "Multiscale Entanglement Renormalization Ansatz in Two Dimensions: Quantum Ising Model". In: *Phys. Rev. Lett.* 100 (24 June 2008), p. 240603. DOI: 10.1103/PhysRevLett.100.240603. URL: https://link.aps.org/doi/10.1103/PhysRevLett.100.240603.

[11] Zhi Li and Roger S. K. Mong. "Entanglement renormalization for chiral topological phases". In: *Phys. Rev. B* 99 (24 June 2019), p. 241105. DOI: 10.1103/PhysRevB.99.241105. URL: https://link.aps.org/doi/10.1103/PhysRevB.99.241105.

[12] A.S. Jermyn, R.S.K. Mong, J. Alicea, and P. Fendley. "Stability of zero modes in parafermion chains". In: *Phys. Rev. B* 90 (16 Oct. 2014), p. 165106. DOI: 10.1103/PhysRevB.90.165106.

[13] Paul Fendley. "Strong zero modes and eigenstate phase transitions in the XYZ/interacting Majorana chain". In: *Journal of Physics A: Mathematical and Theoretical* 49.30 (June 2016), 30LT01. DOI: 10.1088/1751-8113/49/30/30lt01. URL: https://doi.org/10.1088%2F1751-8113%2F49%2F30%2F30lt01.

[14] Dominic V. Else, Paul Fendley, Jack Kemp, and Chetan Nayak. "Prethermal Strong Zero Modes and Topological Qubits". In: *Phys. Rev. X* 7 (4 Dec. 2017), p. 041062. DOI: 10.1103/PhysRevX.7.041062. URL: https://link.aps.org/doi/10.1103/PhysRevX.7.041062.

[15] Markus Müller and Alexander A. Nersesyan. "Classical impurities and boundary Majorana zero modes in quantum chains". In: *Annals Phys.* 372 (2016), pp. 482–522. DOI: 10.1016/j.aop.2016.07.025.

[16] N. Moran, D. Pellegrino, J. K. Slingerland, and G. Kells. "Parafermionic clock models and quantum resonance". In: *Phys. Rev. B* 95 (23 June 2017), p. 235127. DOI: 10.1103/PhysRevB.95.235127. URL: https://link.aps.org/doi/10.1103/PhysRevB.95.235127.

[17] Loredana M. Vasiloiu, Federico Carollo, and Juan P. Garrahan. "Enhancing correlation times for edge spins through dissipation". In: *Phys. Rev. B* 98 (9 Sept. 2018), p. 094308. DOI: 10.1103/PhysRevB.98.094308. URL: https://link.aps.org/doi/10.1103/PhysRevB.98.094308.

[18] Loredana M. Vasiloiu, Federico Carollo, Matteo Marcuzzi, and Juan P. Garrahan. "Strong zero modes in a class of generalized Ising spin ladders with plaquette interactions". In: *Phys. Rev. B* 100 (2 July 2019), p. 024309. DOI: 10.1103/PhysRevB.100.024309. URL: https://link.aps.org/doi/10.1103/PhysRevB.100.024309.

[19] Daniel J. Yates, Fabian H. L. Essler, and Aditi Mitra. "Almost strong $(0, \pi)$ edge modes in clean interacting one-dimensional Floquet systems". In: *Phys. Rev. B* 99 (20 May 2019), p. 205419. DOI: 10.1103/PhysRevB.99.205419. URL: https://link.aps.org/doi/10.1103/PhysRevB.99.205419.

[20] Tibor Rakovszky, Pablo Sala, Ruben Verresen, Michael Knap, and Frank Pollmann. "Statistical localization: From strong fragmentation to strong edge modes". In: *Phys. Rev. B* 101 (12 Mar. 2020), p. 125126. DOI: 10.1103/PhysRevB.101.125126. URL: https://link.aps.org/doi/10.1103/PhysRevB.101.125126.

[21] Norman Y. Yao, Chris R. Laumann, and Ashvin Vishwanath. *Many-body localization protected quantum state transfer*. 2015. arXiv: 1508.06995 [quant-ph].

[22] Christopher T. Olund, Maxwell Block, Snir Gazit, John McGreevy, and Norman Y. Yao. "Adiabatic ground state preparation in an expanding lattice". In: *Phys. Rev. B* 101 (15 Apr. 2020), p. 155152. DOI: 10.1103/PhysRevB.101.155152. URL: https://link.aps.org/doi/10.1103/PhysRevB.101.155152.

[23] Christopher T. Olund, Norman Y. Yao, and Jack Kemp. "Boundary Strong Zero Modes". In preparation.

[24] Bryce Kobrin, Zhenbin Yang, Gregory D. Kahanamoku-Meyer, Christopher T. Olund, Joel E. Moore, Douglas Stanford, and Norman Y. Yao. "Many-Body Chaos in the Sachdev-Ye-Kitaev Model". In: *Phys. Rev. Lett.* 126 (3 Jan. 2021), p. 030602. DOI: 10.1103/PhysRevLett.126.030602. URL: https://link.aps.org/doi/10.1103/PhysRevLett.126.030602.

[25] Zachary Pagel, Weicheng Zhong, Richard H. Parker, Christopher T. Olund, Norman Y. Yao, and Holger Müller. "Symmetric Bloch oscillations of matter waves". In: *Phys. Rev. A* 102 (5 Nov. 2020), p. 053312. DOI: 10.1103/PhysRevA.102.053312. URL: https://link.aps.org/doi/10.1103/PhysRevA.102.053312.

[26] Anders S. Sørensen, Ehud Altman, Michael Gullans, J. V. Porto, Mikhail D. Lukin, and Eugene Demler. "Adiabatic preparation of many-body states in optical lattices". In: *Phys. Rev. A* 81 (6 June 2010), p. 061603. DOI: 10.1103/PhysRevA.81.061603. URL: https://link.aps.org/doi/10.1103/PhysRevA.81.061603.

[27] Peter Schauß, Johannes Zeiher, Takeshi Fukuhara, S Hild, M Cheneau, Tommaso Macri, Thomas Pohl, Immanuel Bloch, and Christian Gross. "Crystallization in Ising quantum magnets". In: *Science (New York, N.Y.)* 347 (Mar. 2015), pp. 1455–1458. DOI: 10.1126/science.1258351.

[28] Michael Lubasch, Valentin Murg, Ulrich Schneider, J. Ignacio Cirac, and Mari-Carmen Bañuls. "Adiabatic Preparation of a Heisenberg Antiferromagnet Using an Optical Superlattice". In: *Phys. Rev. Lett.* 107 (16 Oct. 2011), p. 165301. DOI: 10.1103/PhysRevLett.107.165301. URL: https://link.aps.org/doi/10.1103/PhysRevLett.107.165301.

[29] Cécile Carcy, Gaétan Hercé, Antoine Tenart, Tommaso Roscilde, and David Clément. "Certifying the Adiabatic Preparation of Ultracold Lattice Bosons in the Vicinity of the Mott Transition". In: *Phys. Rev. Lett.* 126 (4 Jan. 2021), p. 045301. DOI: 10.1103/PhysRevLett.126.045301. URL: https://link.aps.org/doi/10.1103/PhysRevLett.126.045301.

[30] Libor Veis and Jiři Pittner. "Adiabatic state preparation study of methylene". In: *The Journal of Chemical Physics* 140.21 (2014), p. 214111.

[31] Ming-Cheng Chen et al. "Demonstration of Adiabatic Variational Quantum Computing with a Superconducting Quantum Coprocessor". In: *Phys. Rev. Lett.* 125 (18 Oct. 2020), p. 180501. DOI: 10.1103/PhysRevLett.125.180501. URL: https://link.aps.org/doi/10.1103/PhysRevLett.125.180501.

[32] Manuel Endres, Hannes Bernien, Alexander Keesling, Harry Levine, Eric R. Anschuetz, Alexandre Krajenbrink, Crystal Senko, Vladan Vuletic, Markus Greiner, and Mikhail D. Lukin. "Atom-by-atom assembly of defect-free one-dimensional cold atom arrays". In: *Science* 354.6315 (2016), pp. 1024–1027. ISSN: 0036-8075. DOI: 10.1126/science.aah3752. URL: https://science.sciencemag.org/content/354/6315/1024.

[33] Daniel Barredo, Sylvain de Léséleuc, Vincent Lienhard, Thierry Lahaye, and Antoine Browaeys. "An atom-by-atom assembler of defect-free arbitrary two-dimensional atomic arrays". In: *Science* 354.6315 (2016), pp. 1021–1023. ISSN: 0036-8075. DOI: 10.1126/science.aah3778. URL: https://science.sciencemag.org/content/354/6315/1021.

[34] Harry Levine, Alexander Keesling, Ahmed Omran, Hannes Bernien, Sylvain Schwartz, Alexander S. Zibrov, Manuel Endres, Markus Greiner, Vladan Vuleti ć, and Mikhail D. Lukin. "High-Fidelity Control and Entanglement of Rydberg-Atom Qubits". In: *Phys. Rev. Lett.* 121 (12 Sept. 2018), p. 123603. DOI: 10.1103/PhysRevLett.121.123603. URL: https://link.aps.org/doi/10.1103/PhysRevLett.121.123603.

[35] H. Eugene Stanley. "Scaling, universality, and renormalization: Three pillars of modern critical phenomena". In: *Rev. Mod. Phys.* 71 (2 Mar. 1999), S358–S366. DOI: 10.1103/RevModPhys.71.S358. URL: https://link.aps.org/doi/10.1103/RevModPhys.71.S358.

[36] Kenneth G. Wilson and J. Kogut. "The renormalization group and the ϵ expansion". In: *Physics Reports* 12.2 (1974), pp. 75–199. ISSN: 0370-1573. DOI: https://doi.org/10.1016/0370-1573(74)90023-4. URL: http://www.sciencedirect.com/science/article/pii/0370157374900234.

[37] David Poulin, Angie Qarry, Rolando Somma, and Frank Verstraete. "Quantum Simulation of Time-Dependent Hamiltonians and the Convenient Illusion of Hilbert Space". In: *Phys.Rev.Lett.* 106 (2011), p. 170501. DOI: 10.1103/PhysRevLett.106.170501. arXiv: 1102.1360 [quant-ph].

[38] M. M. Wolf, F. Verstraete, M. B. Hastings, and J. I. Cirac. "Area Laws in Quantum Systems: Mutual Information and Correlations". In: *Physical Review Letters* 100.7, 070502 (Feb. 2008), p. 070502. DOI: 10.1103/PhysRevLett.100.070502. arXiv: 0704.3906 [quant-ph].

[39] M. B. Hastings. "An area law for one-dimensional quantum systems". In: *Journal of Statistical Mechanics: Theory and Experiment* 8 (Aug. 2007), p. 24. DOI: 10.1088/1742-5468/2007/08/P08024. arXiv: 0705.2024 [quant-ph].

[40] Jacob Jordan, Roman Orús, Guifre Vidal, Frank Verstraete, and J Ignacio Cirac. "Classical simulation of infinite-size quantum lattice systems in two spatial dimensions". In: *Physical review letters* 101.25 (2008), p. 250602.

[41] Norbert Schuch, David Pérez-García, and Ignacio Cirac. "Classifying quantum phases using matrix product states and projected entangled pair states". In: *Phys. Rev. B* 84 (16 Oct. 2011), p. 165139. DOI: 10.1103/PhysRevB.84.165139. URL: https://link.aps.org/doi/10.1103/PhysRevB.84.165139.

[42] Laurens Vanderstraeten, Jutho Haegeman, and Frank Verstraete. "Simulating excitation spectra with projected entangled-pair states". In: *Phys. Rev. B* 99 (16 Apr. 2019), p. 165121. DOI: 10.1103/PhysRevB.99.165121. URL: https://link.aps.org/doi/10.1103/PhysRevB.99.165121.

[43] M. C. Bañuls, D. Pérez-Garcıa, M. M. Wolf, F. Verstraete, and J. I. Cirac. "Sequentially generated states for the study of two-dimensional systems". In: *Phys. Rev. A* 77 (5 May 2008), p. 052306. DOI: 10.1103/PhysRevA.77.052306. URL: https://link.aps.org/doi/10.1103/PhysRevA.77.052306.

[44] Michael P. Zaletel and Frank Pollmann. "Isometric Tensor Network States in Two Dimensions". In: *Phys. Rev. Lett.* 124 (3 Jan. 2020), p. 037201. DOI: 10.1103/PhysRevLett.124.037201. URL: https://link.aps.org/doi/10.1103/PhysRevLett.124.037201.

[45] Tomohiro Soejima, Karthik Siva, Nick Bultinck, Shubhayu Chatterjee, Frank Pollmann, and Michael P. Zaletel. "Isometric tensor network representation of string-net liquids". In: *Phys. Rev. B* 101 (8 Feb. 2020), p. 085117. DOI: 10.1103/PhysRevB.101.085117. URL: https://link.aps.org/doi/10.1103/PhysRevB.101.085117.

[46] Roman Orus. "A Practical Introduction to Tensor Networks: Matrix Product States and Projected Entangled Pair States". In: *Annals Phys.* 349 (2014), pp. 117–158. DOI: 10.1016/j.aop.2014.06.013. arXiv: 1306.2164 [cond-mat.str-el].

[47] Laurens Vanderstraeten, Jutho Haegeman, Philippe Corboz, and Frank Verstraete. "Gradient methods for variational optimization of projected entangled-pair states". In: *Phys. Rev. B* 94 (15 Oct. 2016), p. 155123. DOI: 10.1103/PhysRevB.94.155123. URL: https://link.aps.org/doi/10.1103/PhysRevB.94.155123.

[48] Zeph Landau, Umesh Vazirani, and Thomas Vidick. "A polynomial time algorithm for the ground state of one-dimensional gapped local Hamiltonians". In: *Nature Physics* 11 (June 2015), 566 EP -. URL: https://doi.org/10.1038/nphys3345.

[49] F. Verstraete and J. I. Cirac. "Matrix product states represent ground states faithfully". In: *Phys. Rev. B* 73 (9 Mar. 2006), p. 094423. DOI: 10.1103/PhysRevB.73.094423. URL: https://link.aps.org/doi/10.1103/PhysRevB.73.094423.

[50] Itai Arad, Zeph Landau, Umesh Vazirani, and Thomas Vidick. "Rigorous RG Algorithms and Area Laws for Low Energy Eigenstates in 1D". en. In: *Communications in Mathematical Physics* 356.1 (Nov. 2017), pp. 65–105. ISSN: 0010-3616, 1432-0916. DOI: 10.1007/s00220-017-2973-z. URL: http://link.springer.com/10.1007/s00220-017-2973-z (visited on 07/28/2019).

[51] Brenden Roberts, Thomas Vidick, and Olexei I. Motrunich. "Implementation of rigorous renormalization group method for ground space and low-energy states of local Hamiltonians". en. In: *Physical Review B* 96.21 (Dec. 2017), p. 214203. ISSN: 2469-9950, 2469-9969. DOI: 10.1103/PhysRevB.96.214203. URL: https://link.aps.org/doi/10.1103/PhysRevB.96.214203 (visited on 07/28/2019).

[52] Steven R. White. "Density matrix formulation for quantum renormalization groups". In: *Phys. Rev. Lett.* 69 (19 Nov. 1992), pp. 2863–2866. DOI: 10.1103/PhysRevLett.69.2863. URL: https://link.aps.org/doi/10.1103/PhysRevLett.69.2863.

[53] Ulrich Schollwöck. "The density-matrix renormalization group in the age of matrix product states". In: *Annals of Physics* 326.1 (2011), pp. 96–192. eprint: 1008.3477.

[54] Norbert Schuch, Michael M. Wolf, Frank Verstraete, and J. Ignacio Cirac. "Entropy Scaling and Simulability by Matrix Product States". In: *Phys. Rev. Lett.* 100 (3 Jan. 2008), p. 030504. DOI: 10.1103/PhysRevLett.100.030504. URL: https://link.aps.org/doi/10.1103/PhysRevLett.100.030504.

[55] Anurag Anshu, Itai Arad, and Aditya Jain. "How local is the information in tensor networks of matrix product states or projected entangled pairs states". In: *Phys. Rev. B* 94 (19 Nov. 2016), p. 195143. DOI: 10.1103/PhysRevB.94.195143. URL: https://link.aps.org/doi/10.1103/PhysRevB.94.195143.

[56] G. Vidal. "Entanglement Renormalization". In: *Phys. Rev. Lett.* 99 (22 Nov. 2007), p. 220405. DOI: 10.1103/PhysRevLett.99.220405. URL: https://link.aps.org/doi/10.1103/PhysRevLett.99.220405.

[57] G. Vidal. "Class of Quantum Many-Body States That Can Be Efficiently Simulated". In: *Phys. Rev. Lett.* 101 (11 Sept. 2008), p. 110501. DOI: 10.1103/PhysRevLett.101.110501. URL: http://link.aps.org/doi/10.1103/PhysRevLett.101.110501.

[58] Isaac H. Kim and Brian Swingle. *Robust entanglement renormalization on a noisy quantum computer*. 2017. arXiv: 1711.07500 [quant-ph].

[59] Jutho Haegeman, Tobias J. Osborne, Henri Verschelde, and Frank Verstraete. "Entanglement Renormalization for Quantum Fields in Real Space". In: *Phys. Rev. Lett.* 110 (10 Mar. 2013), p. 100402. DOI: 10.1103/PhysRevLett.110.100402. URL: http://link.aps.org/doi/10.1103/PhysRevLett.110.100402.

[60] Jordan S. Cotler, M. Reza Mohammadi Mozaffar, Ali Mollabashi, and Ali Naseh. "Entanglement renormalization for weakly interacting fields". In: *Phys. Rev. D* 99 (8 Apr. 2019), p. 085005. DOI: 10.1103/PhysRevD.99.085005. URL: https://link.aps.org/doi/10.1103/PhysRevD.99.085005.

[61] Glen Evenbly and Steven R. White. "Entanglement Renormalization and Wavelets". In: *Phys. Rev. Lett.* 116 (14 Apr. 2016), p. 140403. DOI: 10.1103/PhysRevLett.116.140403. URL: https://link.aps.org/doi/10.1103/PhysRevLett.116.140403.

[62] Jutho Haegeman, Brian Swingle, Michael Walter, Jordan Cotler, Glen Evenbly, and Volkher B. Scholz. "Rigorous Free-Fermion Entanglement Renormalization from Wavelet Theory". In: *Phys. Rev. X* 8 (1 Jan. 2018), p. 011003. DOI: 10.1103/PhysRevX.8.011003. URL: https://link.aps.org/doi/10.1103/PhysRevX.8.011003.

[63] J. Haah. "Bifurcation in entanglement renormalization group flow of a gapped spin model". In: *Phys. Rev. B* 89.7, 075119 (Feb. 2014), p. 075119. DOI: 10.1103/PhysRevB.89.075119. arXiv: 1310.4507 [cond-mat.str-el].

[64] Wilbur Shirley, Kevin Slagle, Zhenghan Wang, and Xie Chen. "Fracton Models on General Three-Dimensional Manifolds". In: *Phys. Rev. X* 8 (3 Aug. 2018), p. 031051. DOI: 10.1103/PhysRevX.8.031051. URL: https://link.aps.org/doi/10.1103/PhysRevX.8.031051.

[65] Wilbur Shirley, Kevin Slagle, and Xie Chen. "Foliated fracton order in the checkerboard model". In: *Phys. Rev. B* 99 (11 Mar. 2019), p. 115123. DOI: 10.1103/PhysRevB.99.115123. URL: https://link.aps.org/doi/10.1103/PhysRevB.99.115123.

[66] Aram Harrow and Saeed Mehraban. *Approximate unitary t-designs by short random quantum circuits using nearest-neighbor and long-range gates*. 2018. arXiv: 1809.06957 [quant-ph].

[67] Guifré Vidal. "Efficient Classical Simulation of Slightly Entangled Quantum Computations". In: *Phys. Rev. Lett.* 91 (14 Oct. 2003), p. 147902. DOI: 10.1103/PhysRevLett.91.147902. URL: https://link.aps.org/doi/10.1103/PhysRevLett.91.147902.

[68] Guifré Vidal. "Efficient Simulation of One-Dimensional Quantum Many-Body Systems". In: *Phys. Rev. Lett.* 93 (4 July 2004), p. 040502. DOI: 10.1103/PhysRevLett.93.040502. URL: https://link.aps.org/doi/10.1103/PhysRevLett.93.040502.

[69] Richard Cole, Frank Pollmann, and Joseph J. Betouras. "Entanglement scaling and spatial correlations of the transverse-field Ising model with perturbations". In: *Phys. Rev. B* 95 (21 June 2017), p. 214410. DOI: 10.1103/PhysRevB.95.214410. URL: https://link.aps.org/doi/10.1103/PhysRevB.95.214410.

[70] Jun Li, Ruihua Fan, Hengyan Wang, Bingtian Ye, Bei Zeng, Hui Zhai, Xinhua Peng, and Jiangfeng Du. "Measuring Out-of-Time-Order Correlators on a Nuclear Magnetic Resonance Quantum Simulator". In: *Phys. Rev. X* 7 (3 July 2017), p. 031011. DOI: 10.1103/PhysRevX.7.031011. URL: https://link.aps.org/doi/10.1103/PhysRevX.7.031011.

[71] Bryce Gadway and Bo Yan. "Strongly interacting ultracold polar molecules". In: *Journal of Physics B: Atomic, Molecular and Optical Physics* 49.15 (June 2016), p. 152002. DOI: 10.1088/0953-4075/49/15/152002. URL: https://doi.org/10.1088%2F0953-4075%2F49%2F15%2F152002.

[72] Marcus W. Doherty, Neil B. Manson, Paul Delaney, Fedor Jelezko, Jörg Wrachtrup, and Lloyd C.L. Hollenberg. "The nitrogen-vacancy colour centre in diamond". In: *Physics Reports* 528.1 (2013). The nitrogen-vacancy colour centre in diamond, pp. 1–45. ISSN: 0370-1573. DOI: https://doi.org/10.1016/j.physrep.2013.02.001. URL: http://www.sciencedirect.com/science/article/pii/S0370157313000562.

[73] C. Monroe et al. *Programmable Quantum Simulations of Spin Systems with Trapped Ions*. 2019. arXiv: 1912.07845 [quant-ph].

[74] John Preskill. "Quantum Computing in the NISQ era and beyond". In: *Quantum* 2 (Aug. 2018), p. 79. ISSN: 2521-327X. DOI: 10.22331/q-2018-08-06-79. URL: https://doi.org/10.22331/q-2018-08-06-79.

[75] Itai Arad and Zeph Landau. "Quantum Computation and the Evaluation of Tensor Networks". en. In: *SIAM Journal on Computing* 39.7 (Jan. 2010), pp. 3089–3121. ISSN: 0097-5397, 1095-7111. DOI: 10.1137/080739379. URL: http://epubs.siam.org/doi/10.1137/080739379 (visited on 02/10/2020).

[76] Igor L. Markov and Yaoyun Shi. "Simulating Quantum Computation by Contracting Tensor Networks". en. In: *SIAM Journal on Computing* 38.3 (Jan. 2008), pp. 963–981. ISSN: 0097-5397, 1095-7111. DOI: 10.1137/050644756. URL: http://epubs.siam.org/doi/10.1137/050644756 (visited on 02/10/2020).

[77] G. Evenbly and G. Vidal. "Algorithms for entanglement renormalization". In: (2007). DOI: 10.1103/PhysRevB.79.144108. eprint: arXiv:0707.1454.

[78] A.Yu. Kitaev. "Fault-tolerant quantum computation by anyons". In: *Annals of Physics* 303.1 (2003), pp. 2–30. ISSN: 0003-4916. DOI: https://doi.org/10.1016/S0003-4916(02)00018-0. URL: http://www.sciencedirect.com/science/article/pii/S0003491602000180.

[79] Chetan Nayak, Steven H. Simon, Ady Stern, Michael Freedman, and Sankar Das Sarma. "Non-Abelian anyons and topological quantum computation". In: *Rev. Mod. Phys.* 80 (3 Sept. 2008), pp. 1083–1159. DOI: 10.1103/RevModPhys.80.1083. URL: https://link.aps.org/doi/10.1103/RevModPhys.80.1083.

[80] Sankar Das Sarma, Michael Freedman, and Chetan Nayak. "Majorana zero modes and topological quantum computation". In: *npj Quantum Information* 1.1 (2015), p. 15001. DOI: 10.1038/npjqi.2015.1. URL: https://doi.org/10.1038/npjqi.2015.1.

[81] Anushya Chandran, Vedika Khemani, C. R. Laumann, and S. L. Sondhi. "Many-body localization and symmetry-protected topological order". In: *Phys. Rev. B* 89 (14 Apr. 2014), p. 144201. DOI: 10.1103/PhysRevB.89.144201. URL: https://link.aps.org/doi/10.1103/PhysRevB.89.144201.

[82] Andrew C. Potter and Ashvin Vishwanath. "Protection of topological order by symmetry and many-body localization". In: (2015). arXiv: 1506.00592 [cond-mat.dis-nn].

[83] Yasaman Bahri, Ronen Vosk, Ehud Altman, and Ashvin Vishwanath. "Localization and topology protected quantum coherence at the edge of hot matter". In: *Nature Communications* 6 (July 2015), 7341 EP -. eprint: 1307.4092. URL: http://dx.doi.org/10.1038/ncomms8341.

[84] P. Fendley. "Parafermionic edge zero modes in Z_n-invariant spin chains". In: *J. Stat. Mech.* 11 (Nov. 2012), p. 20. DOI: 10.1088/1742-5468/2012/11/P11020.

[85] Jason Alicea and Paul Fendley. "Topological Phases with Parafermions: Theory and Blueprints". In: *Annual Review of Condensed Matter Physics* 7.1 (2016), pp. 119–139. DOI: 10.1146/annurev-conmatphys-031115-011336. eprint: https://doi.org/10.1146/annurev-conmatphys-031115-011336. URL: https://doi.org/10.1146/annurev-conmatphys-031115-011336.

[86] A Yu Kitaev. "Unpaired Majorana fermions in quantum wires". In: *Physics-Uspekhi* 44.10S (Oct. 2001), pp. 131–136. DOI: 10.1070/1063-7869/44/10s/s29. URL: https://doi.org/10.1070%2F1063-7869%2F44%2F10s%2Fs29.

[87] Jack Kemp, Norman Y Yao, Christopher R Laumann, and Paul Fendley. "Long coherence times for edge spins". In: *Journal of Statistical Mechanics: Theory and Experiment* 2017.6 (June 2017), p. 063105. DOI: 10.1088/1742-5468/aa73f0. URL: https://doi.org/10.1088%2F1742-5468%2Faa73f0.

[88] Daniel J. Yates, Alexander G. Abanov, and Aditi Mitra. "Lifetime of Almost Strong Edge-Mode Operators in One-Dimensional, Interacting, Symmetry Protected Topological Phases". In: *Phys. Rev. Lett.* 124 (20 May 2020), p. 206803. DOI: 10.1103/PhysRevLett.124.206803. URL: https://link.aps.org/doi/10.1103/PhysRevLett.124.206803.

[89] Daniel J. Yates, Alexander G. Abanov, and Aditi Mitra. "Dynamics of almost strong edge modes in spin chains away from integrability". In: *Phys. Rev. B* 102 (19 Nov. 2020), p. 195419. DOI: 10.1103/PhysRevB.102.195419. URL: https://link.aps.org/doi/10.1103/PhysRevB.102.195419.

[90] Jack Kemp, Norman Y. Yao, and Chris R. Laumann. "Symmetry-Enhanced Boundary Qubits at Infinite Temperature". In: *Phys. Rev. Lett.* 125 (20 Nov. 2020), p. 200506. DOI: 10.1103/PhysRevLett.125.200506. URL: https://link.aps.org/doi/10.1103/PhysRevLett.125.200506.

[91] Jason Alicea, Yuval Oreg, Gil Refael, Felix von Oppen, and Matthew P. A. Fisher. "Non-Abelian Statistics and Topological Quantum Information Processing in 1D Wire Networks". In: *Nature Physics* 7.5 (May 2011), pp. 412–417. ISSN: 1745-2481. DOI: 10.1038/nphys1915.

[92] P. Jordan and E. Wigner. "Über das Paulische Äquivalenzverbot". In: *Zeitschrift für Physik* 47.9 (1928), pp. 631–651. DOI: 10.1007/BF01331938. URL: https://doi.org/10.1007/BF01331938.

[93] Paul Fendley. "Free parafermions". In: *Journal of Physics A: Mathematical and Theoretical* 47.7 (Jan. 2014), p. 075001. DOI: 10.1088/1751-8113/47/7/075001. URL: https://doi.org/10.1088%2F1751-8113%2F47%2F7%2F075001.

[94] T. D. Schultz, D. C. Mattis, and E. H. Lieb. "Two-Dimensional Ising Model as a Soluble Problem of Many Fermions". In: *Rev. Mod. Phys.* 36 (3 July 1964), pp. 856–871. DOI: 10.1103/RevModPhys.36.856.

[95] Sergey Bravyi and Robert König. "Disorder-Assisted Error Correction in Majorana Chains". In: *Commun. Math. Phys.* 316.3 (Dec. 2012), pp. 641–692. ISSN: 1432-0916. DOI: 10.1007/s00220-012-1606-9.

[96] In fact, due to the system's free-fermion nature, the autocorrelator never decays, but rather starts to coherently oscillate.

[97] T. Kyle Petersen. *Eulerian Numbers*. Birkhäuser Advanced Texts Basler Lehrbücher. Birkhäuser Basel, 2015. ISBN: 978-1-4939-3090-6. DOI: 10.1007/978-1-4939-3091-3.

[98] Greg Meyer. *GregDMeyer/Dynamite v0.1.0*. Zenodo. Jan. 2020. DOI: 10.5281/zenodo.3606826.

[99] Marek P. Grabowski and Pierre Mathieu. "Quantum Integrals of Motion for the Heisenberg Spin Chain". In: *Mod. Phys. Lett. A* 09.24 (Aug. 1994), pp. 2197–2206. ISSN: 0217-7323. DOI: 10.1142/S0217732394002057.

[100] Yuji Nozawa and Kouhei Fukai. "Explicit Construction of Local Conserved Quantities in the XYZ Spin-1/2 Chain". In: *Phys. Rev. Lett.* 125.9 (Aug. 2020), p. 090602. DOI: 10.1103/PhysRevLett.125.090602.

[101] Bernard Nienhuis and Onno Huijgen. "The Local Conserved Quantities of the Closed XXZ Chain". In: *J. Phys. A: Math. Theor.* 54 (June 2021), p. 304001. ISSN: 1751-8121. DOI: 10.1088/1751-8121/ac0961.

[102] J. R. Ackerhalt and K. Rza żewski. "Heisenberg-picture operator perturbation theory". In: *Phys. Rev. A* 12 (6 Dec. 1975), pp. 2549–2567. DOI: 10.1103/PhysRevA.12.2549. URL: https://link.aps.org/doi/10.1103/PhysRevA.12.2549.

[103] Nima Lashkari, Douglas Stanford, Matthew Hastings, Tobias Osborne, and Patrick Hayden. "Towards the fast scrambling conjecture". In: *Journal of High Energy Physics* 2013.4 (2013), pp. 1–33.

[104] Stephen H. Shenker and Douglas Stanford. "Stringy effects in scrambling". In: *J. High Energ. Phys.* 2015 (2015), p. 132. DOI: 10.1007/JHEP05(2015)132.

[105] Stephen H. Shenker and Douglas Stanford. "Black holes and the butterfly effect". In: *J. High Energ. Phys.* 2014 (2014), p. 67. DOI: 10.1007/JHEP03(2014)067. arXiv: 1306.0622.

[106] Yasuhiro Sekino and Leonard Susskind. "Fast scramblers". In: *Journal of High Energy Physics* 2008.10 (2008), p. 065.

[107] Brian Swingle, Gregory Bentsen, Monika Schleier-Smith, and Patrick Hayden. "Measuring the scrambling of quantum information". In: *Phys. Rev. A* 94 (2016), p. 040302. DOI: 10.1103/PhysRevA.94.040302. arXiv: 1602.06271.

[108] Guanyu Zhu, Mohammad Hafezi, and Tarun Grover. "Measurement of many-body chaos using a quantum clock". In: *Phys. Rev. A* 94 (2016), p. 062329. DOI: 10.1103/PhysRevA.94.062329. arXiv: 1607.00079.

[109] Justin Dressel, José Raúl González Alonso, Mordecai Waegell, and Nicole Yunger Halpern. "Strengthening weak measurements of qubit out-of-time-order correlators". In: *Physical Review A* 98.1 (2018), p. 012132.

[110] Beni Yoshida and Norman Y. Yao. "Disentangling Scrambling and Decoherence via Quantum Teleportation". In: *Phys. Rev. X* 9 (2019), p. 011006. DOI: 10.1103/PhysRevX.9.011006. arXiv: 1803.10772.

[111] Norman Y. Yao, Fabian Grusdt, Brian Swingle, Mikhail D. Lukin, Dan M. Stamper-Kurn, Joel E. Moore, and Eugene A. Demler. "Interferometric Approach to Probing Fast Scrambling". In: (). arXiv: 1607.01801.

[112] Gregory Bentsen, Tomohiro Hashizume, Anton S. Buyskikh, Emily J. Davis, Andrew J. Daley, Steven S. Gubser, and Monika Schleier-Smith. "Treelike Interactions and Fast Scrambling with Cold Atoms". In: *Phys. Rev. Lett.* 123 (2019), p. 130601. DOI: 10.1103/PhysRevLett.123.130601. arXiv: 1905.11430.

[113] JAN Bruin, H Sakai, RS Perry, and AP Mackenzie. "Similarity of scattering rates in metals showing T-linear resistivity". In: *Science* 339.6121 (2013), pp. 804–807.

[114] Yunxiang Liao and Victor Galitski. "Nonlinear sigma model approach to many-body quantum chaos: Regularized and unregularized out-of-time-ordered correlators". In: *Phys. Rev. B* 98 (2018), p. 205124. DOI: 10.1103/PhysRevB.98.205124. arXiv: 1807.09799.

[115] R. J. Lewis-Swan, A. Safavi-Naini, J. J. Bollinger, and A. M. Rey. "Unifying scrambling, thermalization and entanglement through measurement of fidelity out-of-time-order correlators in the Dicke model". In: *Nat Commun* 10 (2019), p. 1581. DOI: 10.1038/s41467-019-09436-y. arXiv: 1808.07134.

[116] Douglas Stanford. "Many-body chaos at weak coupling". In: *J. High Energ. Phys.* 2016 (2016), p. 9. DOI: 10.1007/JHEP10(2016)009. arXiv: 1512.07687.

[117] Debanjan Chowdhury and Brian Swingle. "Onset of many-body chaos in the O(N) model". In: *Phys. Rev. D* 96 (2017), p. 065005. DOI: 10.1103/PhysRevD.96.065005. arXiv: 1703.02545.

[118] Koji Hashimoto, Kyoung-Bum Huh, Keun-Young Kim, and Ryota Watanabe. "Exponential growth of out-of-time-order correlator without chaos: inverted harmonic oscillator". In: *Journal of High Energy Physics* 2020.11 (2020), p. 68.

[119] Martin Gärttner, Justin G. Bohnet, Arghavan Safavi-Naini, Michael L. Wall, John J. Bollinger, and Ana Maria Rey. "Measuring out-of-time-order correlations and multiple quantum spectra in a trapped-ion quantum magnet". In: *Nature Phys* 13 (2017), p. 781. DOI: 10.1038/nphys4119. arXiv: 1608.08938.

[120] K. A. Landsman, C. Figgatt, T. Schuster, N. M. Linke, B. Yoshida, N. Y. Yao, and C. Monroe. "Verified quantum information scrambling". In: *Nature* 567 (2019), p. 61. DOI: 10.1038/s41586-019-0952-6. arXiv: 1806.02807.

[121] M. S. Blok, V. V. Ramasesh, T. Schuster, K. O'Brien, J. M. Kreikebaum, D. Dahlen, A. Morvan, B. Yoshida, N. Y. Yao, and I. Siddiqi. "Quantum Information Scrambling on a Superconducting Qutrit Processor". In: *Phys. Rev. X* 11 (2 Apr. 2021), p. 021010. DOI: 10.1103/PhysRevX.11.021010. URL: https://link.aps.org/doi/10.1103/PhysRevX.11.021010.

[122] Subir Sachdev and Jinwu Ye. "Gapless spin-fluid ground state in a random quantum Heisenberg magnet". In: *Phys. Rev. Lett.* 70 (1993), p. 3339. DOI: 10.1103/PhysRevLett.70.3339.

[123] Alexei Kitaev. *A simple model of quantum holography.* KITP Program: Entanglement in Strongly-Correlated Quantum Matter. 2015. URL: http://online.kitp.ucsb.edu/online/entangled15/kitaev/rm/jwvideo.html.

[124] Juan Maldacena and Douglas Stanford. "Remarks on the Sachdev-Ye-Kitaev model". In: *Phys. Rev. D* 94 (2016), p. 106002. DOI: 10.1103/PhysRevD.94.106002. arXiv: 1604.07818.

[125] Juan Maldacena, Douglas Stanford, and Zhenbin Yang. "Conformal symmetry and its breaking in two-dimensional nearly anti-de Sitter space". In: *Progress of Theoretical and Experimental Physics* 2016.12 (Nov. 2016). 12C104. ISSN: 2050-3911. DOI: 10.1093/ptep/ptw124. eprint: https://academic.oup.com/ptep/article-pdf/2016/12/12C104/9620935/ptw124.pdf. URL: https://doi.org/10.1093/ptep/ptw124.

[126] Kristan Jensen. "Chaos in AdS2Holography". In: *Phys. Rev. Lett.* 117 (2016), p. 111601. DOI: 10.1103/PhysRevLett.117.111601. arXiv: 1605.06098.

[127] Joseph Polchinski and Vladimir Rosenhaus. "The spectrum in the Sachdev-Ye-Kitaev model". In: *Journal of High Energy Physics* 2016.4 (2016), p. 1.

[128] Daniel A. Roberts, Douglas Stanford, and Alexandre Streicher. "Operator growth in the SYK model". In: *Journal of High Energy Physics* 2018.6 (2018), p. 122.

[129] Subir Sachdev. "Bekenstein-Hawking entropy and strange metals". In: *Physical Review X* 5.4 (2015), p. 041025.

[130] Yousef Saad. "Analysis of some Krylov subspace approximations to the matrix exponential operator". In: *SIAM Journal on Numerical Analysis* 29.1 (1992), pp. 209–228.

[131] Tim Kovachy, Jason M. Hogan, David M. S. Johnson, and Mark A. Kasevich. "Optical lattices as waveguides and beam splitters for atom interferometry: An analytical treatment and proposal of applications". In: *Phys. Rev. A* 82 (1 July 2010), p. 013638. DOI: 10.1103/PhysRevA.82.013638. URL: https://link.aps.org/doi/10.1103/PhysRevA.82.013638.

[132] Ekkehard Peik, Maxime Ben Dahan, Isabelle Bouchoule, Yvan Castin, and Christophe Salomon. "Bloch oscillations of atoms, adiabatic rapid passage, and monokinetic atomic beams". In: *Phys. Rev. A* 55 (4 Apr. 1997), pp. 2989–3001. DOI: 10.1103/PhysRevA.55.2989. URL: https://link.aps.org/doi/10.1103/PhysRevA.55.2989.

[133] Felix Bloch. "Über die Quantenmechanik der Elektronen in Kristallgittern". In: *Zeitschrift für Physik* 52.7 (1929), pp. 555–600. DOI: 10.1007/BF01339455. URL: https://doi.org/10.1007/BF01339455.

[134] Gregory H. Wannier. "Wave Functions and Effective Hamiltonian for Bloch Electrons in an Electric Field". In: *Phys. Rev.* 117 (2 Jan. 1960), pp. 432–439. DOI: 10.1103/PhysRev.117.432. URL: https://link.aps.org/doi/10.1103/PhysRev.117.432.

[135] A. Rabinovitch and J. Zak. "Does a Bloch electron in a constant electric field oscillate?" In: *Physics Letters A* 40.3 (1972), pp. 189–190. ISSN: 0375-9601. DOI: https://doi.org/10.1016/0375-9601(72)90649-4. URL: https://www.sciencedirect.com/science/article/pii/0375960172906494.

[136] J. Zak. "Comment on "Time evolution of Bloch electrons in a homogeneous electric field"". In: *Phys. Rev. B* 38 (9 Sept. 1988), pp. 6322–6323. DOI: 10.1103/PhysRevB.38.6322. URL: https://link.aps.org/doi/10.1103/PhysRevB.38.6322.

[137] G. Nenciu. "Dynamics of band electrons in electric and magnetic fields: rigorous justification of the effective Hamiltonians". In: *Rev. Mod. Phys.* 63 (1 Jan. 1991), pp. 91–127. DOI: 10.1103/RevModPhys.63.91. URL: https://link.aps.org/doi/10.1103/RevModPhys.63.91.

[138] J. Feldmann, K. Leo, J. Shah, D. A. B. Miller, J. E. Cunningham, T. Meier, G. von Plessen, A. Schulze, P. Thomas, and S. Schmitt-Rink. "Optical investigation of Bloch oscillations in a semiconductor superlattice". In: *Phys. Rev. B* 46 (11 Sept. 1992), pp. 7252–7255. DOI: 10.1103/PhysRevB.46.7252. URL: https://link.aps.org/doi/10.1103/PhysRevB.46.7252.

[139] Christian Waschke, Hartmut G. Roskos, Ralf Schwedler, Karl Leo, Heinrich Kurz, and Klaus Köhler. "Coherent submillimeter-wave emission from Bloch oscillations in a semiconductor superlattice". In: *Phys. Rev. Lett.* 70 (21 May 1993), pp. 3319–3322. DOI: 10.1103/PhysRevLett.70.3319. URL: https://link.aps.org/doi/10.1103/PhysRevLett.70.3319.

[140] A. Yulin, R. Driben, and T. Meier. "Bloch oscillations and resonant radiation of light propagating in arrays of nonlinear fibers with high-order dispersion". In: *Phys. Rev. A* 96 (3 Sept. 2017), p. 033827. DOI: 10.1103/PhysRevA.96.033827. URL: https://link.aps.org/doi/10.1103/PhysRevA.96.033827.

[141] R. Driben, V. V. Konotop, T. Meier, and A. V. Yulin. "Bloch oscillations sustained by nonlinearity". In: *Scientific Reports* 7.1 (2017), p. 3194. DOI: 10.1038/s41598-017-03400-w. URL: https://doi.org/10.1038/s41598-017-03400-w.

[142] Maxime Ben Dahan, Ekkehard Peik, Jakob Reichel, Yvan Castin, and Christophe Salomon. "Bloch Oscillations of Atoms in an Optical Potential". In: *Phys. Rev. Lett.* 76 (24 June 1996), pp. 4508–4511. DOI: 10.1103/PhysRevLett.76.4508. URL: https://link.aps.org/doi/10.1103/PhysRevLett.76.4508.

[143] S. R. Wilkinson, C. F. Bharucha, K. W. Madison, Qian Niu, and M. G. Raizen. "Observation of Atomic Wannier-Stark Ladders in an Accelerating Optical Potential". In: *Phys. Rev. Lett.* 76 (24 June 1996), pp. 4512–4515. DOI: 10.1103/PhysRevLett.76.4512. URL: https://link.aps.org/doi/10.1103/PhysRevLett.76.4512.

[144] Richard H. Parker, Chenghui Yu, Weicheng Zhong, Brian Estey, and Holger Müller. "Measurement of the fine-structure constant as a test of the Standard Model". In: *Science* 360.6385 (2018), pp. 191–195.

[145] Rym Bouchendira, Pierre Cladé, Saıda Guellati-Khélifa, Fran çois Nez, and Fran çois Biraben. "New Determination of the Fine Structure Constant and Test of the Quantum Electrodynamics". In: *Phys. Rev. Lett.* 106 (8 Feb. 2011), p. 080801. DOI: 10.1103/PhysRevLett.106.080801. URL: https://link.aps.org/doi/10.1103/PhysRevLett.106.080801.

[146] G. Rosi, F. Sorrentino, L. Cacciapuoti, M. Prevedelli, and G. M. Tino. "Precision measurement of the Newtonian gravitational constant using cold atoms". In: *Nature* 510.7506 (2014), pp. 518–521.

[147] J. B. Fixler, G. T. Foster, J. M. McGuirk, and M. A. Kasevich. "Atom Interferometer Measurement of the Newtonian Constant of Gravity". In: *Science* 315.5808 (2007), pp. 74–77.

[148] Lin Zhou et al. "Test of Equivalence Principle at 10^{-8} Level by a Dual-Species Double-Diffraction Raman Atom Interferometer". In: *Phys. Rev. Lett.* 115 (1 July 2015), p. 013004. DOI: 10.1103/PhysRevLett.115.013004. URL: https://link.aps.org/doi/10.1103/PhysRevLett.115.013004.

[149] G. Rosi, G. D'Amico, L. Cacciapuoti, F. Sorrentino, M. Prevedelli, M. Zych, Č. Brukner, and G. M. Tino. "Quantum test of the equivalence principle for atoms in coherent superposition of internal energy states". In: *Nature Communications* 8.1 (2017), p. 15529.

[150] P. Hamilton, M. Jaffe, P. Haslinger, Q. Simmons, H. Müller, and J. Khoury. "Atom-interferometry constraints on dark energy". In: *Science* 349.6250 (2015), pp. 849–851.

[151] Matt Jaffe, Philipp Haslinger, Victoria Xu, Paul Hamilton, Amol Upadhye, Benjamin Elder, Justin Khoury, and Holger Müller. "Testing sub-gravitational forces on atoms from a miniature in-vacuum source mass". In: *Nature Physics* 13.10 (2017), pp. 938–942.

[152] L. Zhou, Z. Y. Xiong, W. Yang, B. Tang, W. C. Peng, K. Hao, R. B. Li, M. Liu, J. Wang, and M. S. Zhan. "Development of an atom gravimeter and status of the 10-meter atom interferometer for precision gravity measurement". In: *Gen. Relativ. Gravit* 43 (2011), pp. 1931–1942.

[153] Xuejian Wu, Zachary Pagel, Bola S. Malek, Timothy H. Nguyen, Fei Zi, Daniel S. Scheirer, and Holger Müller. "Gravity surveys using a mobile atom interferometer". In: *Science Advances* 5.9 (2019), eaax0800.

[154] Peter Asenbaum, Chris Overstreet, Tim Kovachy, Daniel D. Brown, Jason M. Hogan, and Mark A. Kasevich. "Phase Shift in an Atom Interferometer due to Spacetime Curvature across its Wave Function". In: *Phys. Rev. Lett.* 118 (18 May 2017), p. 183602. DOI: 10.1103/PhysRevLett.118.183602. URL: https://link.aps.org/doi/10.1103/PhysRevLett.118.183602.

[155] Malo Cadoret, Estefania de Mirandes, Pierre Cladé, Saıda Guellati-Khélifa, Catherine Schwob, Fran çois Nez, Lucile Julien, and Fran çois Biraben. "Combination of Bloch Oscillations with a Ramsey-Bordé Interferometer: New Determination of the Fine Structure Constant". In: *Phys. Rev. Lett.* 101 (23 Dec. 2008), p. 230801. DOI: 10.1103/PhysRevLett.101.230801. URL: https://link.aps.org/doi/10.1103/PhysRevLett.101.230801.

[156] Victoria Xu, Matt Jaffe, Cristian D. Panda, Sofus L. Kristensen, Logan W. Clark, and Holger Müller. "Probing gravity by holding atoms for 20 seconds". In: *Science* 366.6466 (2019), pp. 745–749.

[157] Vladimir S. Malinovsky and Paul R. Berman. "Momentum transfer using chirped standing-wave fields: Bragg scattering". In: *Phys. Rev. A* 68 (2 Aug. 2003), p. 023610. DOI: 10.1103/PhysRevA.68.023610. URL: https://link.aps.org/doi/10.1103/PhysRevA.68.023610.

[158] Holger Müller, Sheng-wey Chiow, Sven Herrmann, and Steven Chu. "Atom Interferometers with Scalable Enclosed Area". In: *Phys. Rev. Lett.* 102 (24 June 2009), p. 240403. DOI: 10.1103/PhysRevLett.102.240403. URL: https://link.aps.org/doi/10.1103/PhysRevLett.102.240403.

[159] Sven Abend. "Atom-chip gravimeter with Bose-Einstein condensates". PhD thesis. Leibniz U., Hannover, 2017. DOI: 10.15488/8921.

[160] Martina Gebbe et al. "Twin-lattice atom interferometry". In: *Nature Communications* 12.1 (2021), p. 2544.

[161] Chenghui Yu, Weicheng Zhong, Brian Estey, Joyce Kwan, Richard H. Parker, and Holger Müller. "Atom-Interferometry Measurement of the Fine Structure Constant". In: *Annalen der Physik* 531.5 (2019), p. 1800346. DOI: https://doi.org/10.1002/andp.201800346. eprint: https://onlinelibrary.wiley.com/doi/pdf/10.1002/andp.201800346. URL: https://onlinelibrary.wiley.com/doi/abs/10.1002/andp.201800346.

[162] Dong-Feng Gao, Jin Wang, and Ming-Sheng Zhan. "Atomic Interferometric Gravitational-Wave Space Observatory (AIGSO)". In: *Communications in Theoretical Physics* 69.1 (Jan. 2018), p. 37.

[163] Peter W. Graham, Jason M. Hogan, Mark A. Kasevich, and Surjeet Rajendran. "Resonant mode for gravitational wave detectors based on atom interferometry". In: *Phys. Rev. D* 94 (10 Nov. 2016), p. 104022. DOI: 10.1103/PhysRevD.94.104022. URL: https://link.aps.org/doi/10.1103/PhysRevD.94.104022.

[164] Holger Müller, Sheng-wey Chiow, Quan Long, Sven Herrmann, and Steven Chu. "Atom Interferometry with up to 24-Photon-Momentum-Transfer Beam Splitters". In: *Phys. Rev. Lett.* 100 (18 May 2008), p. 180405. DOI: 10.1103/PhysRevLett.100.180405. URL: https://link.aps.org/doi/10.1103/PhysRevLett.100.180405.

[165] Pierre Cladé. "Bloch oscillations in atom interferometry". In: *arXiv: Atomic Physics* 38 (2015), pp. 173–207.

[166] Andrey R. Kolovsky and Hans Jürgen Korsch. "Bloch oscillations of cold atoms in optical lattices". In: *International Journal of Modern Physics B* 18.09 (2004), pp. 1235–1260. DOI: 10.1142/S0217979204024483. eprint: https://doi.org/10.1142/S0217979204024483. URL: https://doi.org/10.1142/S0217979204024483.

[167] Qian Niu and M. G. Raizen. "How Landau-Zener Tunneling Takes Time". In: *Phys. Rev. Lett.* 80 (16 Apr. 1998), pp. 3491–3494. DOI: 10.1103/PhysRevLett.80.3491. URL: https://link.aps.org/doi/10.1103/PhysRevLett.80.3491.

[168] Le Tuan Anh Ho and Liviu F. Chibotaru. "A simple derivation of the Landau–Zener formula". In: *Phys. Chem. Chem. Phys.* 16 (2014), pp. 6942–6945.

[169] J. K. Stockton, K. Takase, and M. A. Kasevich. "Absolute Geodetic Rotation Measurement Using Atom Interferometry". In: *Phys. Rev. Lett.* 107 (13 Sept. 2011), p. 133001. DOI: 10.1103/PhysRevLett.107.133001. URL: https://link.aps.org/doi/10.1103/PhysRevLett.107.133001.

[170] S. Abend et al. "Atom-Chip Fountain Gravimeter". In: *Phys. Rev. Lett.* 117 (20 Nov. 2016), p. 203003. DOI: 10.1103/PhysRevLett.117.203003. URL: https://link.aps.org/doi/10.1103/PhysRevLett.117.203003.

[171] C. Wachter. "Numerical Solution of the Time-Dependent 1D-Schrödinger Equation using Absorbing Boundary Conditions". University of Graz, 2017.

[172] Florian Fitzek, Jan-Niclas Siemß, Stefan Seckmeyer, Holger Ahlers, Ernst M. Rasel, Klemens Hammerer, and Naceur Gaaloul. "Universal atom interferometer simulation of elastic scattering processes". In: *Scientific Reports* 10.1 (2020), p. 22120.

[173] M. Büchner, R. Delhuille, A. Miffre, C. Robilliard, J. Vigué, and C. Champenois. "Diffraction phases in atom interferometers". In: *Phys. Rev. A* 68 (1 July 2003), p. 013607. DOI: 10.1103/PhysRevA.68.013607. URL: https://link.aps.org/doi/10.1103/PhysRevA.68.013607.

[174] Brian Estey, Chenghui Yu, Holger Müller, Pei-Chen Kuan, and Shau-Yu Lan. "High-Resolution Atom Interferometers with Suppressed Diffraction Phases". In: *Phys. Rev. Lett.* 115 (8 Aug. 2015), p. 083002. DOI: 10.1103/PhysRevLett.115.083002. URL: https://link.aps.org/doi/10.1103/PhysRevLett.115.083002.

[175] Sheng-wey Chiow, Tim Kovachy, Hui-Chun Chien, and Mark A. Kasevich. "102$\hbar k$ Large Area Atom Interferometers". In: *Phys. Rev. Lett.* 107 (13 Sept. 2011), p. 130403. DOI: 10.1103/PhysRevLett.107.130403. URL: https://link.aps.org/doi/10.1103/PhysRevLett.107.130403.

[176] Ethan R. Elliott, Markus C. Krutzik, Jason R. Williams, Robert J. Thompson, and David C. Aveline. "NASA's Cold Atom Lab (CAL): system development and ground test status". In: *npj Microgravity* 4.1 (2018), p. 16.

[177] Sascha Kulas et al. "Miniaturized Lab System for Future Cold Atom Experiments in Microgravity". In: *Microgravity Science and Technology* 29.1 (2017), pp. 37–48.

[178] Richard H. Parker, Chenghui Yu, Brian Estey, Weicheng Zhong, Eric Huang, and Holger Müller. "Controlling the multiport nature of Bragg diffraction in atom interferometry". In: *Phys. Rev. A* 94 (5 Nov. 2016), p. 053618. DOI: 10.1103/PhysRevA.94.053618. URL: https://link.aps.org/doi/10.1103/PhysRevA.94.053618.

[179] Alan O. Jamison, Benjamin Plotkin-Swing, and Subhadeep Gupta. "Advances in precision contrast interferometry with Yb Bose-Einstein condensates". In: *Phys. Rev. A* 90 (6 Dec. 2014), p. 063606. DOI: 10.1103/PhysRevA.90.063606. URL: https://link.aps.org/doi/10.1103/PhysRevA.90.063606.

[180] Holger Müller, Sheng-wey Chiow, and Steven Chu. "Atom-wave diffraction between the Raman-Nath and the Bragg regime: Effective Rabi frequency, losses, and phase shifts". In: *Phys. Rev. A* 77 (2 Feb. 2008), p. 023609. DOI: 10.1103/PhysRevA.77.023609. URL: https://link.aps.org/doi/10.1103/PhysRevA.77.023609.

[181] P. Cladé, T. Plisson, S. Guellati-Khélifa, F. Nez, and F. Biraben. "Theoretical analysis of a large momentum beamsplitter using Bloch oscillations". In: *The European Physical Journal D* 59.3 (2010), pp. 349–360.

[182] C. Yu. "Measuring the fine structure constant with a state-of-the-art atom interferometer". PhD thesis. University of California, Berkeley, 2018.

[183] P. L. Knight, B. Stoicheff, D. Walls, A. Peters, K. Y. Chung, B. Young, J. Hensley, and S. Chu. "Precision atom interferometry". In: *Philosophical Transactions of the Royal Society of London. Series A: Mathematical, Physical and Engineering Sciences* 355.1733 (1997), pp. 2223–2233. DOI: 10.1098/rsta.1997.0121. eprint: https://royalsocietypublishing.org/doi/pdf/10.1098/rsta.1997.0121. URL: https://royalsocietypublishing.org/doi/abs/10.1098/rsta.1997.0121.

[184] Tim Kovachy, Sheng-wey Chiow, and Mark A. Kasevich. "Adiabatic-rapid-passage multiphoton Bragg atom optics". In: *Phys. Rev. A* 86 (1 July 2012), p. 011606. DOI: 10.1103/PhysRevA.86.011606. URL: https://link.aps.org/doi/10.1103/PhysRevA.86.011606.

[185] E. Giese, A. Roura, G. Tackmann, E. M. Rasel, and W. P. Schleich. "Double Bragg diffraction: A tool for atom optics". In: *Phys. Rev. A* 88 (5 Nov. 2013), p. 053608. DOI: 10.1103/PhysRevA.88.053608. URL: https://link.aps.org/doi/10.1103/PhysRevA.88.053608.